



# **Spatio-Temporal Estimation and Validation of Remotely Sensed Vegetation and Hydrological Fluxes in the Rur Catchment, Germany**

Muhammad Ali

Energie & Umwelt / Energy & Environment

Band / Volume 403

ISBN 978-3-95806-287-0

# Spatio-Temporal Estimation and Validation of Remotely Sensed Vegetation and Hydrological Fluxes in the Rur Catchment, Germany

Dissertation  
zur  
Erlangung des Doktorgrades (Dr. rer. nat.)  
der  
Mathematisch-Naturwissenschaftlichen Fakultät  
der  
Rheinischen Friedrich-Wilhelms-Universität Bonn

vorgelegt von  
**Muhammad Ali**

aus  
Charsadda (KP)  
Pakistan

Bonn 2017



Angefertigt mit Genehmigung der Mathematisch-Naturwissenschaftlichen Fakultät der Rheinischen Friedrich-Wilhelms-Universität Bonn

1. Gutachter: Prof. Dr. Harry Vereecken
2. Gutachter: Prof. Dr. Bernd Diekkrüger

Tag der Promotion: December 04, 2017

Erscheinungsjahr: 2018



Forschungszentrum Jülich GmbH  
Institut für Bio- und Geowissenschaften  
Agrosphäre (IBG-3)

# **Spatio-Temporal Estimation and Validation of Remotely Sensed Vegetation and Hydrological Fluxes in the Rur Catchment, Germany**

Muhammad Ali

Schriften des Forschungszentrums Jülich  
Reihe Energie & Umwelt / Energy & Environment

Band / Volume 403

---

ISSN 1866-1793

ISBN 978-3-95806-287-0

Bibliografische Information der Deutschen Nationalbibliothek.  
Die Deutsche Nationalbibliothek verzeichnet diese Publikation in der  
Deutschen Nationalbibliografie; detaillierte Bibliografische Daten  
sind im Internet über <http://dnb.d-nb.de> abrufbar.

Herausgeber  
und Vertrieb:           Forschungszentrum Jülich GmbH  
                                  Zentralbibliothek, Verlag  
                                  52425 Jülich  
                                  Tel.: +49 2461 61-5368  
                                  Fax: +49 2461 61-6103  
                                  **zb-publikation@fz-juelich.de**  
                                  **www.fz-juelich.de/zb**

Umschlaggestaltung:   Grafische Medien, Forschungszentrum Jülich GmbH

Titelbild:                Satellitenaufnahme: DLR (RapidEye), © Planet Labs

Druck:                    Grafische Medien, Forschungszentrum Jülich GmbH

Copyright:              Forschungszentrum Jülich 2018

Schriften des Forschungszentrums Jülich  
Reihe Energie & Umwelt / Energy & Environment, Band / Volume 403

D 5N (Diss., Bonn, Univ., 2017)

ISSN 1866-1793  
ISBN 978-3-95806-287-0

Vollständig frei verfügbar über das Publikationsportal des Forschungszentrums Jülich (JuSER)  
unter [www.fz-juelich.de/zb/openaccess](http://www.fz-juelich.de/zb/openaccess).



This is an Open Access publication distributed under the terms of the [Creative Commons Attribution License 4.0](https://creativecommons.org/licenses/by/4.0/), which permits unrestricted use, distribution, and reproduction in any medium, provided the original work is properly cited.

## Abstract

Operational availability of spatio-temporal vegetation and hydrological estimates are becoming increasingly attractive for hydrologic studies from local through regional and global scales, especially in remote areas and ungauged basins. More advancement and versatility in satellite-based remotely sensed methods towards consistent and timely information for monitoring regional scale vegetation and hydrological fluxes may lead to efficient and unprecedented planning and management of agricultural practices and water resources. This thesis develops and analyses remote sensing methods for regional scale vegetation and land surface water fluxes estimation. Results from this study are validated at various test sites in the Rur catchment, Germany. These sites are equipped with sophisticated and state-of-the-art instruments for monitoring vegetation and hydrological fluxes.

Second chapter in this thesis explains a direct retrieval method and validation of the Leaf Area Index (LAI) from time-series of multispectral RapidEye images. LAI, quantifying the amount of leaf material, considered as an important variable for numerous processes in hydrological studies that link vegetation to climate. *In situ* LAI measuring methods have the limitation of being labor intensive and site specific. Remote sensing LAI ( $LAI_{\text{rapideye}}$ ) were derived using different vegetation indices, namely SAVI (Soil Adjusted Vegetation Index) and NDVI (Normalized Difference Vegetation Index). Additionally, applicability of the newly available red-edge band (RE) was also analyzed through Normalized Difference Red-Edge index (NDRE) and Soil Adjusted Red-Edge index (SARE). The  $LAI_{\text{rapideye}}$  obtained from vegetation indices with red-edge band showed better correlation with destructive  $LAI_{\text{destr}}$  ( $r = 0.88$  and Root Mean Square Deviation,  $RMSD = 1.01$  &  $0.92$ ) than LAI from vegetation indices without red-edge band. This study also investigated the need to apply relative and absolute atmospheric correction methods to the time-series of RapidEye Level 3A data prior to LAI estimation. Analysis of the RapidEye data set showed that application of the atmospheric corrections did not improve correlation of the estimated LAI with *in situ* LAI, because RapidEye Level 3A data are provided with simplified atmospheric corrections and the vegetation indices used for LAI retrieval were already normalized.

Third chapter investigates estimation of spatio-temporal latent heat using an energy balance approach and simplified regression between calculated latent heat (from energy balance) and downward shortwave radiation data from the Spinning Enhanced Visible and Infrared Imager (SEVIRI) onboard Meteosat Second Generation (MSG) Satellites. Mapping the spatio-temporal



variability of latent heat is crucial to better explain important area-wide hydrological compartments and on the long term variations of climate system components as it determines evapotranspiration. In addition to atmospheric demand, vegetation especially leaf area determine the amount of water loss to the atmosphere as evapotranspiration. Here, I evaluate the use of land surface temperature, albedo, LAI and net radiation estimated at a satellite platform on coarse spatial but high temporal resolution in a two source land-atmosphere energy exchange model for estimating latent heat. First, latent and sensible heat fluxes ( $LE_{EBM}$  and  $H_{EBM}$ ) were calculated using a two source energy balance model for points in time where input data from remote sensing were available. Secondly, a complete spatio-temporal dataset of latent heat ( $LE_{REG}$ ) was estimated through a linear regression fit of  $LE_{EBM}$  to satellite-based shortwave radiation, in order to quantify the gap-free consistent latent heat.  $LE_{EBM}$  showed a correlation coefficient ( $r$ ) of 0.83, 0.80, 0.84, 0.90, 0.85 and a root-mean-square difference RMSD of 63.41, 75.41, 66.16, 118.25 and  $150.00 \text{ Wm}^{-2}$  with *in situ* latent heat ( $LE_{EC}$ ) at five sites in the Rur catchment (Germany), namely, the lowland crop sites Selhausen and Merzenhausen, the low- and upland grassland sites Selhausen-Ruraue and Rollesbroich, and the forest site Wuestebach, respectively.  $LE_{REG}$  exhibits correlation coefficient ( $r$ ) of 0.83, 0.78, 0.86, 0.89, 0.83 and a RMSD of 51.15, 56.28, 47.46, 43.24 and  $61.29 \text{ Wm}^{-2}$  with  $LE_{EC}$  at Selhausen, Merzenhausen, Selhausen-Ruraue, Rollesbroich and Wuestebach, respectively. While  $LE_{REG}$  leads to a strong increase in the number of available hourly data points, correlation coefficients show only minor differences compared to  $LE_{EMB}$ . The present study reveals a high ET rate (i.e., 641, 645, 644, 626 and  $616 \text{ mmyear}^{-1}$ ) during 2011 and a comparatively low annual ET rate (i.e., 594, 593, 597, 580 and  $560 \text{ mmyear}^{-1}$ ) in 2012 with respect to all test sites. In general, the ET rate shows an increasing trend again towards 2015.

Operational and reliable estimates of rain, evapotranspiration and runoff with respect to space and time are crucial for water balance applications to monitor quantitative variability of water resources. On catchment scale, runoff is the balance between water received as precipitation and water lost as evapotranspiration. Therefore, fourth chapter explains balancing of solely remotely sensed evapotranspiration and rainfall to quantify annual runoff patterns. In this study, predicted runoff correlates very well ( $r = 0.95$ ) with *in situ* runoff, and mean annual runoff for the whole Rur catchment observed at the Stah gauge was 232.92 mm (predicted) and 279.66 mm (*in situ*) during 2012-2014. The approach of solely remotely-sensed water balance allows for the quantitative estimates of water balance and can be utilized for the water resources management at catchment scale.

In general, this thesis investigated the usability of remotely sensed data to derive time-series of LAI, evapotranspiration and annual runoff patterns. Dynamics of water and energy cycles are intimately linked at all scales at the land surface whereby density and type of vegetation play crucial role. Methods developed in this thesis, with minimum possible *in situ* inputs, will lead to better vegetation bio-physical and hydrological estimates on remotely sensed data especially in catchments with no or few ground-based networks.

## Zusammenfassung

Operationell verfügbare Daten raum-zeitlicher Muster von Vegetation und hydrologischen Größen wie Evapotranspiration und Grundwasserneubildung sind für hydrologische Analysen von großer Wichtigkeit. Dies gilt für alle Skalen, von der lokalen über die regionale zur globalen Ebene, insbesondere in unzugänglichen Regionen und Gebiete ohne (Pegel-) Messungen. Technische und methodische Entwicklungen in der satellitenbasierten Fernerkundung in Richtung konsistenter und zeitnaher Informationen über regionale Vegetation und Hydrologie führen zu nie dagewesenen Möglichkeiten im Agrar- und Wasserressourcenmanagement. Die vorliegende Dissertation entwickelt und analysiert Fernerkundungsmethoden zur regionalen Erfassung von Vegetationsmustern und Wasserflüssen an der Erdoberfläche. Die Ergebnisse werden in verschiedenen Teilen des Flusseinzugsgebietes der Rur in Deutschland validiert. Die Validationsstandorte sind mit hochmodernem Equipment ausgestattet, die es erlauben Vegetationsänderungen und Wasser- und Energieflüsse zu messen.

Im zweiten Kapitel dieser Dissertation wird eine Methode zur direkten Ableitung des Blattflächenindex (leaf area index, LAI) von Zeitreihen des multispektralen RapidEye-Satelliten entwickelt. LAI ist eine wichtige Variable für diverse hydrologische Prozesse. Regionale *in situ* Messungen des LAI sind limitiert durch Arbeitsaufkommen und lokale Charakteristika. Der regionale LAI wird anhand von verschiedenen Indizes aus Spektralkanälen errechnet, z.B. vom SAVI (Soil Adjusted Vegetation Index) und vom NDVI (Normalized Difference Vegetation Index). Zusätzlich zu diesen weit verbreiteten Indizes wird der „Red-Edge“-Kanal von RapidEye verwendet, um den Normalized Difference Red-Edge index (NDRE) und den in dieser Arbeit erstmals beschriebenen Soil Adjusted Red-Edge index (SARE) für die LAI-Berechnung heranzuziehen. Letztere „Red-Edge“-basierte Indizes zeigen signifikant bessere Korrelationen mit destruktiven Messungen der Pflanzen ( $r = 0.88$  und Root Mean Square Deviation, RMSD = 1.01 & 0.92) als Indizes die standardmäßig den nahinfraroten Kanal verwenden. Darüber hinaus wurde ermittelt, ob eine relative oder eine absolute atmosphärische Korrektur der RapidEye-Daten (Level 3A) vor Berechnung des LAI notwendig ist. Die Ergebnisse zeigen, dass beide zusätzlichen Korrekturmöglichkeiten keinen positiven Einfluss auf die Korrelationen zu den Bodenmessungen des LAI haben, da bereits eine rudimentäre Atmosphärenkorrektur der RapidEye Level 3A Daten vorliegt und die Vegetationsindizes normalisierenden Charakter besitzen.

Das dritten Kapitel untersucht die raum-zeitliche Abschätzung des latenten Wärmeflusses mit Hilfe eines Energiebilanzansatzes und einer vereinfachten Regression anhand von Daten des Spinning Enhanced Visible and infrared Imager (SEVIRI) Sensors an Bord des Meteorosat Second Generation (MSG) Satelliten. Eine Kartierung der raum-zeitlichen Variabilität des latenten Wärmeflusses ist in der Lage, Kompartimente des hydrologischen Kreislaufs flächendeckend zu erfassen und langfristige Trends im Rahmen des überlagernden Klimasystems zu erklären. Die Nutzung der Landoberflächentemperatur und Nettostrahlung erfasst von einer geostationären Satellitenplattform in einem Land-Atmosphäre Energiebilanzmodell wird evaluiert für die Berechnung des latenten Wärmeflusses, bzw. der Evapotranspiration. Zunächst werden der latente und sensible Wärmefluss mit einem Zweiquellen-Energiebilanzmodell berechnet, an denen Fernerkundungsdaten verfügbar sind. In einem zweiten Schritt werden die durch Wolkenbedeckung entstandenen Lücken im Datensatz zum latenten Wärmefluss gefüllt, indem ein linearer Zusammenhang zu Satellitenbeobachtungen der kurzwelligen Strahlung gefunden wird. Dadurch entsteht ein lückenloser Datensatz des latenten Wärmeflusses, der Korrelationen ( $r$ ) von 0.83, 0.80, 0.84, 0.90, 0.85 und RMSD von 63.41, 75.41, 66.16, 118.25 und 150.00  $\text{Wm}^{-2}$  mit Eddy Covarianz-Stationen an fünf Standorten im Rureinzugsgebiet (Selhausen, Merzenhausen, Selhausen-Ruraue, Rollesbroich and Wuestebach) aufweist. Zum Vergleich liefert das Lücken aufweisende Energiebilanzmodell Korrelationen ( $r$ ) von 0.83, 0.78, 0.86, 0.89, 0.83 und RMSD von 51.15, 56.28, 47.46, 43.24 und 61.29  $\text{Wm}^{-2}$  für die genannten Standorte. Trotz der höheren Datendichte des lückenlosen Datensatzes ist keine Verschlechterung der Korrelation zu beobachten. Auf dieser Basis können nun Jahressummen der Evapotranspiration berechnet werden, die 2011 recht hoch ausfiel, während 2012 eher durch niedrige Jahressummen gekennzeichnet war. In der kurzen untersuchten Zeitspanne gibt es einen leicht zunehmenden Trend in Richtung des Jahres 2015.

Operationell verfügbare und verlässliche Niederschlags-, Verdunstungs- und Abflussmengen in hoher räumlich und zeitlicher Auflösung sind Voraussetzung für Anwendungen im Wasserressourcenmanagement. Deshalb erstellt das vierte Kapitel eine Wasserhaushaltsbilanz aus rein fernerkundlichen Messungen. Niederschlag und im Kapitel zuvor berechnete Verdunstungsmengen werden bilanziert, und das Ergebnis mit jährlichen Abflussmengen verglichen. Der aus Fernerkundungsdaten bilanzierte jährliche Abfluss auf Subeinzugsgebietsebene korreliert sehr gut ( $r = 0.95$ ) mit Abflussmessungen im Gewässer. Langjährige Mittel (2012-2014) des Abflusses am Pegel Stah (des deutschen und belgischen

Teils des Rureizugsgebietes) liegen bei 232.92 mm (Fernerkundung) bzw. 279.66 mm (*in situ*). Rein fernerkundliche Wasserbilanzen sind in der Lage, auf Einzugsgebietsebene quantitative Informationen für ein Wasserressourcenmanagement zu liefern.

Diese Dissertation untersucht somit die Nutzbarkeit von fernerkundungsbasierten Methoden zur räumlich und zeitlich hochaufgelösten Abschätzung des Blattflächenindex, Verdunstungshöhen und jährlichen Abflussmengen. An der Erdoberfläche sind die Wasser- und Energieflüsse eng miteinander verbunden, wobei die Vegetation eine zentrale Rolle in dieser Dynamik einnimmt. Deshalb werden die in dieser Dissertation entwickelten Methoden der Erdbeobachtung ein verbessertes biophysikalisches und hydrologisches Monitoring begünstigen. Dies trifft vor allem für unzugängliche Regionen ohne systematische lokale Messnetze zu.

## Acknowledgements

This work was supported by the Higher Education Commission of Pakistan with partial support from the German Academic Exchange Service (DAAD). The study was incorporated in the Transregional Collaborative Research Centre 32 (TR32): “Patterns in Soil-Vegetation-Atmosphere Systems: Monitoring, modelling and data assimilation” from the German Research Foundation (DFG). RapidEye data have been provided by the RapidEye/Black Bridge (now Planet Labs) under the collaboration with the Terrestrial Environmental Observatories (TERENO). Remotely sensed LAI, albedo, DSSF, DSLF and LST were downloaded from the EUMETSAT’s Land Surface Analysis Satellite Applications Facility (LSA SAF). The Eddy Covariance and runoff gauge data was provided by the TERENO. The *in situ* air temperature and rainfall and ground radar-based rainfall data (RADOLAN) was provided by the German Weather Service (DWD).

First, I would like to express my gratitude for my supervisor Prof. Dr. Harry Vereecken, head of IBG-3, for the discussions on my work, his input on this thesis and all the possibilities I had at the Agrosphere.

I am grateful to my “everyday” supervisor Dr. Carsten Montzka and colleagues, Alex Graf and Francois Jonard, for all their guidance, support and gracious efforts. Their scientific discussions and constructive comments made me possible to accomplish this task and more importantly building my attitude of systematic scientific investigations and scientific writings.

Furthermore, I would like to thank Prof. Dr. Bernd Diekkrüger (Istitute of Geography, University of Bonn) for taking over the co-supervision. I am also thankful to Frank Thonfeld of the Centre for Remote Sensing of Land Surfaces (ZFL), University of Bonn, for his guidance on atmospheric corrections and statistical analysis.

I am thankful to all my colleagues at the Agrosphere IBG-3 at Research Center Juelich, especially Heye Bogena, Cho Miltin Mboh, Thomas Schustler and Horst Hardelauf. Profound appreciation goes to my dear friends Khanzaib Jadoon and Ayaz Khan (IEK-8) for all their guidance and help throughout my PhD.

Last, I love to mention the role of my family, my mother, brothers and sisters for all their prayers, support and encouragement. I am thankful to my wife, Beena, for providing me

peaceful and joyful environment at home and encouraged me at every stage of my thesis. Thank you Irtaza and Izaan (my sons), your single smile was a source of enough energy for me.

Muhammad Ali

Bonn, December 2017

## Table of Contents

|  |     |
|--|-----|
| Abstract .....   | i   |
| Zusammenfassung .....  | iv  |
| Acknowledgements .....   | vii |
| List of Tables.....  | xi  |
| List of Figures .....  | xii |
| Acronyms & Symbols .....   | xiv |
| 1. General Introduction.....   | 1   |
| 1.1. Background and Motivation .....   | 1   |
| 1.2. Vegetation and Hydrological Variables .....   | 2   |
| 1.2.1. Leaf Area Index (LAI).....  | 2   |
| 1.2.2. Evapotranspiration (ET) .....   | 4   |
| 1.2.3. Water Balance (Runoff Prediction) .....   | 7   |
| 1.3. Remote Sensing of Land Surface Hydrology .....  | 9   |
| 1.4. Scientific Objectives and structure of the thesis.....  | 10  |
| 2. Estimation and Validation of RapidEye-Based Time-Series of Leaf Area Index for Winter Wheat in the Rur Catchment (Germany) .....  | 12  |
| 2.1. Introduction .....  | 12  |
| 2.2. Study Area.....   | 15  |
| 2.3. RapidEye and <i>In Situ</i> Measurements.....   | 17  |
| 2.3.1. RapidEye Data.....  | 17  |
| 2.3.2. <i>In Situ</i> LAI Measurements (LAI <sub>destr</sub> ) .....   | 18  |
| 2.4. Approach / Methods .....  | 20  |
| 2.4.1. The Need for Radiometric/Atmospheric Correction .....   | 21  |
| 2.4.2. Estimation of LAI Time-series from RapidEye .....   | 22  |
| 2.4.3. Impact of the Soil Contribution on LAI Calculation .....  | 23  |
| 2.4.4. Role of the Red-edge Band.....  | 24  |
| 2.5. Results and Discussion .....  | 24  |
| 2.5.1. Impact of the Absolute and Relative Atmospheric/Radiometric Correction .....  | 24  |
| 2.5.2. Estimation of LAI Time-series from RapidEye .....   | 30  |
| 2.6. Conclusions and Outlook .....   | 35  |
| 3. A Simplified Approach to Derive Continuous Hourly Time-series of Latent Heat Flux by Remote Sensing Using a Two Source Energy Balance Model: A Case Study in the Rur Catchment, Germany | 38  |
| 3.1. Introduction .....  | 38  |
| 3.2. Study Area.....   | 43  |



|          |  |     |
|----------|--|-----|
| 3.3.     | Data and Methods.....  | 44  |
| 3.3.1.   | <i>In Situ</i> Flux Measurements.....  | 44  |
| 3.3.2.   | Satellite-based Fluxes and Evapotranspiration Calculation .....                    | 45  |
| 3.3.2.1. | Approach 1 .....   | 49  |
| 3.3.2.2. | Approach 2 .....   | 50  |
| 3.4.     | Results and discussion.....  | 51  |
| 3.4.1.   | Validation of $LE_{EMB}$ and $H_{EMB}$ (Approach 1).....                           | 51  |
| 3.4.2.   | Validation of $LE_{REG}$ (Approach 2).....   | 57  |
| 3.5.     | Conclusions .....  | 68  |
| 4.       | Towards a Solely Remotely-Sensed Water Balance for the Rur Catchment, Germany..... | 70  |
| 4.1.     | Introduction .....   | 70  |
| 4.2.     | Materials and Methods .....  | 73  |
| 4.2.1.   | Hydro-geological Description of the Study Area.....                                | 73  |
| 4.2.2.   | Remotely Sensed Precipitation Estimates .....                                      | 74  |
| 4.2.3.   | Remotely-sensed ET estimates.....  | 76  |
| 4.2.4.   | Water Balance .....  | 76  |
| 4.3.     | Results and Discussions .....  | 77  |
| 4.3.1.   | Annual Runoff.....   | 77  |
| 4.3.2.   | Mean Annual Runoff.....  | 81  |
| 4.4.     | Conclusion and Outlook.....  | 85  |
| 5.       | Synthesis.....   | 87  |
| 5.1.     | Final conclusion .....   | 87  |
| 5.1.1.   | Estimation and validation of LAI.....  | 87  |
| 5.1.2.   | Evapotranspiration.....  | 88  |
| 5.1.3.   | Water Balance .....  | 89  |
| 5.2.     | Outlook.....   | 90  |
|          | Bibliography.....  | 92  |
|          | Curriculum Vitae.....  | 113 |

## List of Tables

|  |    |
|--|----|
| Table 2.1. <i>In situ</i> LAI and RapidEye time-series available for this study at both test fields ...  | 19 |
| Table 2.2. Direct comparison of different spectral vegetation indices calculated on RapidEye L3A, IR-MAD and ATCOR processed RapidEye data with LAI <sub>destr</sub> for winter wheat at two different locations. Top numbers in each cell represent the r for the Selhausen field (2011-2012), the bottom numbers in each cell represent the Merzenhausen field (2011), in brackets the significance level ( <i>p</i> -value) is given..... | 26 |
| Table 2.3. Comparison of the LAI <sub>NDVI</sub> (RapidEye standard L3A, IR-MAD and ATCOR processed) with LAI <sub>destr</sub> , in winter wheat fields at Selhausen and Merzenhausen test sites. (Numbers in bold represent the best correlation in a column while underlined number represent the insignificant correlation) .....   | 27 |
| Table 2.4. Validation result through splitting the sample set into calibration and validation sets for LAI estimates from RapidEye .....   | 31 |
| Table 3.1. Correlation statistics of hourly <i>in situ</i> and remotely sensed net radiation (R <sub>n</sub> ) for Eddy Covariance sites in the Rur catchment, Germany, for five years (2011-2015).....  | 52 |
| Table 3.2. Correlation statistics on hourly <i>in situ</i> latent and sensible heat fluxes (LE <sub>EC</sub> and H <sub>EC</sub> ) and remotely sensed latent and sensible heat (LE <sub>EBM</sub> and H <sub>EBM</sub> ) for the Eddy Covariance sites in the Rur catchment, Germany, for five years (2011-2015). .....   | 53 |
| Table 3.3. Correlation statistics of hourly <i>in situ</i> and remotely sensed Downwelling Shortwave Surface Flux (DSSF) for Eddy Covariance sites in the Rur catchment, Germany, for five years (2011-2015).....  | 57 |
| Table 3.4. Correlation statistics on hourly <i>in situ</i> latent heat flux (LE <sub>EC</sub> ) and remotely sensed latent heat (LE <sub>REG</sub> ) for the Eddy Covariance sites in the Rur catchment, Germany, for five years (2011-2015).....  | 61 |
| Table 3.5. Annual evapotranspiration (mmyear <sup>-1</sup> ) for Eddy Covariance sites in the Rur catchment, Germany, for the years 2011-2015. ....  | 67 |
| Table 4.1a. Annual rate of radar-based rainfall, satellite-based ET, predicted and <i>in situ</i> runoff for various sub-catchments in the Rur catchment, Germany, during 2011-2012. ....  | 78 |
| Table 4.1b. Annual rate of radar-based rainfall, satellite-based ET, predicted and <i>in situ</i> runoff for various sub-catchments in the Rur catchment, Germany, during 2013-2014. ....  | 79 |
| Table 4.2. Mean annual rate of radar-based rainfall, satellite-based ET, predicted and <i>in situ</i> runoff for various sub-catchments in the Rur catchment, Germany, during 2012 through 2014. ....  | 82 |

## List of Figures

|  |    |
|--|----|
| Figure 2.1. The Rur Catchment (Germany), as seen by RapidEye on June 27, 2011. Individual test sites at Selhausen and Merzenhausen are shown with sampling points. ....  | 17 |
| Figure 2.2. Spectral Reflectance Curves for various features of the land surface plotted against different RapidEye’s spectral channels. Vertical bars represent spectral bands of the RapidEye imagery. (Source for the reflectance data is ASTER Spectral Library). .... | 18 |
| Figure 2.3. Flowchart description of the study. ....   | 20 |
| Figure 2.4. Part of the standard L3A RapidEye image from April 02, 2011 (A). The reference image dated April 24, 2011 (B). IR-MAD processed image (C). RGB band combinations are 3-2-1. ....   | 25 |
| Figure 2.5. Temporal sequence of field-average destructive $LAI_{destr}$ with remote sensing based $LAI_{NDVI}$ (RapidEye L3A imagery, IR-MAD and ATCOR processed) at Selhausen winter wheat field for 2011-2012. ....   | 28 |
| Figure 2.6. Scatter Plot of the $LAI_{NDVI}$ (RapidEye standard L3A, IR-MAD and ATCOR processed) with $LAI_{destr}$ for winter wheat field at Selhausen for 2011 and 2012 (blue) and at Merzenhausen for 2011 (red). ....  | 28 |
| Figure 2.7. Comparison of the light extinction coefficient and RMSD for NDVI, NDRE, SAVI and SARE based LAI for the Selhausen and the Merzenhausen winter wheat fields. ....   | 31 |
| Figure 2.8. Temporal sequence of field-average destructive $LAI_{destr}$ with remote sensing based $LAI_{NDVI}$ and $LAI_{SAVI}$ (upper) and $LAI_{NDRE}$ and $LAI_{SARE}$ (lower). ....   | 33 |
| Figure 2.9. Winter wheat $LAI_{NDRE}$ map of the northern Rur Catchment for April, 2, 2011. ....   | 35 |
| Figure 3.1. Rur Catchment, Germany, with Eddy Covariance sites. ....   | 44 |
| Figure 3.2. Flowchart description of the study for estimating evapotranspiration. ....   | 46 |
| Figure 3.3. Scatter plots of hourly <i>in situ</i> and remotely sensed net radiation ( $R_n$ ) for Eddy Covariance sites in the Rur catchment, Germany, for five years (2011-2015). ....   | 52 |
| Figure 3.4. Scatter plots of hourly $LE_{EC}$ ( <i>in situ</i> ) and $LE_{EBM}$ (energy balance model) for the Eddy Covariance sites in the Rur catchment, Germany, for the years 2011-2015. ....  | 54 |
| Figure 3.5. Scatter plots of hourly $H_{EC}$ ( <i>in situ</i> ) and $H_{EBM}$ (energy balance model) for the Eddy Covariance sites in the Rur catchment, Germany, for the years 2011-2015. ....  | 54 |
| Figure 3.6. Scatter plots of hourly <i>in situ</i> and remotely sensed Downwelling Shortwave Surface Flux (DSSF) for Eddy Covariance sites in the Rur catchment, Germany, for five years (2011-2015). ....   | 58 |
| Figure 3.7. Regression slope of $LE_{EBM}$ and DSSF (pixel-wise) for the whole study period from 2011 through 2015 for the Rur catchment. ....   | 60 |

Figure 3.8. Scatter plots of hourly  $LE_{EC}$  (*in situ*) and  $LE_{REG}$  (through regression analysis from downwelling surface shortwave flux) for Eddy Covariance sites in the Rur catchment, Germany, for the years 2011-2015. .... 61

Figure 3.9. Scatter plot of hourly  $LE_{REG}$  and  $LE_{EC}$  for June and mid-August to mid-September during 2012 at Merzenhausen. .... 64

Figure 3.10. Temporal sequence of  $LE_{REG}$  and  $LE_{EC}$  during June 2012 (upper) and mid-August to mid-September 2012 (lower) at Merzenhausen. .... 65

Figure 3.11. Annual evapotranspiration ( $mm\text{year}^{-1}$ ) in the Rur catchment (2011-2015). .... 66

Figure 3.12. Annual sum of evapotranspiration ( $mm\text{year}^{-1}$ ) for Eddy Covariance sites, namely, Selhausen (SE), Merzenhausen (ME), Selhausen-Ruraue (RU), Rollesbroich (RO) and Wuestebach (WU) for a period of 2011 through 2015, in the Rur catchment, Germany. .... 67

Figure 4.1. Sub-catchments in the Rur catchment with Rur River and its main tributaries along with runoff measuring gauge locations. .... 73

Figure 4.2. Comparison of the annual remotely sensed radar-based rain rate (RADOLAN), satellite-based ET, predicted and *in situ* runoff for various sub-catchments in the Rur catchment for the year 2011 through 2014. .... 79

Figure 4.3. Hydrograph of annual *in situ* and estimated runoff for various sub-catchments in the Rur catchment for the years 2011-2014. .... 81

Figure 4.4. Mean annual remotely sensed radar-based rain rate (RADOLAN), satellite-based ET, predicted and *in situ* runoff for various sub-catchments in the Rur catchment for the year 2012 through 2014. .... 83

Figure 4.5. Scatter plot of mean annual *in situ* and predicted runoff for various sub-catchments in the Rur catchment for the years 2012-2014. .... 84

## Acronyms & Symbols

|                      |  |
|----------------------|--|
| $\alpha$             | Albedo   |
| ATCOR                | Atmospheric Correction   |
| $C_p$                | Specific heat of the air ( $993 \text{ Jkg}^{-1}\text{k}^{-1}$ ) |
| $\Delta$             | slope of the saturation vapour pressure temperature relationship |
| dBZ                  | Decibel of Radar Reflectivity Factor (z)                         |
| DSLFL                | Down-welling Surface Longwave Flux                               |
| DSSF                 | Down-welling Surface Shortwave Flux                              |
| DWD                  | Deutsche Wetter Dienst (German Weather Service)                  |
| $\varepsilon$        | Surface Emissivity   |
| EBM                  | Energy Balance Model   |
| ET                   | Evapotranspiration   |
| EUMETSAT             | European Meteorological Satellites                               |
| FVC, $f_c$           | Fractional Vegetation Cover                                      |
| G                    | Ground Heat Flux   |
| GPM                  | Global Precipitation Mission                                     |
| H                    | Sensible Heat Flux   |
| $H_c$                | Sensible Heat (Canopy Component)                                 |
| $H_s$                | Sensible Heat (Soil Component)                                   |
| I                    | Infiltration   |
| IR-MAD               | Iteratively Reweighted Multivariate Alteration Detection         |
| $k(\theta)$          | Light Extinction Coefficient                                     |
| L                    | Soil Brightness Correction Factor                                |
| LAI                  | Leaf Area Index  |
| $LAI_{\text{destr}}$ | LAI measured with Destructive method                             |
| LE                   | Latent Heat Flux   |
| $LE_c$               | Latent Heat (Canopy Component)                                   |
| $LE_{\text{EBM}}$    | LE derived using Energy Balance Model                            |
| $LE_{\text{REG}}$    | LE derived using regression                                      |
| $LE_s$               | Latent Heat (Soil Component)                                     |
| LST                  | Land Surface Temperature   |
| MFG                  | Meteosat First Generation  |
| MPE                  | Multiple-sensor Precipitation Estimates                          |
| MSG                  | Meteosat Second Generation                                       |

|                   |  |
|-------------------|--|
| NDVI              | Normalized Difference Vegetation Index   |
| NDVI <sub>s</sub> | NDVI of bare soil  |
| NDVI <sub>v</sub> | NDVI of fully vegetated surface  |
| NDRE              | Normalized Difference Red-Edge Index   |
| NIR               | Near-Infrared  |
| p                 | Statistical Significance   |
| P                 | Precipitation  |
| $\rho$            | Air Density ( $1.225 \text{ kgm}^{-3}$ )   |
| Q <sub>T</sub>    | Total Runoff   |
| Q <sub>S</sub>    | Surface Runoff   |
| r                 | Correlation Coefficient  |
| R <sub>A</sub>    | Aerodynamic resistance   |
| RADAR             | RADio Detection And Ranging  |
| RADOLAN           | Radar-Online-Aneichung (Radar Online Adjustment)                                       |
| R <sub>n</sub>    | Net Radiation  |
| R <sub>n,c</sub>  | Net Radiation (Canopy Component)   |
| R <sub>n,s</sub>  | Net Radiation (Soil Component)   |
| RMSD              | Root Mean Square Difference  |
| R <sub>S</sub>    | Resistance to heat flow from soil  |
| R <sub>X</sub>    | Resistance to heat flow from canopy  |
| $\sigma$          | Stefan Boltzmann constant ( $\sigma = 5.6703 \times 10^{-8} \text{ W/m}^2\text{K}^4$ ) |
| SAVI              | Soil Adjusted Vegetation Index   |
| SARE              | Soil Adjusted Red-Edge Index   |
| SEVIRI            | Spinning Enhanced Visible and Infrared Imager  |
| $\Delta S$        | Changes in Terrestrial Water   |
| T <sub>A</sub>    | Air Temperature  |
| T <sub>AC</sub>   | Temperature within the canopy  |
| T <sub>C</sub>    | Canopy Temperature   |
| TRMM              | Tropical Rainfall Measuring Mission  |
| T <sub>S</sub>    | Soil Temperature   |
| TSM               | Tow Source Model   |
| u                 | Wind Speed   |
| USLF              | Up-welling Surface Longwave Flux   |
| USSF              | Up-welling Surface Shortwave Flux  |

|                  |  |
|------------------|--|
| $\text{Wm}^{-2}$ | Watts per square meter                       |
| $\gamma$         | Gamma (Psychrometric Constant = 0.066 kPa/K) |
| $z$              | Radar Reflectivity Factor                    |

## 1. General Introduction

### 1.1. Background and Motivation

Land surface processes are not static and constantly changing at different spatial and temporal scales, whereby vegetation, water and energy cycles play a dominant role and have obvious effects on shaping many terrestrial ecosystems (Pan *et al.*, 2008; Trenberth *et al.*, 2009; Syed *et al.*, 2010). Dynamics of water and energy cycles, mediated by the density and type of vegetation, are intimately linked at diverse spatial scales at the land surface (Schmugge *et al.*, 2002). Presence of vegetation greatly modifies and controls the distribution and variability of the energy (Yang *et al.*, 1994) and hydrological fluxes (Rind, 1984). Vegetation, ranging from evergreen forests and crops to grass meadows, has the potential to alter water and energy balances through albedo, level of carbon dioxide (CO<sub>2</sub>) in the atmosphere, evapotranspiration, interception, infiltration and surface runoff (Rind, 1984; Arora, 2002). Timely and adequate estimates regarding the type, density and phenological information of vegetation are key variables for crop yield and stress evaluation and to understand factors responsible for environmental changes (Curran, 1983). More than half of the total solar energy received on the land surface is consumed as latent heat in the process of evapotranspiration (Trenberth *et al.*, 2009; Jung *et al.*, 2010), however, this ratio is subjected to seasonal variations and dependent on the geographical location. Also, it can be linked to changing climate and land use patterns on the earth surface (Thompson *et al.*, 2011). Globally, more than 60% of the rain received at the earth surface goes back to the atmosphere through the process of evapotranspiration (Oki and Kanae, 2006). Being a major component of the hydrological cycle, dynamics of evapotranspiration are crucial for the water balance at all scales ranging from local to continental and global. Water resources availability is directly affected by changes in climatic conditions. Balance between water inflow (mainly precipitation) and outflow (including evapotranspiration and runoff) on catchment-scale provide reliable information for agricultural and water resources management, combating water shortages (droughts) and floods and plan accordingly for LULC (land use land cover) changes.

Precipitation, evapotranspiration, surface runoff and infiltration are major and important components of the hydrological cycle and there are many factors (both natural and human-induced) that affect and modify these components. These components and the state-variables that modify and affect these components, e.g., vegetation, need techniques for temporal and spatial monitoring operationally in order to better analyze the effects of hydrologic variability with respect to space and time. While being more precise and accurate, the *in situ* observation



systems are often point- or footprint-based and hence, cannot represent/capture the spatially distributed nature of the hydrological processes (Wang *et al.*, 2007; Yu and Ma, 2015). Remote sensing methods offer consistent and cost-effective data with a large range of spatial and temporal resolutions to better map the spatial and temporal explicit trends and patterns of various processes that affect the land surface hydrology. Precipitation, density/type of vegetation and the amount of evapotranspiration are the most important components that affect land surface hydrology from catchment to regional scales. Mapping the spatio-temporal dynamics of these components through remotely sensed methods would better describe catchment-scale hydrology, particularly, in ungauged or poorly gauged hydrological basins (Sivapalan *et al.*, 2003; McGlynn *et al.*, 2012).

Operational and consistent monitoring of the spatial distribution and temporal variations in hydrological processes and its various components lead to better policy decisions, reforms, precautionary measures and preparedness to control or mitigate (and even avoid) the devastating effects of extreme hydrological events. Hydrological extremes in the form of floods, droughts (Kundzewicz and Kaczmarek, 2000), tornados and hurricanes adversely affect the landscape and cause shortage of food and clean drinking water, loss of life and damage to physical infrastructure. Droughts, cause shortage of water in the hydrological system (Van Loon, 2015), are considered a very strong factor endangering food security (Sheffield *et al.*, 2014) and lead to food price spikes. Droughts are also known as ‘the creeping disaster’ that often happen very slow (unnoticed) and bring large scale indirect devastating results (Kundzewicz and Kaczmarek, 2000; Van Loon, 2015).

## **1.2. Vegetation and Hydrological Variables**

### **1.2.1. Leaf Area Index (LAI)**

The current global scenario of climate change may be linked to hydrological interactions in the soil-plant-atmosphere continuum (Arora, 2002; Gerten *et al.*, 2004; Smith *et al.*, 2011) and the spatio-temporal distribution of vegetation (Gu *et al.*, 2011). Type, distribution and density of vegetation affect the energy and water exchange between the earth’s surface and atmosphere. Energy balance approaches, aiming to retrieve hydrological fluxes, use vegetation as an important parameter due to its impact on the distribution of incoming radiation into latent, sensible and soil heat fluxes. As the plant species composition of an area can be very complex, simplified vegetation indices, for instance, the Leaf Area Index (LAI) which can be derived from optical remote sensing imagery is an important variable for climatic and hydrological

models (Sellers *et al.*, 1997). LAI is the ratio of total one-sided green leaf area per unit ground area ( $\text{m}^2/\text{m}^2$ ). A variety of methods, ranging from ground-based (*in situ*) to satellite-based remote sensing methods, are employed to quantify LAI. *In situ* methods are classified in destructive and non-destructive methods using LAI meters/sensors, e.g., LI-COR and Delta-T Devices (Wilhelm *et al.*, 2000; Stadler *et al.*, 2015). Destructive methods involve physical removal of plants, whereas, LAI meters use radiative transfer models to compute LAI from intercepted light (mostly blue light) by the canopy through measurements taken above and below the canopy. Being site specific, *in situ* LAI measurements can be replaced with remote sensing method. Remotely sensed methods provide regional scale LAI and are grouped into physical (Verhoef, 1984; Wilhelm *et al.*, 2000; Haboudane *et al.*, 2004; Jacquemoud *et al.*, 2009) and empirical models (Clevers, 1989; Colombo *et al.*, 2003; Walthall *et al.*, 2004). Physical methods make use of specialized models to simulate canopy reflectance for deriving various canopy bio-physical variables. However, physical models, simulating canopy reflectance, require significant computational resources. LAI is widely derived from remotely sensed vegetation indices by establishing simple empirical relations (for instance, Eq. 1.1) between the respective vegetation index (VI) and LAI (Norman *et al.*, 1995; Sprintsin *et al.*, 2007; Propastin and Erasmi, 2010):

$$LAI = \frac{-\log(1 - VI)}{k(\theta)} \quad (1.1)$$

Here,  $k(\theta)$  is the light extinction coefficient. The Normalized Difference Vegetation Index (NDVI), its modified form of soil adjusted vegetation index (SAVI), Enhanced Vegetation Index (EVI), Difference Vegetation Index (DVI), and Ratio Vegetation Index (RVI) are generally used as vegetation indices. These indices are mathematical combinations of those spectral bands that distinguish green plants than other objects. Information from red (0.630 – 0.685  $\mu\text{m}$ ) and near-infrared bands (0.760 – 0.850  $\mu\text{m}$ ) of the electromagnetic spectrum are widely used in these indices. Vegetation indices incorporating red-edge spectral band (0.690 – 0.730  $\mu\text{m}$ ) in multispectral RapidEye imagery will improve retrieval of vegetation related information owing to its high sensitivity towards chlorophyll content of leaves. Furthermore, LAI over agricultural vegetation is heavily changing over the year. High spatio-temporal resolutions of RapidEye data are suitable for more reliable estimates of temporal course of

vegetation dynamics, especially over agricultural regions. However, data availability is highly affected by overcast weather conditions. High spatio-temporal estimates of LAI would lead to better estimates of variability in evapotranspiration for heterogeneous surfaces in order to quantify more accurate annual sums.

Here, various satellite missions, carrying sensors for estimating vegetation related variables, are briefly discussed. All of the Landsat missions i.e., Landsat1-5 and Landsat6-7 provided data in visible (VIS) and near infrared (NIR) spectral channels for studying land surface. Satellite Probatoire d'Observation de la Terre (SPOT), with missions from SOPT1 through SPOT7, is a satellite-based high resolution optical Earth imaging system and delivers high resolution panchromatic and multispectral imagery in VIS, NIR and shortwave infrared (SWIR) channels since 1986. RapidEye of the Planet Labs (PlanetLabs), formerly belonged to BlackBridge, comprised of five identical satellites orbiting the earth provide data in five spectral bands i.e., blue (0.440 – 0.510  $\mu\text{m}$ ), green (0.520 – 0.590  $\mu\text{m}$ ), red (0.630 – 0.685  $\mu\text{m}$ ), red-edge (0.690 – 0.730  $\mu\text{m}$ ) and near infrared (0.760 – 0.850  $\mu\text{m}$ ). Operating at an altitude of 630 km, RapidEye is capable of providing daily multispectral imagery in 5m spatial resolution. The new red-edge spectral band makes it more appropriate for retrieving and monitoring biophysical vegetation parameters (Delegido *et al.*, 2011; Schumacher *et al.*, 2016). ESA's Sentinel-2 satellites with Multispectral Imager (MSI) onboard provide high resolution spectral images of the Earth's surface every 10 days with one satellite and every 5 days with 2 satellites. Sentinel-2 bands in the red-edge region are highly sensitive to green LAI and chlorophyll content (Ch) (Delegido *et al.*, 2011).

### **1.2.2. Evapotranspiration (ET)**

Evapotranspiration (ET) is the second largest component of the terrestrial water balance after rainfall and plays an imperative role in shaping water balance and weather system of an area. According to Thompson *et al.* (2011), ET dynamics can be linked to changing climate and land uses. The rate of ET is driven by many factors including meteorological variables, whereas vegetation (leaf area) and soil characteristics affect this rate. More precise and timely quantification of ET leads to better description of hydrological and meteorological processes. Being the largest component of the terrestrial energy budget, ET transfers most of the water (around 60%) back to the atmosphere received on the Earth as precipitation (Oki and Kanae, 2006; Trenberth *et al.*, 2009; Jung *et al.*, 2010; McMahon *et al.*, 2013). According to Jung *et al.* (2010), ET is considered as the central process of the climate system.

Different approaches are adopted to estimate evapotranspiration from a single point to global scale. *In situ* methods are more precise and accurate but cannot be applied on spatial scale owing to the spatial heterogeneity of land surfaces (Wang *et al.*, 2007), nevertheless, *in situ* measurements are extensively used to calibrate and validate spatial ET products. Some well-known *in situ* methods include pan evaporation, atmometers, lysimeters, scintillometers, eddy covariance (EC) and Bowen ratio (BR). On a regional scale, three main approaches are generally employed for mapping spatial scale evapotranspiration, i) Hydrological models, ii) Application of a water balance approach to ground-based catchment-scale measurements, and iii) Application of an energy balance approach to remote sensing data. Hydrological models are simplified representations of the real world water cycle and balance to predict and understand land surface hydrological processes (Wheater *et al.*, 2008; Devi *et al.*, 2015). A number of models have been developed to simulate hydrological processes for diverse spatial scales ranging from small catchments to global scales (Devi *et al.*, 2015), for instance, SWAT model (Soil Water Assessment Tool), MIKE SHE model (Systeme Hydrologique European), TOPMODEL, HBV model (Hydrologiska Byrans Vattenavdelning model), and VIC model (Variable Infiltration Capacity). Model calibration with hydrological properties measured with traditional *in situ* methods is an integral part for the hydrological models (Pechlivanidis *et al.*, 2011). Approaches suitable with no or less *in situ* calibrations are preferred, for instance, the energy balance approaches on remotely sensed data. The water balance approach calculates time changes in terrestrial water storage ( $\Delta S$ ) through balancing ground-based water inflow (rainfall) and outflow (evaporation, transpiration, runoff and infiltration) of a hydrological domain (see section 1.2.3). The energy balance approach is based on the distribution of incoming net radiation ( $R_n$ ) received on the earth surface (Eq. 1.2) and the availability of the amount of latent heat (LE) to cause evapotranspiration (transpiration from vegetation and evaporation from non-vegetated surfaces):

$$R_n = LE + H + G \quad (1.2)$$

Here, H and G are sensible and ground heat fluxes, respectively. Along with spatial variations, temporal changes in ET may occur on short time scales (less than an hour) due to its dependency primarily on the amount and duration of incoming solar radiations and some other

meteorological parameters. Generally, the energy balance methods are advantageous over other methods for computing evapotranspiration as these are independent of further water balance components, for instance, rainfall, runoff and moisture holding capacity of the soil (soil hydraulic properties) to estimate ET (Anderson *et al.*, 2011). Several approaches based on the energy balance approach have been published (Norman *et al.*, 1995; Anderson *et al.*, 1997; Bastiaanssen *et al.*, 1998a; Bastiaanssen *et al.*, 1998b; Mecikalski *et al.*, 1999; Allen and Bastiaanssen, 2005; Li *et al.*, 2005; Allen *et al.*, 2007; Kalma *et al.*, 2008; Kustas and Anderson, 2009; Anderson *et al.*, 2011; Cammalleri *et al.*, 2012; Colaizzi *et al.*, 2012; Maes and Steppe, 2012; Mokhtari *et al.*, 2013; Mallick *et al.*, 2014). The energy balance approach is continuously revised to minimize utilization of ancillary meteorological data needed to run the models, as described by Anderson *et al.*, (1997) using ALEXI (Atmospheric Land EXchange Inverse model). Later, using DisALEXI (Disaggregated Atmosphere Land Exchange Inverse model), ALEXI fluxes were disaggregated from continental scale to field scale (Norman *et al.*, 2003; Anderson *et al.*, 2011). The energy balance models utilize land surface temperature (LST) as a key boundary condition, which is calculated (through Eq. 1.3) from the brightness temperature ( $T_B(\theta)$ ), measured by a radiometer (Norman *et al.*, 1995):

$$T_B(\theta) = [\varepsilon(\theta)T_{RAD}(\theta)^4 + (1 - \varepsilon(\theta))T_{SKY}^4]^{\frac{1}{4}} \quad (1.3)$$

Here,  $\varepsilon(\theta)$  is the directional thermal emissivity at a view zenith angle  $\theta$ ,  $T_{RAD}$  is the radiometric surface temperature and  $T_{SKY}$  represents the hemispherical temperature of the sky.

The Penman-Monteith approach (Eq. 1.4) combines energy balance with mass transfer using standard climatological records to quantify evaporation from water surface (Allen *et al.*, 1998):

$$ET = \frac{\Delta(R_n - G) + \rho_a c_p \frac{(e_s - e_a)}{r_a}}{\Delta + \gamma \left(1 + \frac{r_s}{r_a}\right)} \quad (1.4)$$

In Eq. 1.4,  $R_n$  is net radiation received,  $G$  is the ground heat flux,  $\Delta$  represents the slope of the saturation vapour pressure and temperature relationship,  $\rho_a$  is the mean air density at constant pressure,  $c_p$  is the specific heat of the air,  $(e_s - e_a)$  is the vapour pressure deficit of the air,  $\gamma$  represents psychrometric constant,  $r_s$  and  $r_a$  are bulk surface and aerodynamic resistances. This approach was further modified by many researchers for cropped surfaces incorporating resistance factors (Allen *et al.*, 1998). Recently, Stanislaus *et al.* (2016) revealed an important omission of the radiative and sensible heat fluxes from one side of a leaf in the Penman-Monteith approach (Eq. 1.4). They proposed coupling of canopy scale latent and sensible heat with radiative exchange and ground heat flux, incorporating changes in atmospheric forcing, to derive more accurate responses of latent and sensible heat.

Land surface temperature is derived from brightness temperature measured by airborne or satellite-based radiometers (Eq. 1.3). Land surface temperature is closely linked to water and water related land surface processes, vegetation and weather related prediction modelling (Bastiaanssen *et al.*, 1998a; Kalma *et al.*, 2008). Thermal Infrared (TIR) remote sensing techniques are widely used for measuring land surface temperature. Some of the satellite missions carrying thermal infrared sensors include; Landsat4-5, Landsat7-8, AVHRR (Advanced Very High Resolution Radiometer), MODIS (Moderate Resolution Imaging Spectroradiometer). The National Aeronautics and Space Administration (NASA) has recently developed a thermal imager, TIRS (thermal infrared sensor) with two channels covering 10-12.5  $\mu\text{m}$  for measuring thermal data in continuity with previous Landsat missions (Reuter *et al.*, 2015). Landsat-8 mission carrying TIRS was launched in February 2013 with data availability to public in May 2013 (Markham *et al.*, 2013). With the launch of first Meteosat, Meteosat-1, in 1977, the Meteosat First Generation (MFG, Metosat1-7) and Meteosat Second Generation (MSG, Meteosat8-10) satellites provide data of the land surface processes in visible and thermal bands. Recently, Metosat-11 was launched in July 2015 and stored in orbit. The Spinning Enhanced Visible and Infrared Imager (SEVIRI) onboard the MSG geostationary satellites provide Land Surface Temperature, LAI, short and longwave downwelling radiation over areas including in the MSG disk (i.e., Europe, Northern Africa, Southern Africa and south America).

### **1.2.3. Water Balance (Runoff Prediction)**

Remote sensing methods are becoming crucial for quantifying consistent spatio-temporal estimates of evapotranspiration and precipitation for water balance and water resources management. Water is directly linked to many human activities (e.g., agriculture, industry,

settlement, and waste management) and has obvious impacts/control on many terrestrial ecosystems. Owing to the potential threats of climate change to water cycle/water balance (Hattermann *et al.*, 2015), proper planning and management of water resource is the need of the day. Out of plenty of water on the Earth, about 2.5% of the total water available on the earth is fresh water, and only a small amount of this fresh water is accessible due to storage in glaciers and deep in the ground (Oki and Kanae, 2006). Simultaneous occurrence of droughts and floods in different parts of the Earth has been challenging since long. Precipitation, evapotranspiration and surface runoff are integral components of the water cycle and define hydrology of an area. Most traditional methods for measuring ET and precipitation are site-specific and have no applicability beyond the point of measurement. With the advent of remote sensing technology, spatio-temporal ET and precipitation products are available operationally. Despite the spatio-temporal availability of the required data, remotely sensed tools cannot compete with *in situ* methods in terms of uncertainty. Presently a number of satellite missions are operating to provide remotely sensed relevant data for evapotranspiration (MSG, MODIS, Landsat, AVHRR etc.) and precipitation (MPE, TRMM, GPM etc.). According to Milly (1994), long-term water balance of a finite area can be determined only by local water fluctuations in the form of precipitation (water inflow source), evapotranspiration (water outflow), arbitrated by terrestrial water storage. A generalized catchment scale water balance can be expressed as equation 1.5 (Willmott *et al.*, 1985; Milly, 1994; Ponce and Shetty, 1995; Schmutge *et al.*, 2002; Montzka *et al.*, 2008b; Usman *et al.*, 2015):

$$\frac{\Delta S}{\Delta T} = P - ET - Q \quad (1.5)$$

Here,  $\Delta S/\Delta T$  is the change in water storage in soil, aquifers and reservoirs, P represents precipitation received, ET represents the amount of evapotranspiration (evaporation and transpiration) and Q represents total runoff (surface runoff, infiltration and base flow). For longer time-series (annual or more), change in terrestrial water ( $\Delta S$ ) may be considered negligible (Milly, 1994; Babin, 1995; Ponce and Shetty, 1995; Montzka *et al.*, 2008b), as the infiltrated water consequently joins stream water as base flow. Runoff patterns can also be linked with soil moisture (Scipal *et al.*, 2005), therefore, runoff dynamics are capable of providing crucial information about the soil moisture conditions in the catchment. Remote

sensing techniques for estimating operational and consistent evapotranspiration and rainfall would better suit the catchment scale water balance applications. Runoff estimates through balancing solely remotely sensed ET and rainfall may lead to better estimates of runoff fluctuations in ungauged basins or catchments with little *in situ* networks. It will facilitate the decision making system and help mitigate the adverse effects of hydrological extremes, for instance, floods due to heavy rains and water scarcity from extreme droughts.

In 1997, the Tropical Rainfall Measuring Mission (TRMM), a joint mission of the NASA and the Japan Aerospace Exploration Agency (JAXA), was launched with a design life time of 3 years to study tropical rainfall throughout the globe. State-of-the-art on-orbit active/passive instrument of the TRMM mission provided unprecedentedly valuable information on tropical weather and climate patterns for weather and climate research (NASA-TRMM). The mission came to an end on in April 2015 after providing valuable global tropical rainfall data for nearly two decades. After the successful operation of the TRMM mission, the Global Precipitation Mission (GPM) was launched by NASA and JAXA in February 2014 (NASA-GPM). GPM is a network of satellites equipped with advanced radar/radiometer system to monitor global rain and snow from space to help understand earth's water and energy cycles in more advanced manner from space. GPM's sophisticated forecasting system will help mitigate the adverse effects of weather related natural calamities. The Multi-sensor Precipitation Estimate (MPE) of EUMETSAT (European Meteorological Satellites) is an instantaneous rain rate product (EUMETSAT's-MPE; Basarudin *et al.*, 2014). The MPE algorithm is based on the assumption that cold clouds produce rain. It derives near real time rain rate from a combination of polar orbiting Special Sensor Microwave/Imager (SSM/I) measurements and brightness temperature data from Infrared channel of the Meteosat geostationary satellites (Derin and Yilmaz, 2014).

### **1.3. Remote Sensing of Land Surface Hydrology**

Remote sensing techniques (both active and passive) have enormous potentials for monitoring hydrological processes at vast spatial scales (Scipal *et al.*, 2005) and their impacts on terrestrial ecosystems. Remote sensing methods have explored operational monitoring of dynamic land surface parameters such as land surface temperature, energy fluxes, evapotranspiration, land cover changes, seasonal and evergreen vegetation, temporally covering large areas (Wagner *et al.*, 2009). The development of new satellite remote sensing techniques has made the operational availability of data required for hydrological applications possible, however, traditional methods of *in situ* observations (limited to point or footprint scale) are still important



to validate and calibrate satellite-based remotely sensed products (Dadson *et al.*, 2013). Data acquisition based on remotely sensed methods overcomes the spatio-temporal scale unavailability of hydrological variables for deriving various hydrological fluxes for land surface hydrology and several related disciplines. Many hydrological models have been revised to make efficient use of remotely sensed spatial information (Pietroniro and Prowse, 2002). Integration of remote sensing and modelling leads to better understanding the spatio-temporal patterns and variability of the water cycle and available water resources (Kite and Pietroniro, 1996; Loumagne *et al.*, 2001; Moradkhani, 2008; Xu *et al.*, 2014), especially in areas where no or less ground-based observations are available.

#### **1.4. Scientific Objectives and structure of the thesis**

The principal objective of this study is to use remotely sensed data for operational spatio-temporal estimates of vegetation and hydrological fluxes for catchment-scale water balance analysis. Throughout this dissertation, it was attempted to minimize dependency on data measured through traditional *in situ* networks to compute remotely sensed estimates. With the mentioned approaches, the *in situ* measurements were exclusively utilized to validate estimated vegetation bio-physical variable and hydrological fluxes. Estimation and validation of vegetation and hydrological fluxes from remote sensing data in the Rur catchment may lead to better estimates of these variables for global applications. In this context, this dissertation is structured into 3 main data analysis chapters. After starting with an introduction to the study (this chapter), the second chapter explains the use of remotely sensed imagery (RapidEye) for deriving and validating fine spatial resolution time-series of surface bio-physical vegetation variable, the leaf area index (LAI), which has a very significant impact on modifying land surface hydrological and energy fluxes estimates and employed as an important state variable in many hydrological and energy balance models. Different vegetation indices are analyzed for deriving LAI, also, reflectance in the red-edge band is tested in vegetation indices to evaluate its sensitivity for estimating LAI. The effects of absolute and relative atmospheric corrections are also evaluated on the time-series of RapidEye imagery. The third chapter explains spatio-temporal time-series estimation of the latent heat flux (causing evapotranspiration) using an energy balance approach. Presence of clouds causes gaps in the latent heat time-series. Therefore, a simplified regression relationship is established between calculated latent heat and satellite-based downwelling shortwave radiation to prepare a consistent time-series of latent heat to determine annual sum of catchment-scale evapotranspiration. The calculated latent heat is validated by comparing to the latent heat measured by the Eddy Covariance at five different

locations in the catchment. The fourth chapter explains prediction of sub-catchment scale annual runoff patterns throughout the catchment based on solely remotely sensed rainfall (Ground radar-based) and evapotranspiration (geostationary satellite-based) data using simplified water balance on annual and mean annual basis for better water resources management. Using the water balance on annual basis, changes in terrestrial water storage are neglected. The predicted sub-catchment scale runoff is compared to gauge data at the outlet of each sub-catchment. Finally, chapter five briefly summarizes the main conclusions derived from this study. It also covers a brief outlook for possible further research on the relevant topics.

## 2. Estimation and Validation of RapidEye-Based Time-Series of Leaf Area Index for Winter Wheat in the Rur Catchment (Germany)<sup>1</sup>

### 2.1. Introduction

Interactions among vegetation, soil, energy fluxes and carbon cycle have profound impacts on the climate system (Weiss *et al.*, 2004; Mu *et al.*, 2011). Vegetation greatly influences the climatic conditions prevailing in an area through modification of the hydrologic fluxes, such as transpiration/evaporation and interception (Arora, 2002). Therefore, indices describing vegetation properties, e.g., Leaf Area Index (LAI), contain important information that can be used to characterize vegetation dynamics and evapotranspiration fluxes in climate and hydrological models (Sellers *et al.*, 1997; Ge, 2009). To achieve better agricultural productivity, adequate information on climatic variables and physical landscape properties is required which can be provided by remote sensing in a timely and operational manner (Atzberger, 2013) from field scale to regional scale (Rembold *et al.*, 2013). LAI is an important bio-physical variable (Jonckheere *et al.*, 2004) for various models used in hydrology, climatology and crop growth, and is defined as the ratio of total upper leaf area per unit surface area of the ground [ $\text{m}^2/\text{m}^2$ ]. Accurate and timely estimates of LAI are useful for production estimation and stress evaluation of crops and environmental changes (Curran, 1983). There are several methods for measuring LAI whereof *in situ* measurements are the most reliable. However, *in situ* measurements of LAI are labor intensive and site specific so that an extrapolation to regional scale is limited. There are several approaches for estimating LAI from remotely sensed data, generally grouped into physical models and empirical models. Physical models include canopy reflectance models such as SAIL (Verhoef, 1984) and PROSAIL (Jacquemoud *et al.*, 2009) to simulate the canopy reflectance as a function of canopy variables (including LAI). For instance, Haboudane *et al.* (Haboudane *et al.*, 2004) simulated leaf and canopy reflectance spectra using PROSAIL to estimate LAI. Empirical models relate *in situ* LAI measurements to remotely-sensed vegetation indices using statistical transfer functions (Clevers, 1986; Clevers, 1988, 1989; Cohen *et al.*, 2003; Colombo *et al.*, 2003; Walthall *et al.*, 2004). Atzberger *et al.* (Atzberger *et al.*, 2010)

---

<sup>1</sup> Adapted from: Ali, M., Montzka, C., Stadler, A., Menz, G., Thonfeld, F., Vereecken, H., 2015. Estimation and Validation of RapidEye-Based Time-Series of Leaf Area Index for Winter Wheat in the Rur Catchment (Germany). *Remote Sens.* 7, 2808-2831.

analyzed two full spectrum methods using hyperspectral data [*i.e.* principal component regression (PCR) and partial least square regression (PLSR)] based on a leave-one-out (LOO) approach (Thorp *et al.*, 2007; Mirzaie *et al.*, 2014) to derive chlorophyll content in winter wheat. Despite requiring significant computational resources, models simulating the physical processes are preferred for accuracy and transferability (Deng *et al.*, 2006). Sometimes, they even outperform empirical approaches (e.g. NN, neural network approach) (Vuolo *et al.*, 2010). Asrar *et al.* (Asrar *et al.*, 1984) established a procedure to estimate LAI and FPAR (fraction of photosynthetically active radiation) from spectral reflectance. LAI and spectral reflectance are interrelated (Asrar *et al.*, 1984; Baret and Guyot, 1991) and many relationships have been developed between vegetation indices (combination of reflectance) and various vegetation parameters e.g., LAI, FPAR, chlorophyll concentration and biomass etc. (Baret and Guyot, 1991; Haboudane *et al.*, 2004). Deng *et al.* (Deng *et al.*, 2006) used the simple ratio (SR) and the reduced simple ratio (RSR) to retrieve global and regional LAI maps. According to Walthall *et al.* (Walthall *et al.*, 2004) using scaled NDVI (Normalized Difference Vegetation Index) without site specific calibration measurements is an efficient method to retrieve LAI. Area of green leaves exhibit more spatio-temporal variability and has more influence on the red and near infrared radiation in the canopy, therefore, many studies have incorporated reflectance data in these spectral regions to estimate LAI for large areas (Curran, 1983). Several VI have been developed, but I selected the most widely used indices *i.e.*, the NDVI (Rouse *et al.*, 1973) and its modified form to correct for soil reflectance the SAVI (Huete, 1988) along with their red-edge based modifications.

Presently, several remote sensors are operational that provide vegetation-related information with different spatial and temporal resolutions. Multispectral optical remote sensing techniques give more direct estimates of vegetation characteristics using the unique spectral reflectance (Xie *et al.*, 2008), whereas microwave methods provide more information on the structural characteristics of vegetation (Vereecken *et al.*, 2012). Some of the remote sensing based data sources for vegetation monitoring include: AVHRR (Advanced Very High Resolution Radiometers (Duggin and Piwinski, 1984)), Landsat (Barnett and Thompson, 1983; Chen and Cihlar, 1996; Turner *et al.*, 1999; Cohen *et al.*, 2003; Gao *et al.*, 2012; Propastin and Panferov, 2013), MODIS (Moderate Resolution Imaging Spectroradiometer), MISR (Multi-angle Imaging SpectroRadiometer), VIIRS [Visible/Infrared Imager Radiometer Suite], SPOT-VEGETATION (Systeme Pour l'Observation de la Terre), multispectral EO-1 Hyperon (Pu

and Gong, 2004) and airborne multispectral HyMap (Schlerf and Atzberger, 2006). In this study I have used the relatively new satellite system, RapidEye. To analyze the performance in estimating LAI time-series, I used RapidEye's high spatio-temporal resolution and its newly available red-edge spectral band [RE (0.690 – 0.730  $\mu\text{m}$ )]. Here I have attempted to validate the methodology previously used for MODIS LAI (Norman *et al.*, 1995; Sprintsin *et al.*, 2007; Propastin and Erasmi, 2010) to directly map LAI on high spatial resolution (5m) satellite imagery from RapidEye.

RapidEye's satellites are the first commercial satellites to include a high spatial resolution red-edge band, representing the wavelength region that exhibits rapid change in the reflectivity of vegetation from red (more absorption/low reflectance) to near infrared (NIR, maximum reflectance) (Curran, 1983; Ullah *et al.*, 2012). Numerous studies have been carried out using the red-edge spectral information. Darvishzadeh *et al.* (2009) derived LAI from (ground based) hyper-spectral vegetation indices and red-edge inflection point (REIP), but the REIP showed very poor correlation with LAI. Vuolo *et al.* (Vuolo *et al.*, 2010) used multispectral RapidEye images to estimate LAI, canopy chlorophyll content (CCC) and leaf chlorophyll content (LCC). Ehammer *et al.* (2010) used RapidEye images to determine the fraction of incident photosynthetically active radiation (FPAR) and LAI of cotton and rice using the red-edge spectral information in calculating vegetation indices, but use of the red-edge band did not improve the vegetation indices. Eitel *et al.* (2011) studied early stress detection by examining utility of the red-edge and non-red-edge vegetation indices calculated on a time-series of 22 RapidEye images of a piñon-juniper woodland in central New Mexico. Schuster *et al.* (2012) investigated the improvement of land use classification, especially in vegetation classes, using a RapidEye scene from July 2009 of a study site in Berlin (Germany). Filella and Penuelas (Filella and Penuelas, 1994) have confirmed high sensitivity of the red-edge spectral band to chlorophyll content of vegetation. Previous studies using RapidEye images (Eitel *et al.*, 2007; Ehammer *et al.*, 2010; Vuolo *et al.*, 2010) did not discuss the benefits of the multi-temporal red-edge spectral band from RapidEye (Asam *et al.*, 2013). Asam *et al.* (Asam *et al.*, 2013) derived LAI for grassland in Bavarian alpine upland (Germany) on RapidEye imagery. Here, I investigate the retrieval of LAI time-series from vegetation indices with the red-edge spectral band, and correlate with *in situ* vegetation observations covering various stages of winter wheat growth.

Radiation from the earth surface interacts strongly with the atmosphere (Hadjimitsis *et al.*, 2010). This interaction affects in particular the time-series of vegetation observations under different atmospheric conditions. Variations in atmospheric conditions, sun-target-sensor geometries and illumination conditions lead to variations in satellite images acquired on different days of the year. Two approaches have been described in the scientific literature to account for these differences: absolute and relative correction (Yang and Lo, 2000). The absolute approach needs *in situ* optical properties of the atmosphere at the time of image acquisition (Hall, 1991). In the relative method, one image (target) is radiometrically normalized with another image (reference) acquired under the best optical properties of the atmosphere (Yang and Lo, 2000). In this study, effect of both the absolute and relative atmospheric correction on a time-series of RapidEye imagery was evaluated by the performance of the LAI estimation.

The objectives of this study are: i) to evaluate the usability of RapidEye to derive LAI time-series for winter wheat, ii) to investigate the need for absolute and relative atmospheric/radiometric correction, iii) to analyze the role of the red-edge band in LAI estimation, and iv) to evaluate the impact of soil contribution on LAI time-series using SAVI as vegetation index.

## 2.2. Study Area

The area under investigation in this study is the Rur catchment (Figure 2.1), located in the Germany-Belgium-Netherlands border area, near the city of Aachen (Montzka *et al.*, 2008a; Montzka *et al.*, 2008b; Hasan *et al.*, 2014; Rudolph *et al.*, 2015). The TERENO-initiative [Terrestrial Environmental Observatories (TERENO)] has established several test sites at different locations within this catchment covering cropland (Selhausen and Merzenhausen in Figure 2.1), grassland (Rollesbroich in Figure 2.1) and forests (Wuestebach in Figure 2.1) (Zacharias *et al.*, 2011; Montzka *et al.*, 2013). The southern part of the catchment is covered by the bedrock of the Eifel Mountains with a high annual precipitation and a moderate potential evapotranspiration, while the northern part receives relatively low annual precipitation and higher potential evapotranspiration (Bogena *et al.*, 2005c). Winter wheat and sugar beet are the main crops cultivated in the area.

The Selhausen test field (area  $\approx 0.8$  hectare) is located in the southern part of the Lower Rhine Embayment, in the vicinity of the Rur river (near Dueren city) (Rötzer *et al.*, 2014). The area is covered with Quaternary sediments, mostly fluvial deposits from the Rhine/Maas River and the Rur river system (Rudolph *et al.*, 2015). They form the underlying sediments, whereas floodplain sediments belong to Pleistocene and Holocene sediments. Weakly inclined ( $<4^\circ$ ) in the east-west direction, high gravel content is present in the upper (eastern) part of the site (Weihermuller *et al.*, 2007). Due to the specific geomorphology and textural properties, the soil surface water content is highly variable in space (Weihermuller *et al.*, 2007).

The other test area, Merzenhausen (area  $\approx 7$  hectares), is located approximately 12 km away to the northwest of the Selhausen test site, near Juelich (Germany). Geomorphologically weakly inclined and structured on a high terrace of the Rur river, the area is composed of fluvial deposited loess of Pleistocene/Holocene and with small gravels up to a depth of 165 cm (Weihermueller, 2005).

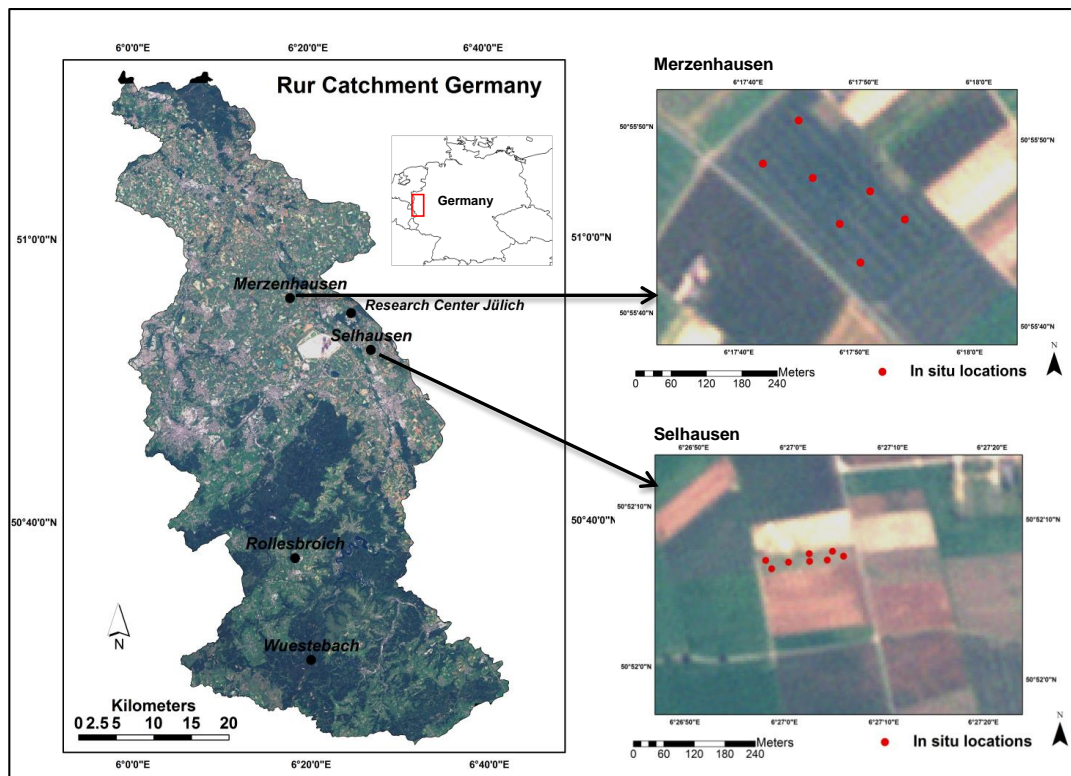


Figure 2.1. The Rur Catchment (Germany), as seen by RapidEye on June 27, 2011. Individual test sites at Selhausen and Merzenhausen are shown with sampling points.

## 2.3. RapidEye and *In Situ* Measurements

### 2.3.1. RapidEye Data

RapidEye data are available in five different spectral bands (Figure 2.2) *i.e.*, blue (0.440 – 0.510  $\mu\text{m}$ ), green (0.520 – 0.590  $\mu\text{m}$ ), red (0.630 – 0.685  $\mu\text{m}$ ), red-edge (0.690 – 0.730  $\mu\text{m}$ ) and near infrared [NIR (0.760 – 0.850  $\mu\text{m}$ )]. With a constellation of five identically constructed satellites, RapidEye is able to provide daily multispectral imagery in 6.5 m spatial resolution. During orthorectification to a map projection, the pixel size of 6.5 m with 77 km swath width (Eitel *et al.*, 2007; Ehammer *et al.*, 2010) has been resampled to 5 m and provided as Level 3A data. These Level 3A (standard L3A) products were already radiometrically corrected through sensor calibration based on the statistics from all incoming imagery data, absolute ground calibration



campaigns and image acquisitions over selected temporal calibration sites located worldwide (BlackBridgE-RapidEye, 2013). In total 24 scenes were available for 2011 and 2012 covering two winter wheat growing seasons. For validation purpose, I considered only those images for which *in situ* LAI measurements were taken. When *in situ* and satellite acquisition date did not coincide, a nearest available image (date wise) to the *in situ* measurement was used (Table 2.1).

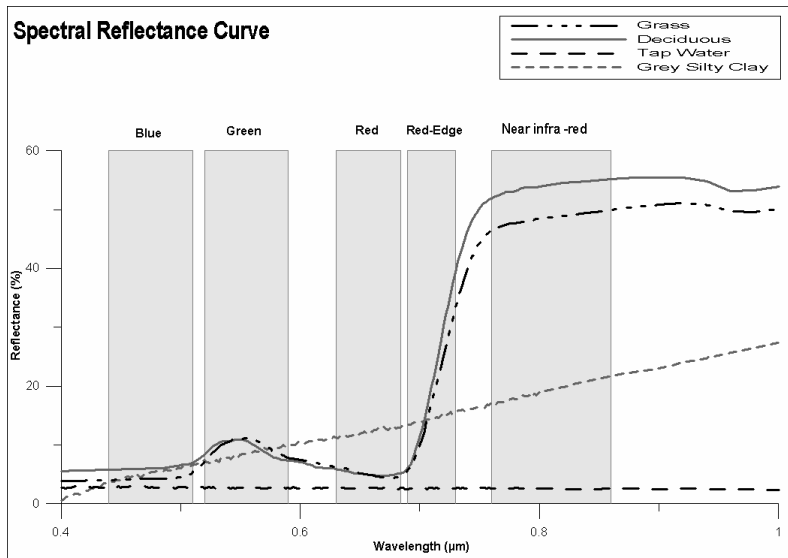


Figure 2.2. Spectral Reflectance Curves for various features of the land surface plotted against different RapidEye’s spectral channels. Vertical bars represent spectral bands of the RapidEye imagery. (Source for the reflectance data is ASTER Spectral Library).

### 2.3.2. *In Situ* LAI Measurements ( $LAI_{destr}$ )

*In situ* LAI measurements were taken at several points within the winter wheat fields using destructive method, LI-COR LI 3100C ( $LAI_{destr}$ ). Destructive methods ( $LAI_{destr}$ ) produce more reliable results and provide a reference for the calibration of non-destructive measurements (Breda, 2003) including *in situ* LAI (non-destructive) and remotely sensed LAI. The destructive methods involved physical removal of above ground vegetation within a defined area. Eight

and seven collection points were selected for *in situ* measurements inside the Selhausen and the Merzenhausen test fields respectively. The *in situ* LAI collection points were evenly distributed within the test fields (Figure 2.1) and remote sensing based LAI was acquired from the same points within the test fields. In the study area winter wheat is usually sown mid November and harvested at the end of July or start of August. Each year, the measurement campaign was started in March and carried out until the harvest time (July/August). The *in situ* data were collected twice a month during the growing season (March – July/August) of 2011 and 2012 (Stadler *et al.*, 2015). The time-series of LAI calculated on RapidEye images ( $LAI_{\text{rapideye}}$ ) were correlated with the time-series of destructive  $LAI_{\text{destr}}$ . Table 2.1 shows the availability of *in situ* LAI ( $LAI_{\text{destr}}$ ) data along with the date and time of acquisition of RapidEye. To compare *in situ* LAI (measured in a 1x1 meter space) to satellite derived LAI (on 5 meter spatial resolution), field averages were calculated.

Table 2.1. *In situ* LAI and RapidEye time-series available for this study at both test fields

| Selhausen           |                                 |                 | Merzenhausen |                                 |                 |
|---------------------|---------------------------------|-----------------|--------------|---------------------------------|-----------------|
| RapidEye            | RapidEye Acquisition Time (UTC) | Destructive LAI | RapidEye     | RapidEye Acquisition Time (UTC) | Destructive LAI |
| <b>2011</b>         |                                 |                 | <b>2011</b>  |                                 |                 |
| <b>April 07</b>     | 11:42:30                        | April 07        | April 02     | 11:37:42                        | March 29        |
| <b>April 24</b>     | 11:42:04                        | April 18        | April 07     | 11:42:27                        | April 15        |
| <b>May 10</b>       | 11:34:49                        | May 03          | May 02       | 11:28:02                        | May 04          |
| <b>May 21</b>       | 11:44:59                        | May 18          | May 21       | 11:44:56                        | May 23          |
| <b>May 30</b>       | 11:34:32                        | June 03         | June 01      | 11:39:51                        | June 11         |
| <b>June 27</b>      | 11:43:00                        | June 27         | June 27      | 11:42:57                        | June 20         |
| <b>September 01</b> | 11:28:44                        | August 30       |              |                                 |                 |
| <b>2012</b>         |                                 |                 |              |                                 |                 |
| <b>April 03</b>     | 11:39:35                        | March 30        |              |                                 |                 |
| <b>May 25</b>       | 11:30:21                        | May 25          |              |                                 |                 |
| <b>June 08</b>      | 11:47:27                        | June 12         |              |                                 |                 |
| <b>July 26</b>      | 11:32:19                        | July 24         |              |                                 |                 |

## 2.4. Approach / Methods

The main objective of this study was to derive an accurate and reliable time-series of LAI on multi-temporal RapidEye images for the two intensively investigated winter wheat fields in the Rur catchment. For this purpose, LAI was estimated through a logarithmic relationship between LAI and respective vegetation indices (e.g., NDVI, SAVI, and their respective red-edge based modifications) calculated on RapidEye images. The LAI time-series ( $LAI_{\text{rapideye}}$ ) obtained from RapidEye images was then validated with the time-series of destructive LAI measurements ( $LAI_{\text{destr}}$ ) in order to choose a more optimized vegetation index. Validation results of the LAI calculated on RapidEye imagery [standard L3A and processed images (atmospheric/radiometric correction)] with destructive  $LAI_{\text{destr}}$  were mutually compared. A flowchart (Figure 2.3) summarizes different vegetation indices and various approaches adopted for this study.

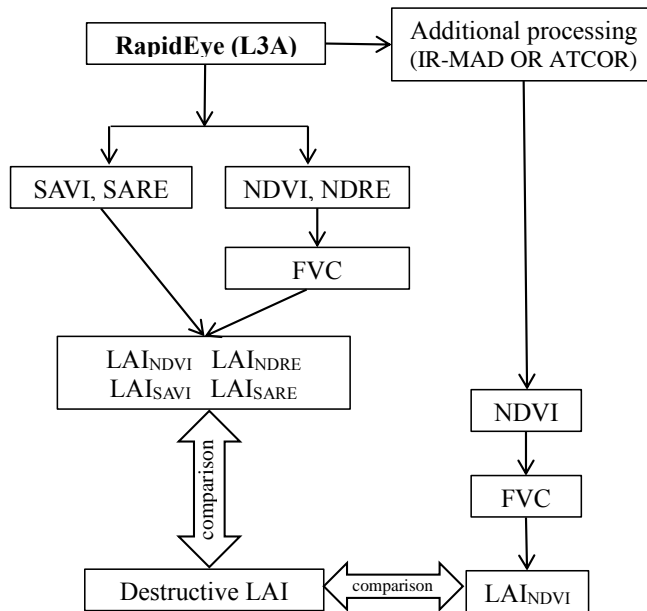


Figure 2.3. Flowchart description of the study.

#### 2.4.1. The Need for Radiometric/Atmospheric Correction

In this study, LAI computation on RapidEye imagery is based on several vegetation indices (NDVI, SAVI, NDRE and SARE). These indices are already normalized where difference of two spectral bands is normalized by the sum of the same spectral bands. Different atmospheric conditions affect the absolute reflectance of each band. Therefore the necessity for absolute and relative radiometric/atmospheric correction needs to be analyzed. Here, I focused on the correlation between *in situ* LAI ( $LAI_{destr}$ ) and three processing levels for considering the radiometric/atmospheric conditions: i) relative radiometric normalization, ii) specific absolute atmospheric correction, and iii) standard RapidEye Level 3A delivery without further processing.

The method used for relative radiometric normalization was the Iteratively Re-weighted - Multivariate Alteration Detection (IR-MAD) (Canty *et al.*, 2004; Canty and Nielsen, 2008). The band-wise IR-MAD transformation was applied to a set of bi-temporal satellite images (all 5 bands) to select invariant pixels from the two dates, *i.e.*, reference image and target image. Satellite images acquired under the most appropriate atmospheric and illumination conditions were taken as reference to normalize the target. Generally, the satellite image acquired on June 27, 2011 was used as the reference image in this study. If there was a large time gap between reference image and target images, it became difficult to find enough pseudo-invariant pixels for adequate normalization. Then, a temporally close already normalized image (April) was selected as reference image. The resultant normalized target image should appear as if it were acquired with the same sensor and atmospheric conditions of the reference image (Hall, 1991).

For absolute radiometric/atmospheric correction, the Atmospheric Correction Algorithm, ATCOR-2 (Richter, 1996a, b) was applied to the time-series of RapidEye imagery. The ATCOR-2 incorporates image center (nadir)-based date, season and landuse-based atmospheric visibility, aerosol types (*i.e.*, rural, urban, desert, maritime, spring, summer and winter *etc.*), spacecraft view angle, illumination azimuth angle and illumination elevation angle for the respective RapidEye image. Typically, ATCOR-2 is applied to flat terrains, which is given for the agriculturally intensively used region under investigation with 60 meter average elevation.

#### 2.4.2. Estimation of LAI Time-series from RapidEye

First, NDVI (Normalized Difference Vegetation Index) was calculated. NDVI is the difference of the reflectance at near infrared (NIR) and Red (RED) spectral bands normalized by the sum of the reflectance at these spectral bands (Eq. 2.1):

$$NDVI = \frac{NIR - RED}{NIR + RED} \quad (2.1)$$

NDVI (Rouse *et al.*, 1973) has wide applications providing information about vegetation and chlorophyll content in leaves. NDVI has good potential to extract useful information regarding dynamic changes in different vegetation types, making it a good indicator for investigating such changes temporally (Geerken *et al.*, 2005; Xie *et al.*, 2008). Beck *et al.* (Beck *et al.*, 2006) presented a double logistic function for modeling time-series of MODIS NDVI for higher latitude environments. Based on NDVI, the fractional vegetation cover [ $FVC_{NDVI}$  (Eq. 2.2)] was derived:

$$FVC_{NDVI} = \frac{NDVI - NDVI_s}{NDVI_v - NDVI_s} \quad (2.2)$$

as used by Zeng *et al.* and Xiao & Moody (Zeng *et al.*, 2000; Zeng *et al.*, 2003; Xiao and Moody, 2005). Here,  $NDVI_s$  represents the NDVI values for bare soil while  $NDVI_v$  represents the NDVI values at full vegetation cover in respective images of the time-series. The FVC was calculated to avoid mixed signals in satellite data (Xiao and Moody, 2005). For this purpose, NDVI was scaled between lowest  $NDVI_s$  (bare soil) and highest  $NDVI_v$  (dense vegetation) to calculate fractional vegetation cover (Eq. 2.2). For this model  $NDVI_s$  and  $NDVI_v$  were selected through histogram evaluation. Subsequently LAI was calculated through a given logarithmic relation (Eq. 2.3) between respective  $FVC_{NDVI}$  and LAI (Norman *et al.*, 1995, 1996):

$$LAI_{NDVI} = \frac{-\log(1 - FVC_{NDVI})}{k(\theta)} \quad (2.3)$$

Here,  $k(\theta)$  is the light extinction coefficient for a given solar zenith angle. The solar zenith angle ( $\theta$ ) depends on terrain geometry, solar declination, solar elevation angle, latitudinal location and day of the year (Propastin and Erasmi, 2010). The light extinction coefficient is a measure of attenuation of radiation in the canopy. The model parameter,  $k(\theta)$ , was calibrated with *in situ*

LAI (also see section 5.2). Here, the aim was first to find a good correlation ( $r$ ), whereas the estimated LAI magnitudes may not be in line with *in situ* LAI in terms of absolute prediction accuracy *i.e.*, Root Mean Square Deviation [RMSD (Eq. 2.4)]:

$$RMSD = \sqrt{\sum_{i=1}^n \frac{(LAI_{rapideye}(i) - LAI_{destr}(i))^2}{n}} \quad (4.4)$$

Number of observations ‘ $n$ ’ were different for both test sites under investigation [‘ $n = 11$ ’ for Selhausen and ‘ $n = 6$ ’ for Merzenhausen (Table 2.1)]. Second, the subsequent selection of adequate  $k(\theta)$  will focus on the improvement of the RMSD. The extinction coefficient was optimized to reduce error between *in situ* LAI ( $LAI_{destr}$ ) and  $LAI_{rapideye}$  (LAI derived from vegetation spectral indices *e.g.*,  $LAI_{NDVI}$ ).

A spatial separation into a calibration and a validation data set is performed in order to independently optimize  $k(\theta)$  and validate the  $LAI_{rapideye}$  results. Three points per field were selected for validation, whereas the point combination with the maximum distance sum was selected to adequately cover the within-field heterogeneity. The residual points were used for  $k(\theta)$  calibration.

### 2.4.3. Impact of the Soil Contribution on LAI Calculation

The soil contribution to the reflectance in crop fields can be relatively high, especially in the early stages of crop growth, which can cause inaccurate estimates of LAI. To account for this, I also utilized the Soil Adjusted Vegetation Index (SAVI), developed by Huete (Huete, 1988), as vegetation index for  $LAI_{SAVI}$  estimation. The SAVI algorithm (Eq. 2.5) (Huete, 1988) has the same structure as NDVI with a modification to correct for the influence of the soil brightness of bare soils or soils with low vegetation:

$$SAVI = \left( \frac{NIR - RED}{(NIR + RED) + L} \right) 1 + L \quad (2.5)$$

where  $L$  stands for soil brightness correction factor and its value is 0 for dense vegetation and 1 for bare soil (Huete, 1988). Here,  $L = 0.25$  was used keeping in view the status of vegetation

availability during the *in situ* measurement campaign. Like NDVI, SAVI was also used for LAI calculation using Eq. 2.3, however, unlike NDVI, SAVI is directly used in Eq. 2.3 without FVC calculation. SAVI reduces the impact of soil reflectances by incorporating the soil brightness correction factor ( $L$ ). Therefore calculation of FVC before LAI estimation was not considered here.

#### 2.4.4. Role of the Red-edge Band

The red-edge spectral band represents portion of the spectral reflectance where rapid changes occur in the reflectivity of vegetation (Figure 2.2). I have evaluated this portion of the solar spectrum (captured by RapidEye system) for vegetation by incorporating it into the vegetation indices for LAI calculation (*i.e.*, LAI<sub>NDRE</sub> and LAI<sub>SARE</sub>). Red-edge based vegetation indices *i.e.*, the Normalized Difference Red-edge index {NDRE (Eq. 2.6) (Gitelson and Merzlyak, 1994b, a; Sims and Gamon, 2002)} and the Soil Adjusted Red-edge index [SARE (Eq. 2.7)], are calculated by replacing the red spectral band (0.630 – 0.685  $\mu\text{m}$ ) with the red-edge (RE) spectral band (0.690 – 0.730  $\mu\text{m}$ ) in Eq. 2.1 (NDVI) and Eq. 2.5 (SAVI). The RE spectral band is more sensitive towards vegetation than the RED spectral band (Figure 2.2). The modified form of equations 2.1 and 2.5 for RE are shown as Eq. 2.6 and 2.7:

$$NDRE = \frac{NIR - RE}{NIR + RE} \quad (2.6)$$

$$SARE = \left( \frac{NIR - RE}{(NIR + RE) + L} \right) 1 + L \quad (2.7)$$

The new RE-based indices were renamed as Normalized Difference Red-edge index (NDRE) and Soil Adjusted Red-edge index (SARE) for NDVI and SAVI respectively.

## 2.5. Results and Discussion

### 2.5.1. Impact of the Absolute and Relative Atmospheric/Radiometric Correction

One example of an additional atmospheric correction to the L3A data set is presented in Figure 2.4. Here, it shows the difference in the visual appearance (*i.e.*, natural color composite display) of standard L3A RapidEye (A), and IR-MAD corrected (C) images from the mosaic, while part B represents the reference image for IR-MAD normalization. In figure 2.4, part A and C were

acquired on April 2, 2011 while part B was acquired on April 24, 2011. Due to the normalization procedure, part C compares well to part B. This improvement needs to be verified statistically. Changes due to the phenological cycle are visible from B to C.



Figure 2.4. Part of the standard L3A RapidEye image from April 02, 2011 (A). The reference image dated April 24, 2011 (B). IR-MAD processed image (C). RGB band combinations are 3-2-1.

For a single date, the results of different atmospheric correction strategies are highly correlated. However, the regression slope is different for each date, which affects the time-series analysis for a single pixel. Therefore, the analysis of different atmospheric correction strategies is mandatory prior to LAI time-series analysis. Before deriving LAI, different vegetation indices (*i.e.*, NDVI, SAVI, NDRE and SARE), based on the standard L3A, IR-MAD and ATCOR processed RapidEye imagery were directly compared to  $LAI_{destr}$  (Table 2.2). Table 2.2 shows higher correlation coefficients for standard L3A RapidEye spectral indices with  $LAI_{destr}$  than the IR-MAD processed vegetation indices at both test sites. However ATCOR works well at the Merzenhausen site and presents higher correlations than L3A and IR-MAD except for red-edge based indices (NDRE and SARE) where ‘*r*’ is similar for L3A and ATCOR imagery. All correlations are statistically significant ( $p < 0.05$ ) except the NDVI and SAVI (IR-MAD processed) at the Merzenhausen winter wheat field.



Table 2.2. Direct comparison of different spectral vegetation indices calculated on RapidEye L3A, IR-MAD and ATCOR processed RapidEye data with LAI<sub>destr</sub> for winter wheat at two different locations. Top numbers in each cell represent the r for the Selhausen field (2011-2012), the bottom numbers in each cell represent the Merzenhausen field (2011), in brackets the significance level (*p*-value) is given.

| Spectral Vegetation Index | Different atmospheric correction methods |               |              |
|---------------------------|--|---------------|--------------|
|                           | L3A                                      | IR-MAD        | ATCOR        |
| NDVI                      | 0.85 (0.0005)                            | 0.72 (0.0077) | 0.60 (0.040) |
|                           | 0.85 (0.033)                             | 0.77 (0.075)  | 0.90 (0.012) |
| NDRE                      | 0.90 (0.0001)                            | 0.70 (0.0104) | 0.68 (0.014) |
|                           | 0.92 (0.009)                             | 0.83 (0.040)  | 0.92 (0.007) |
| SAVI                      | 0.85 (0.0005)                            | 0.72 (0.0081) | 0.60 (0.040) |
|                           | 0.85 (0.033)                             | 0.77 (0.075)  | 0.90 (0.012) |
| SARE                      | 0.90 (0.0001)                            | 0.70 (0.0121) | 0.68 (0.014) |
|                           | 0.92 (0.009)                             | 0.83 (0.040)  | 0.92 (0.007) |

As the overall correlation relationship between the different spectral vegetation indices is similar, and for simplification, the following analysis about the need for atmospheric correction for LAI derivation is based on NDVI-related spectral analysis only. For validating RapidEye-derived LAI I used a general  $k(\theta) = 0.25$  in Eq. 2.3 for both test fields. Results are listed in Table 2.3. For these NDVI-based LAI (LAI<sub>NDVI</sub>), ATCOR produced almost similar results like IR-MAD, whereas L3A was comparatively better correlated with *in situ* LAI<sub>destr</sub>. Similar to direct comparison, LAI<sub>NDVI</sub> derived from ATCOR processed imagery gave better correlation results for Merzenhausen ( $r = 0.89$ ,  $RMSD = 2.30$ ). ATCOR processing works differently for two separate fields with different levels of surface heterogeneity in terms of vegetation health/density. However, with respect to lower RMSD and consistency of better validation results for two separate sites, the L3A RapidEye imagery are preferred. It is evident from the temporal sequence (Figure 2.5) and scatter plot (Figure 2.6) that the LAI<sub>NDVI</sub> (L3A) data have comparatively less uncertainty. The LAI<sub>NDVI</sub> after ATCOR and IR-MAD processing are more scattered as compared to the LAI<sub>NDVI</sub> from RapidEye L3A imagery (Figure 2.6). The same

scatter is visible in the temporal sequence (Figure 2.5) for LAI<sub>NDVI</sub> calculated on IR-MAD/ATCOR processed imagery. However, all the correlations are statistically significant ( $p < 0.05$ ), except the IR-MAD processed LAI<sub>NDVI</sub> ( $p = 0.138$ ) at Merzenhausen (Table 2.3), which is not significant ( $p > 0.05$ ). The LAI<sub>NDVI</sub> calculated on the standard RapidEye L3A imagery show better correlation with the destructive LAI<sub>destr</sub> [ $r = 0.82$  and  $0.78$  for Selhausen and Merzenhausen respectively (Table 2.3)].

Table 2.3. Comparison of the LAI<sub>NDVI</sub> (RapidEye standard L3A, IR-MAD and ATCOR processed) with LAI<sub>destr</sub>, in winter wheat fields at Selhausen and Merzenhausen test sites. (Numbers in bold represent the best correlation in a column while underlined number represent the insignificant correlation)

| LAI <sub>rapideye</sub> and LAI <sub>destr</sub><br>for winter wheat | Selhausen (2011-12) |         |      | Merzenhausen (2011) |              |      |
|--|---------------------|---------|------|---------------------|--------------|------|
|  | r                   | p-value | RMSD | r                   | p-value      | RMSD |
| LAI <sub>NDVI</sub> (L3A)<br>[k(0)=0.25]                             | <b>0.82</b>         | 0.0010  | 0.99 | 0.78                | 0.05         | 1.09 |
| LAI <sub>NDVI</sub> (IR-MAD)<br>[k(0)=0.25]                          | 0.71                | 0.0093  | 0.89 | 0.68                | <u>0.138</u> | 1.70 |
| LAI <sub>NDVI</sub> (ATCOR)<br>[k(0)=0.25]                           | 0.68                | 0.014   | 0.91 | <b>0.89</b>         | 0.016        | 2.30 |

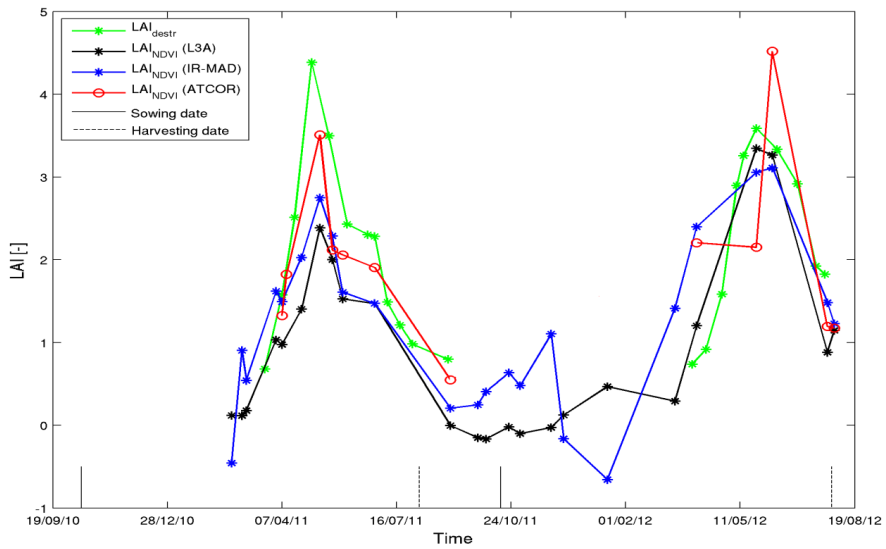


Figure 2.5. Temporal sequence of field-average destructive LAI<sub>destr</sub> with remote sensing based LAI<sub>NDVI</sub> (RapidEye L3A imagery, IR-MAD and ATCOR processed) at Selhausen winter wheat field for 2011-2012.

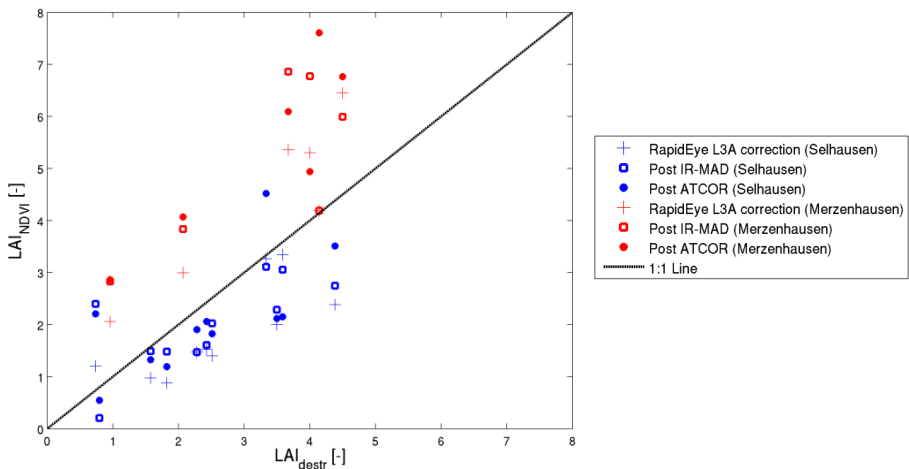


Figure 2.6. Scatter Plot of the LAI<sub>NDVI</sub> (RapidEye standard L3A, IR-MAD and ATCOR processed) with LAI<sub>destr</sub> for winter wheat field at Selhausen for 2011 and 2012 (blue) and at Merzenhausen for 2011 (red).

The preceding multispectral index of LAI (*i.e.*, NDVI) is already normalized (difference of two spectral bands is normalized by the sum of the same spectral bands). This normalization could be a possible reason why absolute and relative atmospheric/radiometric corrections (normalization) do not satisfy my basic assumption for using it. The absolute and relative atmospheric/radiometric corrections normalize satellite images to the best atmospheric and illumination conditions in an absolute and relative way respectively. It removes or minimizes the influence of varying atmospheric and illumination conditions (Richter, 1996b). Use of additional radiometric correction may generate some unavoidable uncertainties in the remote sensing data (Gu *et al.*, 2011) which is also evident in this study for ATCOR/IR-MAD processed  $LAI_{NDVI}$  with  $LAI_{destr}$  (Figures 2.5 and 2.6). The effect of additional noise due to additional absolute and relative radiometric/atmospheric processing may be more prominent when bare soil reflectance is dominant over vegetation (Figure 2.5). Moreover, the reduced sunlight during northern hemisphere winter (Figure 2.5) firstly increases the noise-to-signal ratio at a passive sensor and secondly the different light characteristics during winter cannot be completely considered with the ATCOR and IR-MAD methods. Decrease in the correlation coefficients ( $r$ ) for ATCOR/IR-MAD processed indices in Table 2.3 (except for ATCOR at Merzenhausen) is another evidence of uncertainties in LAI estimation after the application of atmospheric/radiometric correction. Factors such as radiometry, the atmosphere, topography, sun glint effect and adjacent pixel influences, necessary for radiometric correction, are not fully corrected (Abdou *et al.*, 2006), and inappropriate use (or unavailability) of these variables makes the radiometric correction more challenging (Gu *et al.*, 2011). According to Qi *et al.* (2000) the effect of atmospheric correction is not significant on remote sensing based estimation of vegetation variables. Comparison of the standard L3A and ATCOR/IR-MAD processed  $LAI_{NDVI}$  (Table 2.3 and Figures 2.5 and 2.6) with  $LAI_{destr}$  for both test sites make atmospheric/radiometric correction (ATCOR & IR-MAD) unnecessary for this validation study for winter wheat based on RapidEye Level 3A images. During on-ground processing, radiometric and sensor calibrations/corrections are applied to the Level 3A RapidEye imagery (BlackBridge-RapidEye, 2013). My results show that these calibrations (see section 2.3.1) provide satisfying LAI estimates, and there is no need to apply any further calibration/normalization like ATCOR and IR-MAD. The following analyses are therefore based on the L3A product without further atmospheric correction.

### 2.5.2. Estimation of LAI Time-series from RapidEye

The ability of RapidEye data to adequately map *in situ* LAI is based on the adequate selection of the light extinction coefficient,  $k(\theta)$ , in Eq. 2.3. I evaluated a range of  $k(\theta)$  from 0 - 1 in Eq. 2.3 for several vegetation indices of winter wheat (Figure 2.7). It was found that the value of  $k(\theta)$  has no effect on the correlation coefficient, it only affects the RMSD. Figure 2.7 shows that selecting an appropriate empirical  $k(\theta)$  will reduce RMSD, but to minimize the RMSD for various vegetation indices different  $k(\theta)$  have to be selected. The present analysis showed that the use of a single  $k(\theta)$  is challenging for heterogeneous surfaces due to varying patterns of light transmission (Aubin *et al.*, 2000) and leaf morphology (White *et al.*, 2000). Aubin *et al.* (Aubin *et al.*, 2000), White *et al.* (White *et al.*, 2000) and Propastin & Erasmi (Propastin and Erasmi, 2010) calculated  $k$  values for different vegetation types. Aubin *et al.* (Aubin *et al.*, 2000) reported a mean  $k$  value of 0.54 with lowest (0.40) in a mixed forest whereas highest (0.98) in open coniferous forest. Propastin and Erasmi (Propastin and Erasmi, 2010) calculated the extinction coefficient for an agro-forestry area using 30m Landsat TM with a mean value of 0.45 (lowest 0.32 and highest 0.68). Values of  $k$  calculated by Propastin and Erasmi (Propastin and Erasmi, 2010) were compatible with the  $k$  values for the same biome by White *et al.* (White *et al.*, 2000). Generally,  $k(\theta)$  is set at 0.50 for all types of canopies (random distribution of leaf angles (Chen *et al.*, 1997)). However, most suitable  $k(\theta)$  selection needs more experiments for different vegetation types and indices in different geographical regions for different spatial resolutions.

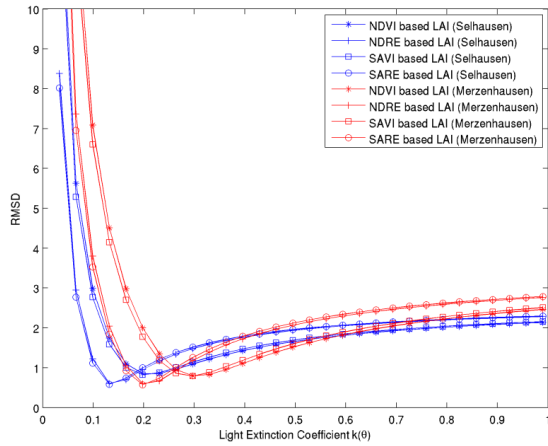


Figure 2.7. Comparison of the light extinction coefficient and RMSD for NDVI, NDRE, SAVI and SARE based LAI for the Selhausen and the Merzenhausen winter wheat fields.

Table 2.4. Validation result through splitting the sample set into calibration and validation sets for LAI estimates from RapidEye

| <b>LAI<sub>rapideye</sub> and LAI<sub>destr</sub><br/>for winter wheat</b> | Selhausen (2011-12) |          |             | Merzenhausen (2011) |          |             |
|--|---------------------|----------|-------------|---------------------|----------|-------------|
|  | <b>k(θ)</b>         | <b>r</b> | <b>RMSD</b> | <b>k(θ)</b>         | <b>r</b> | <b>RMSD</b> |
| <b>LAI<sub>NDVI</sub></b>  | 0.19                | 0.81     | 1.05        | 0.36                | 0.84     | 0.91        |
| <b>LAI<sub>NDRE</sub></b>  | 0.12                | 0.88     | 1.01        | 0.22                | 0.84     | 0.86        |
| <b>LAI<sub>SAVI</sub></b>  | 0.19                | 0.81     | 0.96        | 0.34                | 0.84     | 0.89        |
| <b>LAI<sub>SARE</sub></b>  | 0.12                | 0.88     | 0.92        | 0.21                | 0.85     | 0.84        |

The light extinction coefficient ‘ $k(\theta)$ ’ in Eq. 2.3 has no effect on the correlation coefficient, but it was sensitive towards the RMSD. Therefore, a more appropriate  $k(\theta)$  was selected for different indices and test fields in order to get a minimum possible RMSD. To evaluate the applicability of the optimized  $k(\theta)$  for producing robust results, sample points from each test site were split into calibration and validation sets. The  $k(\theta)$  was optimized using the calibration set on the basis of lowest RMSD (Table 2.4). The cross validation was performed based on the validation set using the relevant optimized  $k(\theta)$  from Table 2.4. This validation produced

consistent results as in Table 2.3. The model used here will generate reliable estimates of LAI if applied beyond the under observation test fields on the satellite data used in this study. The  $k(\theta)$  varies with spectral indices used, vegetation type and surface heterogeneity.

The  $LAI_{NDVI}$  and  $LAI_{SAVI}$  produced identical correlation results (Table 2.4) for both test sites. The  $k(\theta)$  is also similar for both the  $LAI_{NDVI}$  and  $LAI_{SAVI}$  for Selhausen [ $k(\theta) = 0.19$ ], however Merzenhausen site has higher  $k(\theta)$  and slightly different for  $LAI_{NDVI}$  and  $LAI_{SAVI}$  [ $k(\theta) = 0.36$  and  $0.34$  respectively]. Difference in  $k(\theta)$  is apparently due to the surface heterogeneity (in LAI) at both test sites. The Selhausen test field is more heterogeneous (Rudolph *et al.*, 2015) as compared to the Merzenhausen site. Vegetation at the Merzenhausen test site is more homogeneous, healthier and dense, hence more light is trapped by the canopy causing higher  $k(\theta)$  [Table 2.4]. Table 2.4 shows that using red-edge band instead of red band, reduces the light extinction coefficient,  $k(\theta)$ . For using NDVI, the effect of mixed signals (including soil reflection) is minimized by calculating FVC (Eq. 2.2). In SAVI the effect of soil reflection is reduced by incorporating soil brightness correction factor, L (Eq. 2.5). However identical results for NDVI and SAVI exhibit accuracy of the FVC calculation for NDVI and incorporating the soil brightness correction factor (L) in SAVI, in order to minimize the effect of bare soil reflections. Figure 2.8 (upper) shows identical temporal sequence for  $LAI_{SAVI}$  and  $LAI_{NDVI}$ . Apparently there was no advantage of replacing the NDVI by SAVI in this study. There is no improvement in the correlation statistics by correlating remotely sensed  $LAI_{SAVI}$  with  $LAI_{destr}$  as compared to the  $LAI_{NDVI}$  with  $LAI_{destr}$ . For smaller LAI, soil reflection (in red spectral band) affect LAI, however, for higher LAI near infrared reflectance from vegetation are dominant (Asrar *et al.*, 1984). The *in situ* LAI data were taken from dates when there were enough plants in the test fields, *i.e.* when the need for soil adjustment in a spectral vegetation index is already reduced.

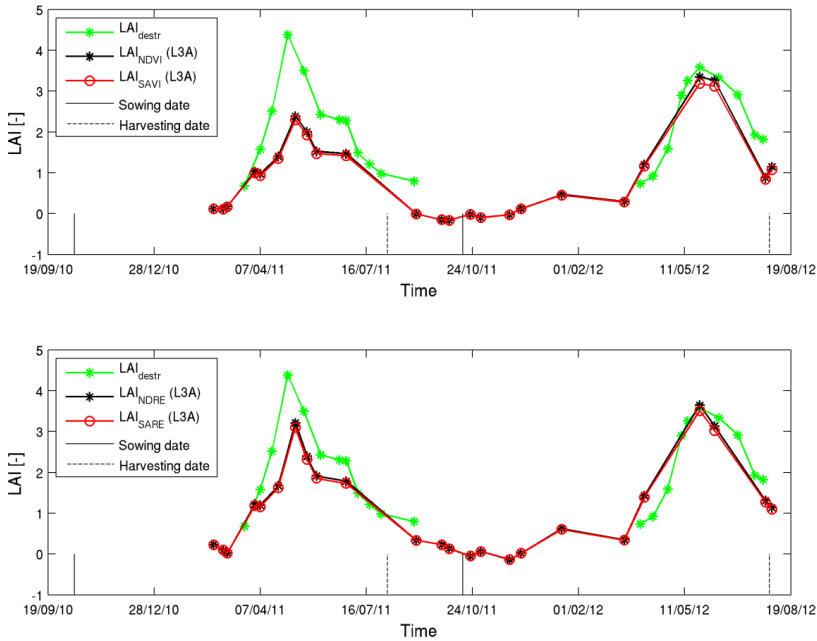


Figure 2.8. Temporal sequence of field-average destructive  $LAI_{destr}$  with remote sensing based  $LAI_{NDVI}$  and  $LAI_{SAVI}$  (upper) and  $LAI_{NDRE}$  and  $LAI_{SARE}$  (lower).

A time-series of the newly available red-edge (RE) spectral band in NDRE, SARE (section 4.4) was analyzed and used for  $LAI_{NDRE}$  and  $LAI_{SARE}$  estimation. Correlation results of the  $LAI_{NDRE}$  and  $LAI_{SARE}$  with  $LAI_{destr}$  are shown in Table 2.4, and plotted together with  $LAI_{destr}$  [Figure 2.8 (lower)]. Ehammer *et al.* (Ehammer *et al.*, 2010) analyzed the effect of incorporating RE in vegetation indices, but in all cases no improvement was reported. My analysis (Tables 2 & 4) showed two different results in correlation statistics by using RE for better estimates of vegetation indices. It is evident from Table 2.2 that NDRE and SARE (based on red-edge band) gave better correlation coefficients ( $r = 0.90$  and  $r = 0.92$  for Selhausen and Merzenhausen respectively) and higher correlation significance ( $p < 0.05$ ). Second,  $LAI_{NDRE}$  and  $LAI_{SARE}$  exhibit better correlation coefficients for Selhausen ( $r = 0.88$ ), whereas Merzenhausen presents identical correlation coefficient ( $r$ ) for all indices except  $LAI_{SARE}$  which presents  $r = 0.85$ . It was already mentioned that for utilizing  $LAI_{NDRE}$  and  $LAI_{SARE}$  a reduced light extinction coefficient,  $k(\theta)$  is optimal. Besides surface heterogeneity, spectral band selection in vegetation indices also affects the  $k(\theta)$  in Eq. 2.3. The  $LAI_{NDRE}$  and  $LAI_{SARE}$  is preferable here due to better and consistent correlation results.



Additionally the model [with a single  $k(\theta) = 0.25$ ] was applied to the northern part of the Rur catchment (on L3A data) to develop a winter wheat LAI map (Figure 2.9) for April, 2, 2011, using Rur catchment landuse map for 2011 (Lussem and Waldhoff, 2013). The LAI<sub>NDVI</sub> map has a mean LAI of 2.44 with a standard deviation of  $\pm 1.55$ , whereas the LAI<sub>NDRE</sub> has a mean LAI of 2.27 with standard deviation of  $\pm 1.25$ . The mean LAI (in both cases) for winter wheat seems very reasonable on this date from the growing season.

Previous studies (Eitel *et al.*, 2011; Schuster *et al.*, 2012; Asam *et al.*, 2013) reported improvement by using RE in vegetation based studies. According to Asam *et al.* (Asam *et al.*, 2013), red-edge based vegetation indices *i.e.*, NDVI<sub>rededge</sub> (Gitelson and Merzlyak, 1994b) and red-edge ration index 1 (Ehammer *et al.*, 2010) improve regression modelling. They declare red-edge band suitable for LAI mapping in grassland. Eitel *et al.* (Eitel *et al.*, 2011) reported improvement in conifer woodland stress detection from satellite-based red-edge monitoring. According to Eitel *et al.* (Eitel *et al.*, 2011) NDRE improves the stress detection in conifer woodland as compared to the traditionally used NDVI and green NDVI. Schuster *et al.* (Schuster *et al.*, 2012) reported improvement in classification accuracy of the vegetation classes (land use) using RE. Spectral reflectance in RE is comparatively higher than in RED, and it represents gradual increase in reflectance towards NIR (as shown in Figure 2.2). Figure 2.2 shows that the RE band is more sensitive towards vegetation (highly sensitive to the chlorophyll content (Filella and Penuelas, 1994)) than the red band. This study has shown that incorporating reflectance values captured in RE into various vegetation indices improve the validation results (Tables 2.2 and 2.4) as compared to the red-based vegetation indices (NDVI and SAVI).

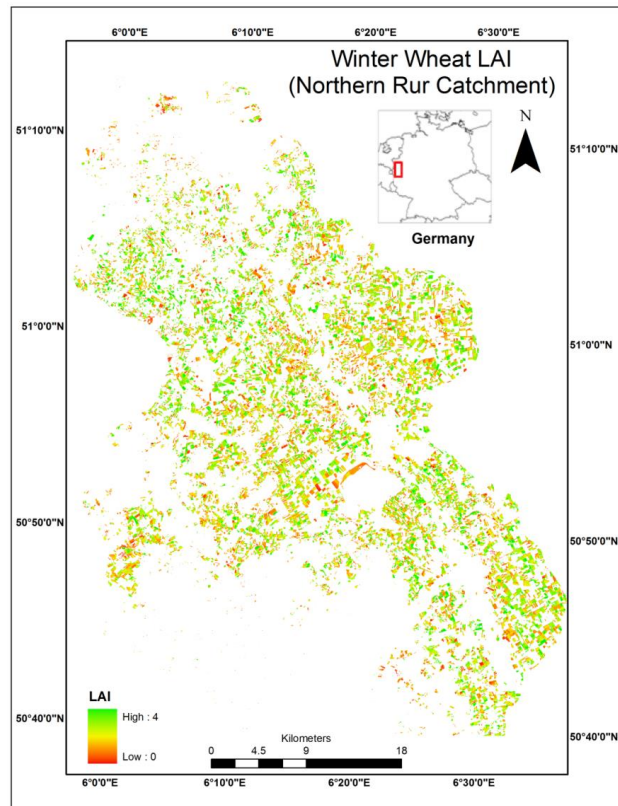


Figure 2.9. Winter wheat LAI<sub>NDRE</sub> map of the northern Rur Catchment for April, 2, 2011.

## 2.6. Conclusions and Outlook

The ability of RapidEye to provide time-series of leaf area index (LAI) for winter wheat was evaluated in the Rur catchment, Germany, focusing on two fields where destructive *in situ* LAI measurements (LAI<sub>destr</sub>) were available. It was found that time-series of various spectral vegetation indices (NDVI, NDRE, SAVI, and SARE) were highly correlated to the time-series of LAI<sub>destr</sub>, where the red-edge-based indices NDRE and SARE provided the best correlations. Three atmospheric correction methods, namely the Standard RapidEyeLevel 3A delivery, the additional relative normalization method IR-MAD as well as the additional absolute ATCOR correction, were evaluated according to their correlation to *in situ* LAI. IR-MAD processed imagery show generally lower correlation than those on L3A images. For ATCOR, the direct correlation of the spectral index to LAI<sub>destr</sub> is very high for a relatively homogeneous field

(Merzenhausen), but very low for a relatively heterogeneous field (Selhausen). Further analysis based on NDVI-related calculation of LAI found for ATCOR relatively large RMSE, whereas for the standard RapidEye L3A product a moderate RMSE was observed. With these results I came to the conclusion that additional atmospheric correction is not necessary for generating time-series of LAI from RapidEye. Therefore, the following analysis was performed on the standard L3A product only.

In general, the estimation of LAI time-series for the two fields in focus was possible with adequate accuracy. The absolute prediction accuracy in terms of RMSD to predict  $LAI_{destr}$  time-series by RapidEye was found to be sensitive to the selection of the light extinction coefficient  $k(\theta)$ . In this study the whole valid range (0-1) of  $k(\theta)$  was optimized for minimizing the RMSD between LAI estimations from RapidEye ( $LAI_{NDVI}$ ,  $LAI_{NDRE}$ ,  $LAI_{SAVI}$ , and  $LAI_{SARE}$ ) and  $LAI_{destr}$  for a calibration data set. For an independent validation data set the optimized  $k(\theta)$  was used to predict LAI.

Owing to the surface heterogeneity of the two fields in focus, varying pattern of radiation transmission (Aubin *et al.*, 2000) and selection of spectral bands, it was not possible to identify a single  $k(\theta)$  valid for large area LAI mapping. Optimum  $k(\theta)$  varied between 0.12 and 0.36, where in general it was lower for the Selhausen field than for the Merzenhausen field. Incorporating the soil contribution into the LAI estimation by the Soil Adjusted Vegetation Index (SAVI) resulted in the same optimum  $k(\theta)$  and correlation coefficient, but it did not significantly improve RMSD. However, the implementation of the red-edge spectral band in the LAI estimation by the Normalized Difference Red-edge Index (NDRE) and the newly introduced Soil Adjusted Red-edge Index (SARE) reduced the optimum  $k(\theta)$ , slightly increased the correlation coefficient and slightly reduced RMSD. Results from the present study suggest the use of the red-edge spectral band in NDRE and SARE for better estimates of LAI on RapidEye satellite imagery.

This validation study at hand was exclusively carried out for winter wheat, and further studies are needed for other crops and vegetation types (grasslands and forests). The high spatial resolution of RapidEye could be used for large scale SVAT (Soil Vegetation Atmosphere Transfer) models by providing generalized Plant Functional Type (PFT) parameters for different land cover types. Using more precise and high resolution estimates of remotely sensed LAI in hydrological and radiative transfer models may improve soil moisture (Hasan *et al.*,

2014) and evapotranspiration retrieval (Duchemin *et al.*, 2006). Remotely sensed fine resolution LAI maps identify the field scale variability of vegetation and it could be used to identify the subsoil heterogeneity in addition to geophysical methods (Rudolph *et al.*, 2015). Moreover, the analysis of the red-edge spectral band impact to LAI estimation provides basic information also for the European Space Agency's (ESA) Sentinel-2 mission (Delegido *et al.*, 2011).

### **3. A Simplified Approach to Derive Continuous Hourly Time-series of Latent Heat Flux by Remote Sensing Using a Two Source Energy Balance Model: A Case Study in the Rur Catchment, Germany<sup>2</sup>**

#### **3.1. Introduction**

Evapotranspiration (ET) is the largest component of the energy budget of the land surface, where the incoming energy is partly utilized to convert liquid water into vapour (Trenberth *et al.*, 2009; Jung *et al.*, 2010). The process of evapotranspiration transfers the largest part of water received on the Earth as precipitation back to the atmosphere (Oki and Kanae, 2006; Jung *et al.*, 2010; McMahon *et al.*, 2013). ET is a central process of the climate system (Jung *et al.*, 2010) and considered as the second largest component of the terrestrial water balance after rainfall. Being a crucial factor of the hydrological cycle, spatial and temporal distribution and variability of the evapotranspiration is essential for numerous disciplines including hydrology, meteorology, land-atmosphere interaction studies, (bio)geosciences, runoff prediction, agriculture, drought control and monitoring etc. ET can be linked to the water balance and hydrological responses and in turn to changing climate and land use (Thompson *et al.*, 2011). Evapotranspiration is the main source of transferring water (from soil and plants) back to the atmosphere, where direct evaporation from plant surface and transpiration from leaves constitute a major part of ET in addition to evaporation from the soil surface. It can be used to better explain the exchange of water and energy between soil, vegetation and atmosphere. Amount and distribution of solar radiation, surface temperature, air temperature, density and type of vegetation are the major factors controlling the rate of evapotranspiration. Wind speed affects ET by moving the water vapour away. However, wind speed is more effective under arid climatic conditions and less effective under humid conditions (Allen *et al.*, 1998; Allen *et al.*, 2005).

Conventional methods for ET estimation, e.g. pan evaporation, atmometers, lysimeters, eddy covariance (EC), scintillometers and Bowen ratio (BR) are restricted to local measurements with a footprint of at most about a hectare, and hence do not fit for regional and continental

---

<sup>2</sup>Adapted from: Ali, M., Montzka, C., Jonard, F., Jadoon, K. Z., Graf, A., Vereecken, Harry., (in preparation). A Simplified Approach to Derive Continuous Hourly Time Series of Latent Heat Flux by Remote Sensing Using a Two Source Energy Balance Model: A Case Study in the Rur Catchment, Germany.

scale spatial distribution of ET on heterogeneous land surfaces (Wang *et al.*, 2007). However, owing to their reliable and accurate results, the conventional measurements are used to validate remote sensing based ET for large geographical areas. To estimate evapotranspiration on a regional scale, energy balance approaches based on remote sensing data are widely employed (Norman *et al.*, 1995; Anderson *et al.*, 1997; Mecikalski *et al.*, 1999; Li *et al.*, 2005; Kalma *et al.*, 2008; Kustas and Anderson, 2009; Anderson *et al.*, 2011; Cammalleri *et al.*, 2012; Colaizzi *et al.*, 2012; Maes and Steppe, 2012; Mallick *et al.*, 2014). The energy balance methods do not require information about further water balance components including rainfall, runoff and moisture holding capacity of the soil (soil hydraulic properties) for estimating ET (Anderson *et al.*, 2011). Being an energy demanding process, an increase in the rate of evapotranspiration causes a decrease of surface temperature of the canopy (Maes and Steppe, 2012). If the energy storage in the canopy as well as energy advection are assumed to be negligible, ET can be calculated using the energy balance at the surface (Eq. 3.1):

$$LE = R_n - (G + H) \quad (3.1)$$

where the latent heat (LE), energy transfer related to ET, is the residual of the surface net radiation ( $R_n$ ), ground surface heat flux (G) and the sensible heat flux (H).

Energy balance methods quantify the amount of latent heat which is a part of the incoming radiation that transforms liquid water to vapour (evaporation + transpiration). Owing to its dependency on the amount and duration of incoming solar radiation and other meteorological parameters, changes in ET may occur on short time scales. Therefore, monitoring the temporal and spatial anomalies in evapotranspiration are of enormous importance for various applications. The high sensitivity of soil surface temperature ( $T_s$ ) towards soil moisture (Kustas and Anderson, 2009; Mallick *et al.*, 2014) makes soil moisture an important controlling factor for the exchange and distribution of water and energy fluxes on Earth surface (Vereecken *et al.*, 2008). Most remotely sensed soil moisture products represent only the upper few centimeters of the soil, causing comparatively larger uncertainties in areas with dense vegetation (Scipal *et al.*, 2008; Jung *et al.*, 2010).

During the last decades, significant advancements have been reported in literature utilizing remotely sensed data to map evapotranspiration beyond the limit of *in situ* footprints, ranging

from local to regional scales. Satellite-based remote sensing data provide fine to coarse resolution information in an operational manner. In addition to spatial resolution, temporal consistency of satellite-based remotely sensed data is also important for mapping evapotranspiration, as changes in latent heat may occur on short time scales (less than an hour). ET retrieval methodologies and required remotely sensed data (without or with a minimum of *in situ* data) are needed operationally. Simultaneous availability of fine spatial and high temporal resolution data are required for retrieving spatio-temporal variability in evapotranspiration. Remotely sensed energy fluxes are widely utilized in energy balance models for calculating surface energy fluxes (e.g., latent heat, sensible heat and ground heat fluxes). However, no single satellite system is capable of measuring a global coverage of required energy fluxes in both fine spatial and high temporal resolution (Anderson *et al.*, 2011; Cammalleri *et al.*, 2013; Bai *et al.*, 2015). Balancing the incoming solar radiation reaching the earth surface, Norman *et al.* (1995) proposed two types of parametrizations of the resistance to heat flow in his two source model, i.e. series and parallel. In the parallel model (not discussed here), interactions between the soil and canopy fluxes are not considered, while the series model (used here) considers this interaction (Li *et al.*, 2005). In the series formulation both the soil and vegetation affect the microclimate within the canopy air space. Anderson *et al.* (1997) evaluated the energy balance through their model ALEXI (Atmospheric Land EXchange Inverse model) using surface temperature measured with ground-based infrared thermometers. ALEXI was the extension of the two source model (TSM) of Norman *et al.* (1995) based on the concept of resistance network in series (Norman *et al.*, 2000; Anderson *et al.*, 2011). Using surface temperature measured by Geostationary Operational Environmental Satellite (GOES-8), Mecikalski *et al.* (1999) used the ALEXI model on continental scale (approximately 10 km spatial resolution). The design of ALEXI was aimed to reduce the need of ancillary meteorological data and takes advantage of high temporal resolution of geostationary satellites (Anderson *et al.*, 2011). The Disaggregated Atmosphere Land Exchange Inverse model (DisALEXI) was designed for spatial disaggregation of the ALEXI fluxes to produce relatively fine spatial resolution (field-scale) surface energy fluxes using Thermal Infrared (TIR) images (Norman *et al.*, 2003; Anderson *et al.*, 2011). Li *et al.* (2005) evaluated the parallel and series model of Norman *et al.* (1995) for a wide range of soybean and corn crops as well as soil moisture conditions, where both the parallel and series model produced similar results in terms of root mean square difference. However, the series resistance parametrizations are preferable over the parallel one for heterogeneous landscapes containing a large range of vegetation cover

(Kustas and Norman, 1999; Kustas *et al.*, 2005; Li *et al.*, 2005). Colaizzi *et al.* (2012) compared ET derived from two different forms of TSM (i.e. TSEB- $T_C$ - $T_S$  and TSEB- $T_R$ ) using component and composite soil surface and canopy temperatures. Mallick *et al.* (2014) demonstrated a novel approach called STIC (Surface Temperature Initiated Closure) which integrates the radiometric surface temperature into the Penman-Monteith (PM) equation for surface energy fluxes estimation. Due to the complexity of the process and dependency on various weather and meteorological parameters, mapping of latent heat on a high spatial and temporal scale has been challenging. In addition to complex weather variables, the presence of clouds is another factor restricting the operational availability of remotely sensed evapotranspiration.

Most applications (like agriculture, water management, etc.) require ET mapping operationally from field to regional scale with narrow time steps. To overcome the unavailability of required data, several methods are employed to get consistent hydrological data for better interpretation of hydrology in an area. Previously several studies e.g., Alavi *et al.* (2006), Chen *et al.* (2012), Cristea *et al.* (2013), Falge *et al.* (2001), Irmak *et al.* (2003), Irmak *et al.* (2006), Koozebani and Nandagiri (2007), and Mecherikunnel *et al.* (1995), used regression models to predict gap-free energy fluxes and evapotranspiration from various weather variables affecting/controlling LE (evapotranspiration). Cristea *et al.* (2013) established a relationship between evapotranspiration and key variables affecting evapotranspiration, i.e., incoming solar radiation, air temperature, relative humidity and wind speed. According to Cristea *et al.* (2013), annual and growing season average solar radiation have the strongest correlation with calculated reference ET above the United States. Gong *et al.* (2006) conducted a sensitivity analysis to evaluate the effect of various weather variables on reference evapotranspiration. Results from Gong *et al.* (2006) show that reference ET is sensitive to changes in relative humidity followed by incoming solar radiation, air temperature and wind speed in the southeast region of China. Irmak *et al.* (2003) estimated reference evapotranspiration ( $ET_o$ ) from incoming solar radiation and mean air temperature ( $R_s$ - $T_m$ ) and net radiation and mean air temperature ( $R_n$ - $T_m$ ) through multilinear regression. Along with other methods, Alavi *et al.* (2006) used multiple regression by establishing a regression relationship (by selecting 10 and 20 day time windows) between latent heat flux, available energy ( $R_n$ - $G$ ) and vapour pressure deficit ( $D$ ) to fill gaps in evapotranspiration data. Mecherikunnel *et al.* (1995) predicted outgoing longwave (OLR) and shortwave (SW) radiation using multiple linear models based on meteorological parameters during cloudy and cloudless conditions. Chen *et al.* (2012) used multiple regression with a



second order polynomial equation to estimate missing latent heat (LE). However, some of these studies were extensively based on ground measurements (Cristea *et al.*, 2013), limited to daily time steps (Irmak *et al.*, 2003; Kooover and Nandagiri, 2007), only focused on gap-filling techniques (Falge *et al.*, 2001; Alavi *et al.*, 2006; Chen *et al.*, 2012), or restricted to sensitivity analyses only (Gong *et al.*, 2006; Irmak *et al.*, 2006).

The Satellite Application Facility on Land Surface Analysis (Land-SAF, <http://landsaf.meteo.pt/>) of European Meteorological Satellites (EUMETSAT) provides energy fluxes and vegetation data operationally, however, cloud presence reduced the number of hourly available estimates of latent heat. Keeping in view the sensitivity of downward shortwave radiation towards ET (Cristea *et al.*, 2013) and its temporal consistency, downward shortwave radiation from Land-SAF was taken in this study as a main controlling meteorological variable to derive latent heat/ET. The relationship between latent heat estimates from the energy balance approach and downward shortwave radiation provides a linear function to estimate a complete hourly spatio-temporal time-series of latent heat for a period of five years. I have attempted to reduce the dependency on *in situ* data by performing a regression analysis between remotely sensed latent heat (from the energy balance approach) and shortwave radiation (from Land-SAF).

This study aimed to develop hourly consistent spatio-temporal time-series of evapotranspiration (ET) by applying the two source land-atmosphere energy exchange model of Norman *et al.* (1995) under humid conditions in the Rur catchment. I evaluated the use of satellite-based remotely sensed LAI, land surface temperature and net radiation for estimating the time-series of latent heat (causing ET). For this purpose, two approaches were used in this study. First, an hourly time-series of latent heat flux ( $LE_{EBM}$ ) was calculated using the two source energy balance approach (series formulations) using energy fluxes and vegetation information. Secondly, an empirical relation was established between calculated latent heat ( $LE_{EBM}$ ) and satellite-based down-welling shortwave radiation in order to estimate a consistent (gap-free) spatio-temporal time-series of latent heat ( $LE_{REG}$ ) for the study area. The calculated time-series of latent heat requires only remote sensing data and these estimates ( $LE_{EBM}$  and  $LE_{REG}$ ) are subsequently compared to reference latent heat measured through Eddy Covariance ( $LE_{EC}$ ) to quantify the accuracy of the LE estimates at five test sites in the Rur catchment, Germany.

### 3.2. Study Area

This study was also carried out in the Rur catchment, Germany (also see section 2.2). Within the Rur catchment, various test sites have been established at different locations by the TERENO initiative [Terrestrial Environmental Observatories (<http://teodoor.icg.kfa-juelich.de/overview-de>)]. The Soil Moisture and Ocean Salinity (SMOS) mission of the European Space Agency (ESA) and Soil Moisture Active-Passive (SMAP) mission of the National Aeronautics and Space Administration (NASA) are using this catchment as a validation area (Montzka *et al.*, 2013; Han *et al.*, 2015; Montzka *et al.*, 2016; Colliander *et al.*, submitted). I have selected five sites, namely, the lowland crop sites Selhausen and Merzenhausen, the low- and upland grassland sites Selhausen-Ruraue and Rollesbroich, and the forest site Wuestebach (Figure 3.1) (Zacharias *et al.*, 2011; Graf *et al.*, 2013; Montzka *et al.*, 2013; Graf *et al.*, 2014; Eder *et al.*, 2015) as validation sites for satellite-based ET estimates. The Selhausen, Merzenhausen, and Selhausen-Ruraue test fields are located in the northern part of the catchment covered by crops; mainly winter wheat and sugar beet (Reichenau *et al.*, 2016). Soils at the Selhausen area (the northern part of the Lower Rhine Embayment) exhibit a relatively high heterogeneity owing to the fraction of coarse material and grain size distribution (Rudolph *et al.*, 2015). According to Weihermueller (2005), the Merzenhausen soil is composed of fluvial deposited loess with Pleistocene/Holocene and located on a high terrace of the Rur river. The Rollesbroich and Wuestebach sites are located in the southern part of the catchment which is mostly covered by the bedrock of the Eifel Mountains. The Rollesbroich site is mainly occupied by grasslands surrounded by forests in the vicinity and the Wuestebach site is dominantly covered by forests. The southern part of the catchment receives high annual precipitation with a moderate potential evapotranspiration (850–1300 and 450–550  $\text{mm}\text{year}^{-1}$ , respectively) as compared to the northern part that receives relatively low annual precipitation and has a higher potential evapotranspiration (650–850 and 580–600  $\text{mm}\text{year}^{-1}$ , respectively) (Bogena *et al.*, 2005b; Han *et al.*, 2015).

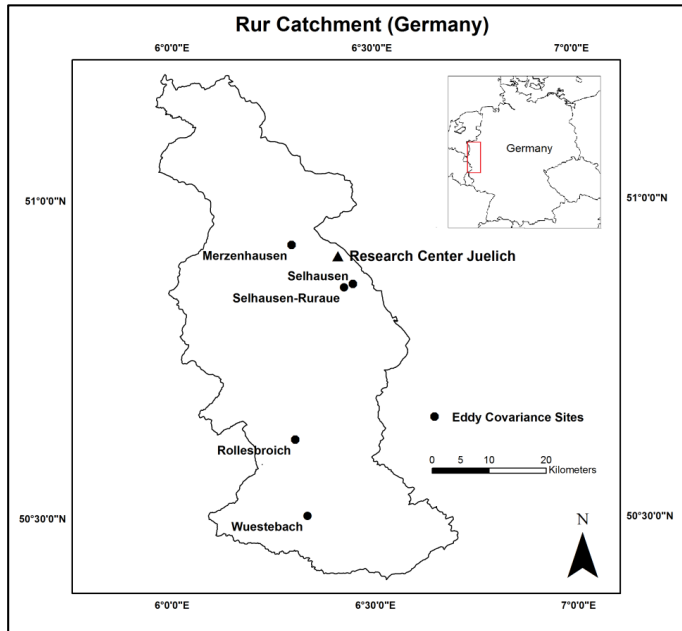


Figure 3.1. Rur Catchment, Germany, with Eddy Covariance sites.

### 3.3. Data and Methods

#### 3.3.1. *In Situ* Flux Measurements

*In situ* flux data are available from various Eddy Covariance (EC) sites in the Rur Catchment, Germany (also see section 3.2 and Figure 3.1). EC-based latent heat ( $LE_{EC}$ ), sensible heat ( $H_{EC}$ ), shortwave radiation, longwave radiation and net radiation data from 2011 to 2015 were used except for the Wuestebach site (available since 2013.) Shortwave radiation data at the Selhausen-Ruraue site were missing and therefore excluded from the comparison analysis of satellite-based shortwave radiation with *in situ* measurements. Latent and sensible heat fluxes are computed on 30 minute intervals (Graf *et al.*, 2013), whereas the state variables (shortwave and longwave radiation) are averaged on 10 minute intervals. Hourly mean values were calculated for further processing.

### 3.3.2. Satellite-based Fluxes and Evapotranspiration Calculation

A complete description of the approach is represented by the flow chart on Figure 3.2. For estimating evapotranspiration, I mainly used relevant data acquired by the Spinning Enhanced Visible and Infrared Imager (SEVIRI) onboard the Meteosat Second Generation (MSG) geostationary satellites at a spatial resolution of 3km/pixel at nadir, i.e., ~5km for the area under investigation with an imaging repeat cycle of 15 minutes (Trigo *et al.*, 2011). Data required for my model are leaf area index (LAI) and albedo, provided on a daily basis, land surface temperature estimated on 15 minute intervals, whereas energy fluxes, i.e. downwelling surface shortwave flux (DSSF) and downwelling surface longwave flux (DSLFL) are estimated on 30 minute intervals. Temporal consistency make Land-SAF based LAI, albedo, DSSF, DSLFL and LST data an optimal candidate for generating long-term time-series at catchment scale. DSSF is the radiative energy in the spectral wavelength region of 0.3  $\mu\text{m}$  and 4.0  $\mu\text{m}$  reaching the earth's surface. It is the integration of spectral irradiance over the wavelength interval 0.3  $\mu\text{m}$  and 4.0  $\mu\text{m}$  computed from level 1.5 SEVIRI data in the short-wave spectral regions corresponding to 0.6  $\mu\text{m}$ , 0.8  $\mu\text{m}$  and 1.6  $\mu\text{m}$  (near infrared) (Trigo *et al.*, 2011). With clear-sky conditions, DSSF is directly estimated and involves parametrization for the effective transmittance of the atmosphere (Trigo *et al.*, 2011) based on the atmospheric transmittance and spherical albedo calculation methodology of Frouin *et al.* (1989). DSSF estimation under cloudy-sky conditions depends on a simplified physical description of the radiation transfer in the cloud-atmosphere-surface system of Gautier *et al.* (1980) and Brisson *et al.* (1999) based on cloud transmittance, cloud albedo and atmospheric transmittance between surface and clouds. Further details can be found on Land-SAF\_DSSF (2011). DSLFL is the total irradiance in the infrared spectral region (4-100  $\mu\text{m}$ ). Bulk parametrization schemes, merging clear-sky formulations with cloudy-sky formulations, are employed for DSLFL estimation (Trigo *et al.*, 2011). Land surface temperature (LST) data are measured every 15 minutes. Land surface temperature (LST) is measured from the thermal infrared window (MSG/SEVIRI channels IR 10.8, IR12.0 and MetOP/AVHRR-3 channels 4 and 5) using the generalized split-window (GSW) algorithm of Wan and Dozier (1996) through differential absorption in adjacent infrared bands and land surface emissivity correction for atmospheric effects (Land-SAF\_LST, 2015). Hourly averaged values of DSSF, DSLFL (from 30 min) and LST (15 min) were calculated. SEVIRI on board of MSG provide only downwelling fluxes (i.e. DSSF and DSLFL). The

Upwelling surface shortwave flux (USSF) was calculated as a function of albedo ( $\alpha$ ) using equation 3.2:

$$USSF = \alpha * DSSF \quad (3.2)$$

whereas the upwelling surface longwave flux (USLF) was calculated according to Stefan Boltzmann's law (Eq. 3.3):

$$USLF = \epsilon \sigma T^4 \quad (3.3)$$

from surface temperature (T), the Stefan Boltzmann constant ( $\sigma = 5.6703 \times 10^{-8} \text{ W/m}^2\text{K}^4$ ) and surface emissivity ( $\epsilon$ ).

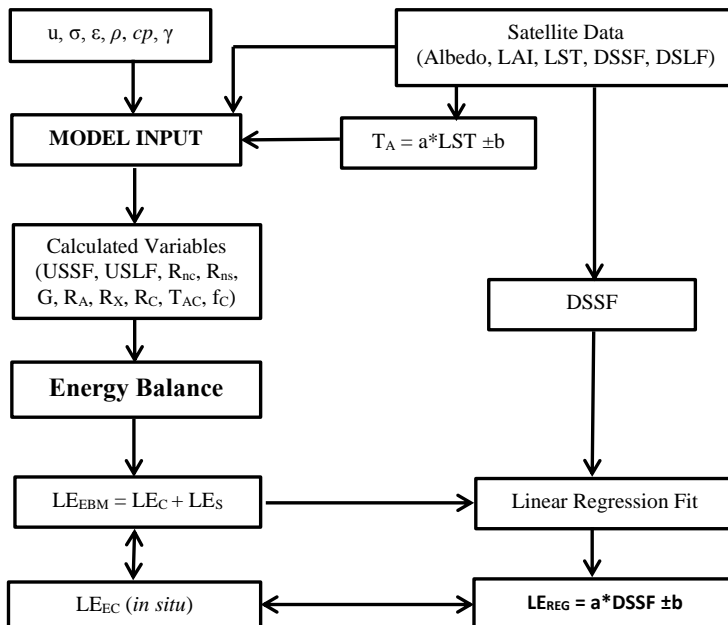


Figure 3.2. Flowchart description of the study for estimating evapotranspiration.

The energy balance model used in this study describes the exchange of energy fluxes between land surface (soil + vegetation) and atmosphere using a two-source energy balance approach. It is based on the distribution of energy [net radiation ( $R_n$ )] on the earth surface (Eq. 3.1) and derivation of the available latent heat [LE ( $\lambda E$ )] which is associated with the process of evapotranspiration (transpiration and evaporation) from plants and soil (Anderson *et al.*, 2007; Maes and Steppe, 2012). The available net radiation is the difference between downwelling and upwelling radiation of all wavelengths [Eq. 3.4 (Mecikalski *et al.*, 1999; Anderson *et al.*, 2000)]:

$$R_n = (DSSF - USSF) + (DSL F - USL F) \quad (3.4)$$

$R_{n,c}$  (Eq. 3.5) represents the net radiation divergence in the canopy (vegetation) and computed as the difference of net radiation ( $R_n$ ) and  $R_{n,s}$ :

$$R_{n,c} = R_n - R_{n,s} \quad (3.5)$$

where  $R_{n,s}$  is the component penetrating to the soil [Eq. 3.6 (Norman *et al.*, 1995)]:

$$R_{n,s} = R_n e^{0.9 \log(1-f_c)} \quad (3.6)$$

$f_c$  (Eq. 3.7) is the fractional vegetation cover (Norman *et al.*, 1995):

$$f_c(\theta) = 1 - \exp\left(\frac{-0.5 LAI}{\cos(\theta)}\right) \quad (3.7)$$

Here, the subscripts s and c represent soil and canopy flux components. Vegetation cover highly affects the distribution of incoming net radiation into canopy and soil components. Accurate partitioning of the incoming solar radiation ( $R_n$ ) and land surface temperature (LST) between soil and vegetation in two-source energy balance models promise better estimate of fluxes (LE, H and G). In literature (Norman *et al.*, 1995; Anderson *et al.*, 1997; Kustas and Norman, 1999; Mecikalski *et al.*, 1999; Norman *et al.*, 2000; Norman *et al.*, 2003; Maes and Steppe, 2012), various approaches have been presented regarding the partitioning of the incoming radiation on the earth surface. However, due to the spatio-temporal unavailability of several parameters

(presented in literature) for hourly calculations, I adopted the generalized form (equations 3.5 - 3.7) of splitting the incoming radiation into canopy and soil component.

To run the energy balance model, radiometric land surface temperature (LST) is a key boundary condition used as composite of soil and canopy temperature ( $T_s$  and  $T_c$ ). The  $T_s$  and  $T_c$  parameters were calculated using a linear simplification approach as described by Norman et al. (1995). Being a key parameter in land surface processes, LST have control over upward radiation affecting the amount of sensible and latent heat (Aires *et al.*, 2001). LST is given by Eq. 3.8:

$$LST = [f_c(\theta)T_c^4 + (1 - f_c(\theta))T_s^4]^{\frac{1}{4}} \quad (3.8)$$

considering the fraction of vegetation.  $T_s$  and  $T_c$  are calculated through Eq. 3.8 using the linear simplification method proposed by Norman et al.(1995). Eq. 3.9 computes temperature within the canopy ( $T_{AC}$ ) by relating it to various resistances to heat flow and canopy/soil components of the land surface temperature:

$$T_{AC} = \left( \frac{\frac{T_A}{R_A} + \frac{T_S}{R_S} + \frac{T_C}{R_X}}{\frac{1}{R_A} + \frac{1}{R_S} + \frac{1}{R_X}} \right) \quad (3.9)$$

Here,  $R_s$ ,  $R_A$ , and  $R_X$  are the resistance to the heat flow above soil, aerodynamic resistance and heat resistance to the leaves of the canopy, respectively. Aerodynamic resistance ( $R_A$ ) and resistance ( $\text{sm}^{-1}$ ) to heat flow from canopy ( $R_X$ ), and soil ( $R_s$ ) were calculated using original formulation of Norman et al.(1995).

Spatio-temporal ambient air temperature ( $T_A$ ) was estimated using linear regression (Eq. 3.10):

$$T_A = a LST + b \quad (3.10)$$

where ‘a’ and ‘b’ are the regression coefficients of land surface temperature with air temperature measured at various ground-based meteorological stations in the study area and surroundings.

Soil heat flux ( $G$ ) is another important variable of the energy balance model. Estimates of  $G$  will affect the overall model fluxes and any error in estimating  $G$  will lead to bias in the latent

and sensible heat fluxes (Choudhury *et al.*, 1987). However, presence of vegetation will minimize this bias (Choudhury *et al.*, 1987).  $G$  is commonly calculated as a constant fraction of the soil component of net radiation [ $G/R_{n,s}$  (Eq. 3.11)]:

$$G = 0.35 R_{n,s} \quad (3.11)$$

Using the aforementioned remotely sensed data, two approaches were employed to quantify latent heat flux.

### 3.3.2.1. Approach 1

First, latent and sensible fluxes were calculated using the two source energy balance method. The two source energy balance model has the ability to compute surface energy balance for soil and vegetated canopy separately. The canopy and soil components of sensible heat are derived as function of temperature differences (Norman *et al.* 1995) using calculated component temperatures. The canopy component of sensible heat ( $H_C$ ) was computed using temperature gradient between canopy ( $T_C$ ) and within the canopy ( $T_{AC}$ ) temperatures (Eq. 3.12):

$$H_C = \rho C_P \frac{T_C - T_{AC}}{R_X} \quad (3.12)$$

and the soil component of sensible heat ( $H_S$ ) was computed from temperature gradient between soil ( $T_S$ ) and within canopy ( $T_{AC}$ ) temperatures (Eq.3.13):

$$H_S = \rho C_P \frac{T_S - T_{AC}}{R_S} \quad (3.13)$$

Composite sensible heat ( $H_{EBM}$ ) was computed from  $H_C$  and  $H_S$  using Eq. 3.14:

$$H_{EBM} = H_C + H_S \quad (3.14)$$



In these equations,  $\rho$  is the air density,  $C_p$  is the specific heat of the air. By applying the component energy balance, soil evaporation (LEs) and canopy transpiration (LEc) are computed separately. LEs was calculated as residual of the soil component of net radiation (Rns), soil sensible heat (Hs) and ground heat flux (G) (Eq. 3.15):

$$LE_s = R_{ns} - G - H_s \quad (3.15)$$

whereas, LEc was calculated as the residual of canopy component of net radiation (Rnc) and canopy sensible heat (Hc) (Eq. 3.16):

$$LE_c = R_{nc} - H_c \quad (3.16)$$

Composite latent heat (LE<sub>EBM</sub>, causing evapotranspiration) was computed as final output of the energy balance model using equation 3.17:

$$LE_{EBM} = LE_c + LE_s \quad (3.17)$$

### 3.3.2.2. Approach 2

The presence of clouds reduces the number of available hourly variables, causing large temporal and spatial gaps in the output time-series of LE<sub>EBM</sub>. Therefore, in addition to the aforementioned energy balance approach, a second approach was developed in this study by establishing an empirical relationship (Eq. 3.18) between LE<sub>EBM</sub> and DSSF:

$$LE_{REG} = a_i DSSF + b_i \quad (3.18)$$

The regression coefficients ( $a_i$  and  $b_i$ ) were calculated by comparing hourly latent heat flux (LE<sub>EBM</sub>, calculated with approach 1) and remotely sensed downwelling surface shortwave flux (DSSF) from satellite. Based on this relationship, a complete spatio-temporal (gap-free) time-series of latent heat flux for the Rur catchment was estimated using equation 3.18. Latent heat (LE<sub>REG</sub>) was converted to equivalent evapotranspiration units (mm $\cdot$ year<sup>-1</sup>) from energy units (Wm<sup>-2</sup>) using 28.4 Wm<sup>-2</sup> = 1 mmday<sup>-1</sup> (Allen *et al.*, 1998; Allen *et al.*, 2005) with subsequent

conversion to  $\text{mmhour}^{-1}$  and  $\text{mmyear}^{-1}$ . Latent heat fluxes measured through Eddy Covariance ( $\text{LE}_{\text{EC}}$ ) from the five test sites (Figure 3.1), Selhausen, Merzenhausen, Selhausen-Ruraue, Rollesbroich and Wuestebach were only used as reference to assess the model performance [i.e. calculated  $\text{LE}_{\text{EBM}}$  (approach 1) and  $\text{LE}_{\text{REG}}$  (approach 2)] by calculating the correlation coefficient ( $r$ ), the root mean squared difference [RMSD (Eq. 3.19)], the mean bias error [MBE (Eq. 3.20)], and the mean absolute error [MAE (Eq. 3.21)]:

$$\text{RMSD} = \sqrt{\frac{1}{n_v} \sum_{i=1}^{n_v} (M_i - O_i)^2} \quad (3.19)$$

$$\text{MBE} = \frac{1}{n_v} \sum_{i=1}^{n_v} M_i - O_i \quad (3.20)$$

$$\text{MAE} = \frac{1}{n_v} \sum_{i=1}^{n_v} |M_i - O_i| \quad (3.21)$$

Here,  $M$  is modelled ( $\text{LE}_{\text{EBM}}$  and  $\text{LE}_{\text{REG}}$ ) and  $O$  is observed (EC) values, while  $n_v$  is the number of available observations for validation. RMSD is the sum of the squared difference of modelled and observed LE and is more sensitive to outliers in the dataset (Willmott and Matsuura, 2005). According to Willmott and Matsuura (2005), MAE is more appropriate to assess model performance as compared to RMSD. To minimize the effect of outliers in the dataset, MAE were also calculated in addition to RMSD and MBE.

### 3.4. Results and discussion

#### 3.4.1. Validation of $\text{LE}_{\text{EMB}}$ and $\text{H}_{\text{EMB}}$ (Approach 1)

Net radiation ( $R_n$ ) is the core variable (key quantity) of energy balance models for deriving latent and sensible heat fluxes. Before using the net radiation derived from satellite-based fluxes (through Eq. 3.4), its accuracy was evaluated by comparing it to *in situ* measurements by the radiation equipment (NR01, Hukseflux, NL) of the eddy-covariance stations.

Table 3.1. Correlation statistics of hourly *in situ* and remotely sensed net radiation ( $R_n$ ) for Eddy Covariance sites in the Rur catchment, Germany, for five years (2011-2015).

| $R_n$ ( $Wm^{-2}$ ) 2011-15 |         |      |       |       |       |
|-----------------------------|---------|------|-------|-------|-------|
| Statistics                  | $n_v$   | $r$  | RMSD  | MBE   | MAE   |
| Selhausen                   | 11896   | 0.97 | 45.92 | 8.97  | 31.44 |
| Merzenhausen                | 7430    | 0.97 | 42.61 | 12.58 | 29.73 |
| Selhausen-Ruraue            | No Data |      |       |       |       |
| Rollesbroich                | 14124   | 0.97 | 48.59 | 11.69 | 33.15 |
| Wuestebach (2013-12)        | 6239    | 0.97 | 54.26 | 4.28  | 37.83 |

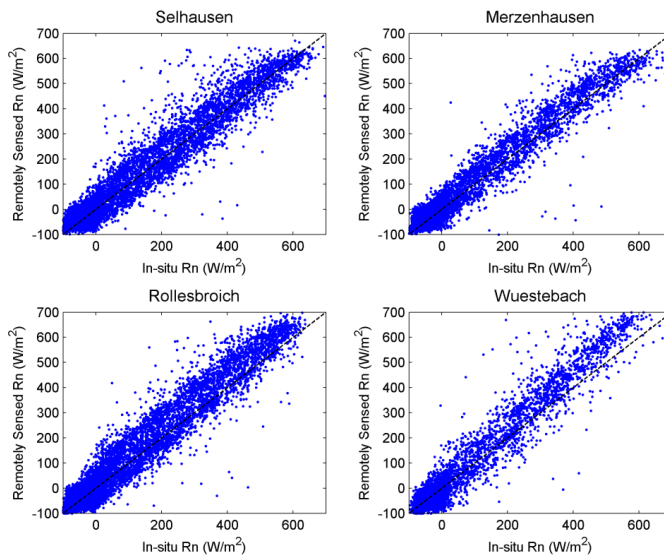


Figure 3.3. Scatter plots of hourly *in situ* and remotely sensed net radiation ( $R_n$ ) for Eddy Covariance sites in the Rur catchment, Germany, for five years (2011-2015).

Scatter plots (Figure 3.3) and correlation statistics in Table 3.1 demonstrate that satellite-derived net radiation agrees well with *in situ* net radiation at four test sites. Correlation coefficient ( $r$ ), RMSD, MBE, and MAE at Selhausen, Merzenhausen, Rollesbroich and Wuestebach for satellite-based net radiation and *in situ*  $R_n$  are enlisted in Table 3.1. The

Selhausen-Ruraue site was excluded here due to *in situ* data unavailability. The calculated  $R_n$  from remotely sensed energy fluxes can be a satisfactory candidate for running the energy balance model. They were incorporated in the energy balance models used in this study to retrieve time-series of latent and sensible heat. The hourly retrieved latent heat ( $LE_{EBM}$ ) and sensible heat ( $H_{EBM}$ ) were compared to *in situ* latent and sensible heat measured by Eddy Covariance ( $LE_{EC}$  and  $H_{EC}$ ) at the five Eddy Covariance sites of the Rur catchment for the years 2011 through 2015 (Table 3.2a,b and Figure 3.4 and 3.5).

Table 3.2. Correlation statistics on hourly *in situ* latent and sensible heat fluxes ( $LE_{EC}$  and  $H_{EC}$ ) and remotely sensed latent and sensible heat ( $LE_{EBM}$  and  $H_{EBM}$ ) for the Eddy Covariance sites in the Rur catchment, Germany, for five years (2011-2015).

| <b>a) <math>LE_{EBM}</math> and <math>LE_{EC}</math> (<math>Wm^{-2}</math>) 2011-15</b> |                         |          |             |            |            |
|---|-------------------------|----------|-------------|------------|------------|
| <b>EC Stations</b>  | <b><math>n_v</math></b> | <b>r</b> | <b>RMSD</b> | <b>MBE</b> | <b>MAE</b> |
| <b>Selhausen</b>  | 9110                    | 0.83     | 63.41       | 16.26      | 39.63      |
| <b>Merzenhausen</b>   | 10841                   | 0.80     | 75.41       | 28.91      | 44.67      |
| <b>Selhausen-Ruraue</b>   | 8249                    | 0.84     | 66.16       | 18.89      | 42.06      |
| <b>Rollesbroich</b>   | 9484                    | 0.90     | 118.25      | 62.09      | 70.96      |
| <b>Wuestebach (2013-15)</b>   | 3947                    | 0.85     | 150.00      | 85.95      | 89.89      |
| <b>b) <math>H_{EBM}</math> and <math>H_{EC}</math> (<math>Wm^{-2}</math>) 2011-15</b>   |                         |          |             |            |            |
| <b>Selhausen</b>  | 9238                    | 0.74     | 40.25       | 5.77       | 29.35      |
| <b>Merzenhausen</b>   | 11069                   | 0.78     | 37.73       | -5.84      | 26.78      |
| <b>Selhausen-Ruraue</b>   | 8424                    | 0.74     | 39.66       | 1.78       | 28.93      |
| <b>Rollesbroich</b>   | 9927                    | 0.61     | 43.81       | -20.09     | 30.15      |
| <b>Wuestebach (2013-15)</b>   | 4524                    | 0.80     | 68.43       | -46.97     | 50.91      |

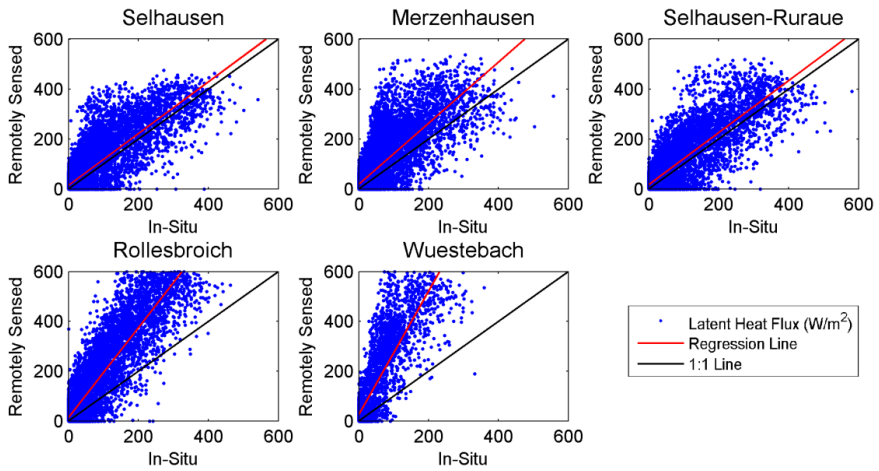


Figure 3.4. Scatter plots of hourly  $LE_{EC}$  (*in situ*) and  $LE_{EBM}$  (energy balance model) for the Eddy Covariance sites in the Rur catchment, Germany, for the years 2011-2015.

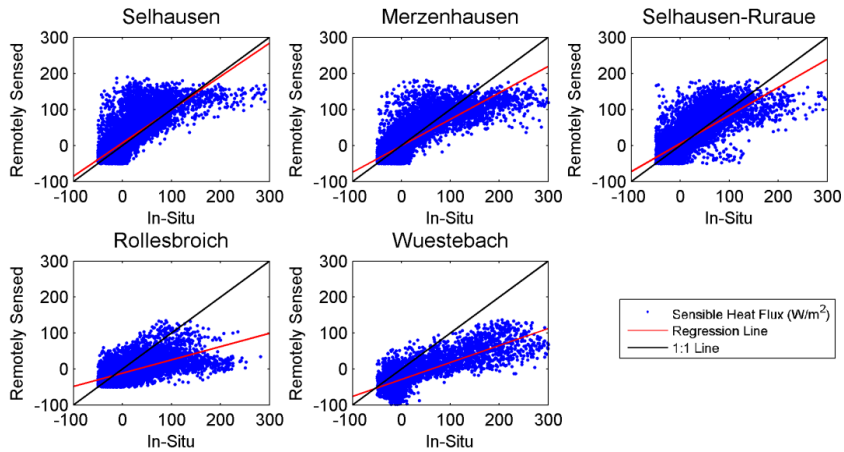


Figure 3.5. Scatter plots of hourly  $H_{EC}$  (*in situ*) and  $H_{EBM}$  (energy balance model) for the Eddy Covariance sites in the Rur catchment, Germany, for the years 2011-2015.

Due to partial unavailability of temporally coinciding calculated ( $LE_{EBM}$ ) and reference latent heat ( $LE_{EC}$ ), the available  $LE_{EBM}$  observations for validation ( $n_v$ ) were less than the total number

of  $LE_{EBM}$  observations. Accuracy of the calculated latent heat ( $LE_{EBM}$ ) and sensible heat ( $H_{EBM}$ ) was quantified in terms of correlation coefficient ( $r$ ), RMSD (Eq. 3.19), MBE (Eq. 3.20) and MAE (Eq. 3.21) and listed in Table 3.2a,b. Using the aforementioned energy balance model, the calculated latent heat fluxes ( $LE_{EBM}$ ) were compared with the *in situ* LE ( $LE_{EC}$ ) at Selhausen, Merzenhausen, Selhausen-Ruraue, Rollesbroich and Wuestebach, respectively (Table 3.2a). The Rollesbroich and the Wuestebach sites represent the southern part of the catchment with grassland-forest mix and exclusively forest, respectively, representing different land use and topography (also see section 3.2). These two southern sites comparatively exhibit the highest absolute RMSD (118.25, 150.00  $Wm^{-2}$ ), MBE (62.09, 85.95  $Wm^{-2}$ ) and MAE 70.96, 89.89  $Wm^{-2}$ ), despite also showing a high correlation ( $r = 0.92$  and  $0.88$  at Rollesbroich and Wuestebach, respectively). Scatter plots of the calculated  $LE_{EBM}$  and measured  $LE_{EC}$  for the five EC sites (Figure 3.4) exhibit an overestimation in LE calculation for all EC sites with prominently higher estimates at Rollesbroich (predominantly grassland with forest in the surrounding area) and Wuestebach (predominantly forest) as compared to the rest of the sites (predominantly croplands). This overestimation of the calculated LE ( $LE_{EBM}$ ) is also evident in Table 3.2a with higher RMSD, MBE and MAE at Rollesbroich and Wuestebach sites, respectively, as compared to Selhausen, Merzenhausen and Selhausen-Ruraue. The overall overestimation at Rollesbroich and Wuestebach could be due to the difference in landuse of the EC field and the surrounding area covered by the same pixel representing EC station. The pixel representing the EC station at Rollesbroich covers grassland with some surrounding forest and large water bodies which might cause an increase in ET as compared to the EC site. The Wuestebach site is dominantly covered with forests. The Rollesbroich and the Wuestebach sites show less scatter of the individual values (Figure 3.4). This reveals that the surrounding area of the Eddy Covariance station covered by the Land-SAF pixel was more homogeneous than the other three sites.

High LAI at Wuestebach and Rollesbroich could be another possible reason for higher LE at these sites. Density, type, height and morphology of vegetation attenuate the incoming net radiation and thus have an obvious impact on its partitioning into canopy and soil components. Owing to this, my model overestimated latent heat (evapotranspiration) in the southern part of the Rur catchment dominated by forests with higher LAI throughout the year. Along with this overall overestimation at Rollesbroich and Wuestebach, the scatter plots (Figure 3.4) of  $LE_{EC}$  and  $LE_{EBM}$  showed some scatter (partial overestimation) at Selhausen, and Merzenhausen. For

all EC sites, most of the data are above the 1:1 line. Overestimation in the modelled LE ( $LE_{EBM}$ ) might be due to the coarse spatial resolution of the satellite data covering a heterogeneous surface. This overestimation is highly subjected to the degree of surface homogeneity and heterogeneity in land use (especially vegetation cover) of the pixel of satellite data representing Eddy Covariance station which is subjected to seasonal variations in grasses and crops. Prior to seasonal evaluation, a gap-free time-series of the latent heat ( $LE_{REG}$ ) was generated through linear regression fit of  $LE_{EBM}$  and DSSF (Eq. 3.18) (also see section 3.4.2). To further investigate the higher model discrepancies, especially at the Rollesbroich and the Wuestebach sites, the calculated sensible heat fluxes ( $H_{EBM}$ ) were evaluated (Table 3.2b and Figure 3.5).

$H_{EBM}$  exhibits better agreement ( $r > 0.70$ ) with *in situ* sensible heat ( $H_{EC}$ ), as shown in Table 3.2b except at Rollesbroich. Detailed validation statistics between  $H_{EBM}$  and  $H_{EC}$  at Selhausen, Merzenhausen, Selhausen-Ruraue, Rollesbroich and Wuestebach are presented in Table 3.2b. Figure 3.5 represents scatter plots of remotely sensed and *in situ* sensible heat for the EC sites. At the Wuestebach and the Rollesbroich site, the satellite-based estimates underestimate the *in situ* latent heat flux measurement (represented by negative MBE in Table 3.2b), where the forest site (Wuestebach) exhibits more underestimation in  $H_{EBM}$  as compared to the site with grass surrounded by forest (Rollesbroich). Sensible heat at Merzenhausen is also slightly underestimated. Under tall forest trees (high LAI), remote sensors provide data of the top of the canopy only with unsuitable representation of the below canopy area. With the incoming radiation, the top of the canopy gets heated first as compared to the surface(s) below the canopy. Sensible heat was calculated from the temperature gradient (Eq. 3.12 and 3.13) of the canopy ( $T_C$ ), soil ( $T_S$ ) and within the canopy temperatures ( $T_{AC}$ ). Comparatively high elevation sites with higher LAI (Rollesbroich and Wuestebach) may have negative temperature gradients when  $T_S < T_{AC}$ . A negative temperature gradient of  $T_S$  and  $T_{AC}$  (for  $H_s$  calculation) may lead to negative  $H_s$  resulting in an underestimation with respect to *in situ* data. This underestimation (mostly in the form of negative soil component of sensible heat) is reflected as overestimation in latent heat at these two EC sites (Table 3.2a) after applying the energy balance equations (Eq. 3.15 and 3.16). It is evident from those equations that accuracy of the estimated latent heat depends on the accuracy of the sensible heat estimates.

### 3.4.2. Validation of $LE_{REG}$ (Approach 2)

Due to the abovementioned high overestimation for forest regions, and also because of large temporal gaps due to cloudiness, the model output ( $LE_{EBM}$ ) was not suitable to be used directly to calculate annual sums of the latent heat. In order to estimate a complete spatio-temporal latent heat dataset ( $LE_{REG}$ ) for 2011 through 2015, simple linear regression was applied to coinciding hourly  $LE_{EBM}$  and downwelling surface shortwave flux (DSSF) throughout the study period, as discussed earlier (Eq. 3.18). Before establishing the linear regression relationship between satellite-based DSSF and calculated LE ( $LE_{EBM}$ ), the DSSF data were validated by comparing to *in situ* downwelling shortwave radiation measured by EC at hourly timescales (Figure 3.6 and Table 3.3).

Table 3.3. Correlation statistics of hourly *in situ* and remotely sensed Downwelling Shortwave Surface Flux (DSSF) for Eddy Covariance sites in the Rur catchment, Germany, for five years (2011-2015).

| <b>DSSF (<math>Wm^{-2}</math>) 2011-15</b> |                         |                       |             |            |            |
|--|-------------------------|-----------------------|-------------|------------|------------|
| <b>EC Station</b>                          | <b><math>n_v</math></b> | <b><math>r</math></b> | <b>RMSD</b> | <b>MBE</b> | <b>MAE</b> |
| <b>Selhausen</b>                           | 30108                   | 0.95                  | 68.78       | -3.83      | 36.14      |
| <b>Merzenhausen</b>                        | 19674                   | 0.96                  | 58.18       | -4.97      | 31.32      |
| <b>Selhausen-Ruraue</b>                    | No Data                 |                       |             |            |            |
| <b>Rollebroich</b>                         | 37130                   | 0.96                  | 62.51       | -10.94     | 33.43      |
| <b>Wuestebach (2013-12)</b>                | 17881                   | 0.95                  | 57.98       | -2.42      | 29.78      |



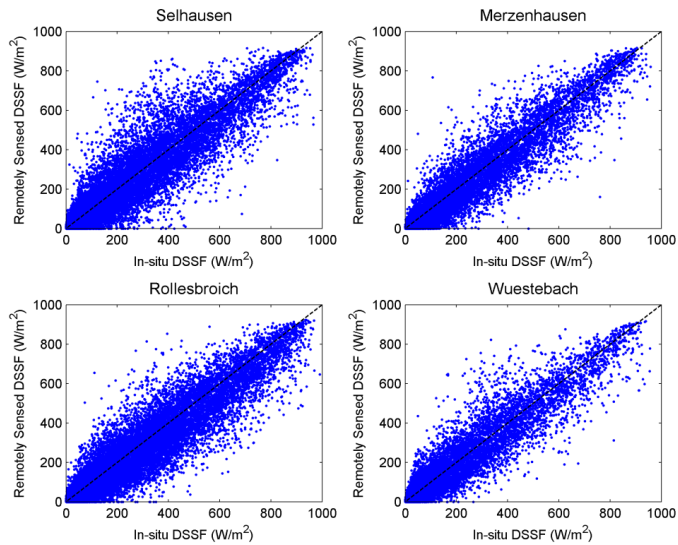


Figure 3.6. Scatter plots of hourly *in situ* and remotely sensed Downwelling Shortwave Surface Flux (DSSF) for Eddy Covariance sites in the Rur catchment, Germany, for five years (2011-2015).

The satellite-derived DSSF corresponds very well to the *in situ* measurements in terms of correlation coefficients ( $r$ ), RMSD, MBE and MAE at Selhausen, Merzenhausen, Rollesbroich and Wuestebach as shown in Table 3.3. The Selhausen-Ruraue site was excluded here due to *in situ* data unavailability. High correlation coefficient values ( $> 0.90$ ) exhibit strong correlation between *in situ* and Land-SAF DSSF on hourly timescale, whereas high RMSD values are due to the higher dynamic range of the incoming shortwave radiation. The scatter plots (Figure 3.6) of *in situ* and Land-SAF DSSF exhibit similar characteristics across EC sites with different elevation. Scatter in the DSSF data (combined for clear and cloudy-sky) in this study may be attributed to cloudy-sky conditions. Trigo et al. (2011) carried out a validation of Land-SAF DSSF for two stations in France separately for clear and cloudy-sky conditions. Their study revealed higher discrepancies for the site with cloudy-sky conditions. Cristobal and Anderson (2013) carried out a detailed regional scale evaluation of the DSSF product of Land-SAF, considering terrain classes (flat and hilly) and atmospheric conditions (clear, cloudy-sky and snow/ice) at hourly, daily and monthly time steps. Here, negative MBE revealed that on average, DSSF data from MSG geostationary platform were slightly underestimated as compared to the *in situ* DSSF during the five years study period. Nevertheless, the overall

accuracy of the satellite-based DSSF was satisfactory. Cristobal and Anderson (2013) also reported a negative MBE of  $-5 \text{ Wm}^{-2}$  and  $-6 \text{ Wm}^{-2}$  for flat and hilly terrain, respectively, between 2008 and 2010 under all sky conditions (clear, cloudy-sky and snow/ice) at hourly timescale. The RMSD calculated by Cristobal and Anderson (2013), for all terrain and atmospheric conditions, are higher than those presented in this study.

After establishing confidence in the satellite-derived DSSF flux, it was used in the regression analysis to derive a gap-free latent heat flux ( $LE_{REG}$ ) dataset. The regression equation ( $LE_{REG} = 0.43 \times DSSF$ ) was used for estimating latent heat from DSSF where the slope value 0.43 represents the mean regression slope between  $LE_{EBM}$  and DSSF from agricultural sites (Selhausen, Selhausen-Ruraue and Merzenhausen), where the model exhibits better results than the Rollesbroich and Wuestebach sites. The validation statistics in Table 3.2a revealed an overestimation in LE retrieval at the Rollesbroich and Wuestebach sites. These overestimations are also evident in Figure 3.7, where higher slope values are shown for comparatively higher LAI regions, i.e., Rollesbroich (grass and forest cover mix) and Wuestebach (forest cover) in the Eifel region. Therefore, instead of pixel-wise regression or catchment-scale mean regression slope, the mean slope value calculated for agricultural sites was applied equally to the whole catchment for deriving latent heat ( $LE_{REG}$ ) from DSSF (Table 3.4).

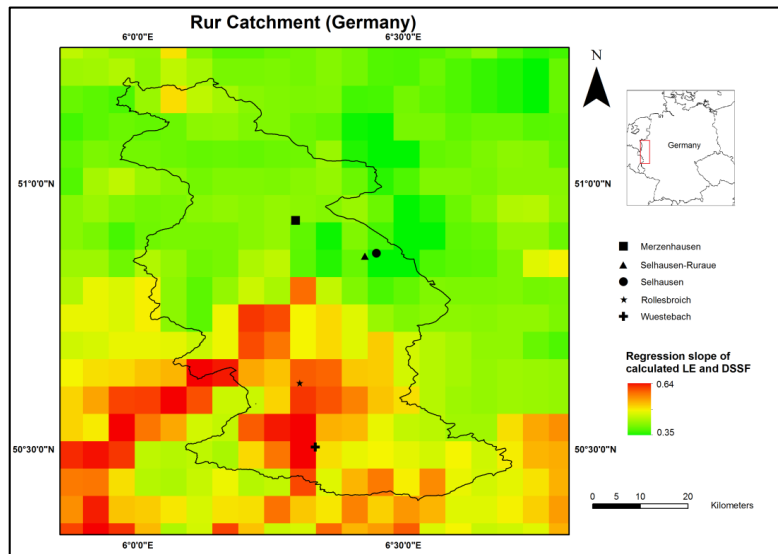


Figure 3.7. Regression slope of  $LE_{EBM}$  and DSSF (pixel-wise) for the whole study period from 2011 through 2015 for the Rur catchment.

Regression analysis was kept independent of *in situ* LE ( $LE_{EC}$ ) and the *in situ* measurements were only used to perform independent validation of the estimated  $LE_{REG}$ . Correlation statistics (correlation coefficient, RMSD, MBE and MAE) of  $LE_{REG}$  with  $LE_{EC}$  for the period 2011-2015 are given in Table 3.4. It is evident from Table 3.4 that  $LE_{REG}$  leads to a strong increase in the number of available hourly data points for validation ( $n_v$ ), correlation coefficients show only minor variations (as compared to Table 3.2a), but values representing absolute validation accuracy (RMSD, MBE and MAE) show a clear improvement (Table 3.4). The correlation coefficients in Table 3.4 are more or less similar to those given in Table 3.2a for  $LE_{EBM}$ . RMSD, MBE and MAE are significantly reduced for the Rollesbroich and Wuestebach sites (Table 3.2a vs Table 3.4). Some improvement in RMSD, MBE and MAE can also be observed for Selhausen, Merzenhausen and Selhausen-Ruraue. Figure 3.8 shows scatter plots of  $LE_{REG}$  with  $LE_{EC}$  at the five Eddy Covariance sites in the study area.

Table 3.4. Correlation statistics on hourly *in situ* latent heat flux ( $LE_{EC}$ ) and remotely sensed latent heat ( $LE_{REG}$ ) for the Eddy Covariance sites in the Rur catchment, Germany, for five years (2011-2015).

| <b><math>LE_{REG}</math> and <math>LE_{EC}</math> (<math>Wm^{-2}</math>) 2011-15</b> |                         |                       |             |            |            |
|--|-------------------------|-----------------------|-------------|------------|------------|
| <b>EC Stations</b>   | <b><math>n_v</math></b> | <b><math>r</math></b> | <b>RMSD</b> | <b>MBE</b> | <b>MAE</b> |
| <b>Selhausen</b>   | 23902                   | 0.83                  | 51.15       | -0.74      | 31.96      |
| <b>Merzenhausen</b>  | 28915                   | 0.78                  | 56.28       | 9.03       | 33.15      |
| <b>Selhausen-Ruraue</b>  | 21432                   | 0.86                  | 47.46       | -2.99      | 30.17      |
| <b>Rollesbroich</b>  | 26562                   | 0.89                  | 43.24       | 7.58       | 26.72      |
| <b>Wuestebach (2013-15)</b>  | 11736                   | 0.83                  | 61.29       | 25.94      | 34.67      |

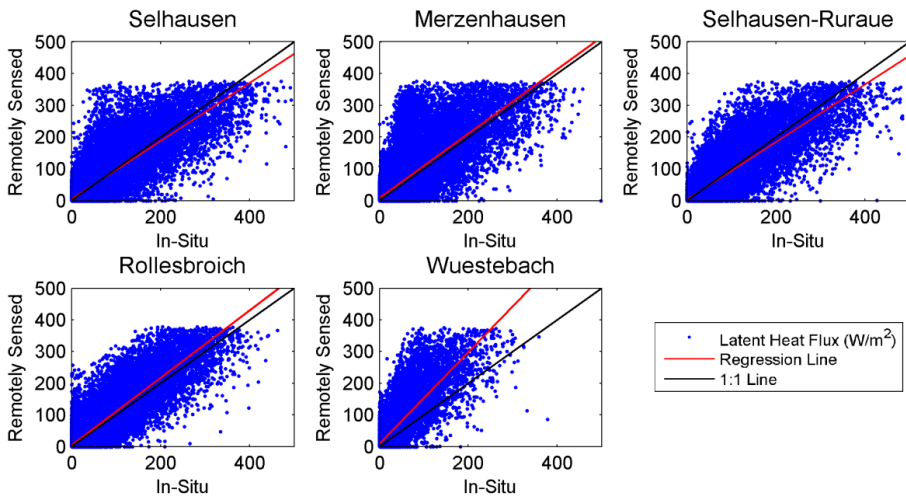


Figure 3.8. Scatter plots of hourly  $LE_{EC}$  (*in situ*) and  $LE_{REG}$  (through regression analysis from downwelling surface shortwave flux) for Eddy Covariance sites in the Rur catchment, Germany, for the years 2011-2015.

The scatter plots of  $LE_{REG}$  with  $LE_{EC}$  (Figure 3.8) show similar discrepancies in the modelled latent heat at Selhausen and Merzenhausen, and less overall overestimation of  $LE_{REG}$  at Wuestebach, while  $LE_{REG}$  at the Rollesbroich site shows no overall overestimation (Figure 3.4 vs Figure 3.8). Although  $LE_{REG}$  leads to comparatively better validation results especially at Rollesbroich and Wuestebach (Table 3.2a vs Table 3.4 and Figure 3.4 vs Figure 3.8), model discrepancies in  $LE_{REG}$  were further evaluated through seasonal investigation (i.e., on monthly basis). These could be the effect of seasonal surface heterogeneity, especially at sites with crops inside the EC field and surrounding. To verify the effect of seasonality, a further seasonal comparison of the *in situ* and modelled LE was performed. For this purpose  $LE_{REG}$  and  $LE_{EC}$  were split into monthly datasets for the year 2012. With the monthly assessment it was found that during June-July the EC footprint represents the surrounding area very well (being homogeneously vegetated), hence  $LE_{EC}$  are close to  $LE_{REG}$ . The opposite is true at Merzenhausen and Selhausen (dominantly croplands) with the advent of winter wheat harvest season during August-September 2012, when the local EC footprint was not representing the area covered by the surrounding satellite data pixel. The winter wheat in the area (including the EC field) gets senescent in July and is harvested between mid-July and mid-August. The EC fluxes thus represent senescent wheat and bare soil conditions with little or no transpiration. Sugar beet, maize, grassland and forest fields in the same pixel, in contrast, continue to transpire and co-determine the  $LE_{REG}$  estimates.

To further investigate this discrepancy, the  $LE_{EC}$  and  $LE_{REG}$  for June and mid-August to mid-September during 2012 were compared with the help of a scatter plot (Figure 3.9). A good agreement exists between *in situ* and remotely sensed LE during June 2012, where a scale difference between EC footprint of several hundreds of meters and remote sensing pixel of ~ 5 km is of no consequence due to homogeneous crop conditions. There is more deviation from the 1:1 line during mid-August to mid-September due to less homogeneous crop conditions surrounding the EC field. At this point in time, winter wheat was already harvested in the EC field (on 30<sup>th</sup> July 2012) and only evaporation from soil contributed to EC measurements. A temporal sequence (Figure 3.10) of  $LE_{EC}$  and  $LE_{REG}$ , for the same time slot, can better visualize the temporal comparison of *in situ* and remotely sensed estimates of LE. June is representing a homogeneous surface as compared to the period from mid-August to mid-September. Figure 3.10 (upper) shows improved adjustment between  $LE_{EC}$  and  $LE_{REG}$  in June. Higher estimates of the  $LE_{REG}$  as compared to  $LE_{EC}$  in figure 3.10 (lower) are due the coarse pixels of the satellite

data, which represents other vegetation surrounding the EC footprint. During this period winter wheat was already harvested and  $LE_{EC}$  is only representing the soil evaporation. Increase in  $LE_{EC}$  (Figure 3.10 lower) is due to rainfall events on the relevant days. This effect is similar for the apparent overestimation at Selhausen in early spring, when sugar beet was newly sown and most of the surface acts as bare soil. Footprint-based LE measuring methods (e.g. Eddy Covariance) do not represent the surrounding heterogeneous surface (Wang *et al.*, 2007). Therefore in this study, Eddy Covariance based *in situ* latent heat data ( $LE_{EC}$ ) were only used to validate the remotely sensed latent heat ( $LE_{EBM}$  and  $LE_{REG}$ ). It was not used in the linear regression due to its lack of representation of the surrounding area, covered by a single LandSAF pixel, might have resulted in a biased latent heat output ( $LE_{REG}$ ). The final latent heat flux ( $LE_{REG}$ ) was integrated to an annual sum and converted to equivalent evapotranspiration units of  $\text{mmyear}^{-1}$  (Figure 3.11). Figure 3.11 demonstrates the trend of evapotranspiration throughout the study period from 2011 through 2015. The southern part of the Rur catchment on the bedrock of the Eifel Mountains with higher elevation, low air temperature and higher rainfall rate exhibits comparatively low evapotranspiration compared to the northern part of the catchment [Figure 3.11 and 3.12, Table 3.5 (also see section 3.2)]. According to my results, 2011 was the year with highest sum of ET [641, 645, 644, 626, 616 ( $\text{mmyear}^{-1}$ ) at Selhausen, Merzenhausen, Selhausen-Ruraue, Rollesbroich and Wuestebach, respectively (Table 3.5)]. According to the report of the European Drought Observatory, EDO (EDO-2011a; EDO-2011b), western, central and northern European countries (including extended areas of France, Germany, Great Britain, Denmark, Belgium, the Netherlands, Luxembourg and Hungary) had received less than 50% of the expected rain since December 2010 until May 2011, coupled with higher temperature and low cloudiness, enhanced the rate of evapotranspiration and vegetation water requirement. The period from January to May during the year 2011 was the driest period since 1975 by then with a rainfall deficit in most parts of the Europe (EDO-2011b). According to a report of the World Meteorological Organization (WMO, (WMO-2011)), a long-lasting dry spell was observed over extended parts of Europe (including Germany) from January through May during 2011. Data from the Global Precipitation Climatology Centre (GPCC, (GPCC-2011)) revealed a significant rain deficit period over extended areas of Europe which was observed, particularly, during the months from February to April 2011. In 2011, the southeastern parts of the United Kingdom had a driest March since 1953, whereas Switzerland experienced the whole year (2011) as one of the driest 10 year periods since 1864, accompanied with low water levels in rivers, lakes and groundwater, particularly in the areas of Jura and

Central Plateau (Hydrological yearbook of Switzerland 2011). According to the German Federal Hydrological Agency (BfG (BfG-2011)), rivers in Germany experienced very low levels, which also affected shipping in the Rhine River. Rudolph et al. (2015) pointed out paleo-river structures at Selhausen during May 2011 on RapidEye multispectral image. This study did not find these paleo-river structures in the study area before or after May 2011 while evaluating a time-series of LAI during 2011-2012 (see chapter 2). Hypothetically, these paleo-river structures are important for subsoil hydrology only under (temporarily) dry conditions. According to my results, 2012 is marked with the lowest ET rate at all the test sites during the study period, with an ET rate of 594, 593, 597, 580 and 560 ( $\text{mmyear}^{-1}$ ) at Selhausen, Merzenhausen, Selhausen-Ruraue, Rollesbroich and Wuestebach, respectively (Table 3.5). 2012 and 2013 exhibit comparatively wet conditions in the study area. The annual sum ( $\text{mmyear}^{-1}$ ) tends to increase again towards 2015 (Figure 3.12 and Table 3.5). Also during 2015, EDO reported drought conditions in Europe due to a prolonged rainfall deficit since April with temperature anomalies coupled with higher evapotranspiration towards July (EDO-2015). However, the Land-SAF data were only available until November, 11, 2015, therefore, 2015 ET map represents a period from January, 1 to November, 11 during 2015.

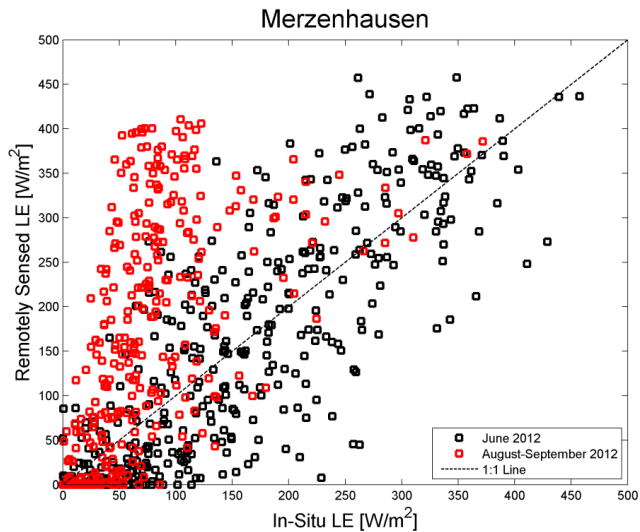


Figure 3.9. Scatter plot of hourly  $LE_{REG}$  and  $LE_{EC}$  for June and mid-August to mid-September during 2012 at Merzenhausen.

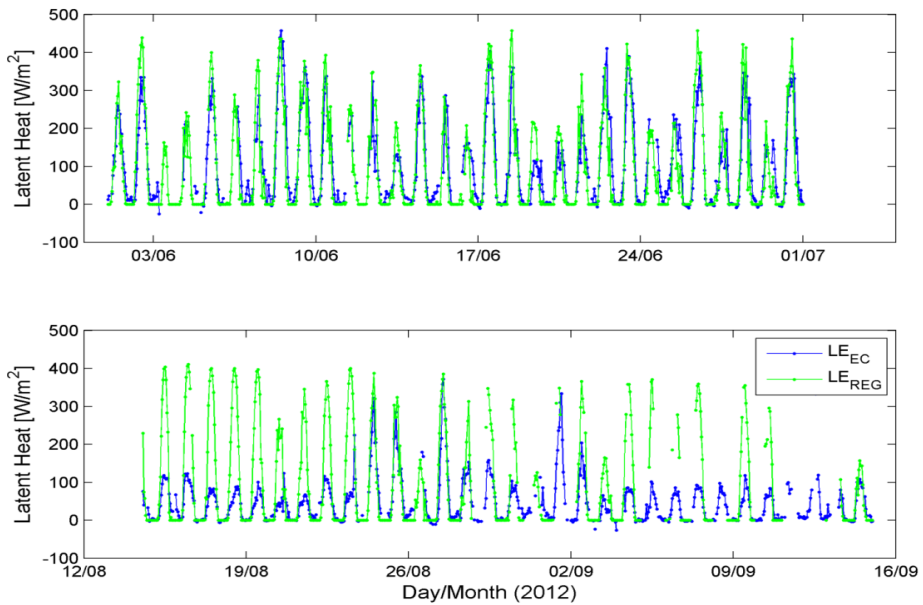


Figure 3.10. Temporal sequence of  $LE_{REG}$  and  $LE_{EC}$  during June 2012 (upper) and mid-August to mid-September 2012 (lower) at Merzenhausen.



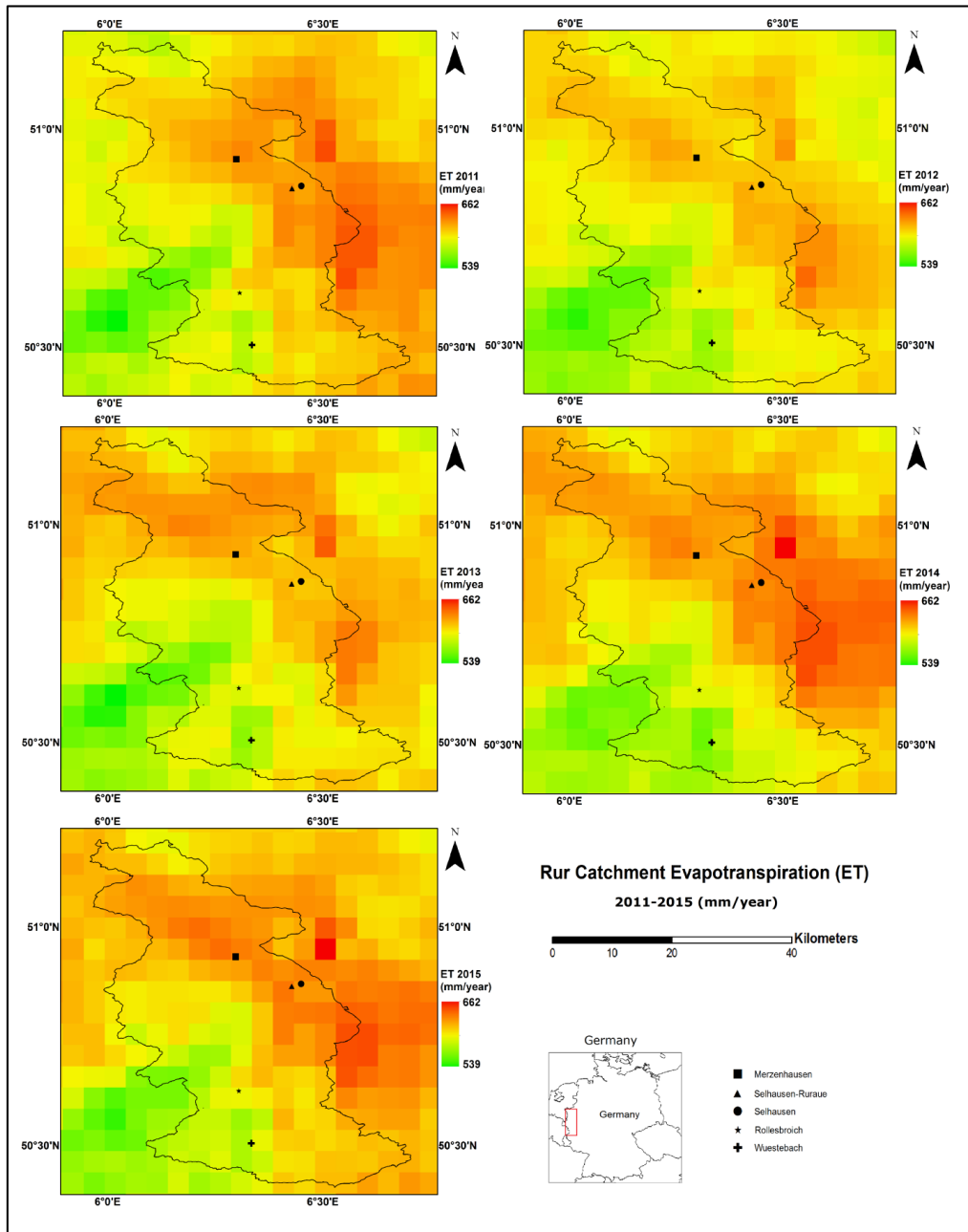


Figure 3.11. Annual evapotranspiration ( $\text{mm year}^{-1}$ ) in the Rur catchment (2011-2015).

Table 3.5. Annual evapotranspiration ( $\text{mm year}^{-1}$ ) for Eddy Covariance sites in the Rur catchment, Germany, for the years 2011-2015.

| Evapotranspiration ( $\text{mm year}^{-1}$ ) |      |      |      |      |      |
|--|------|------|------|------|------|
| EC Site                                      | 2011 | 2012 | 2013 | 2014 | 2015 |
| Selhausen                                    | 641  | 594  | 608  | 629  | 625  |
| Merzenhausen                                 | 645  | 593  | 613  | 628  | 628  |
| Selhausen-Ruraue                             | 644  | 597  | 611  | 632  | 630  |
| Rollesbroich                                 | 626  | 580  | 594  | 604  | 610  |
| Wuestebach                                   | 616  | 560  | 580  | 582  | 601  |

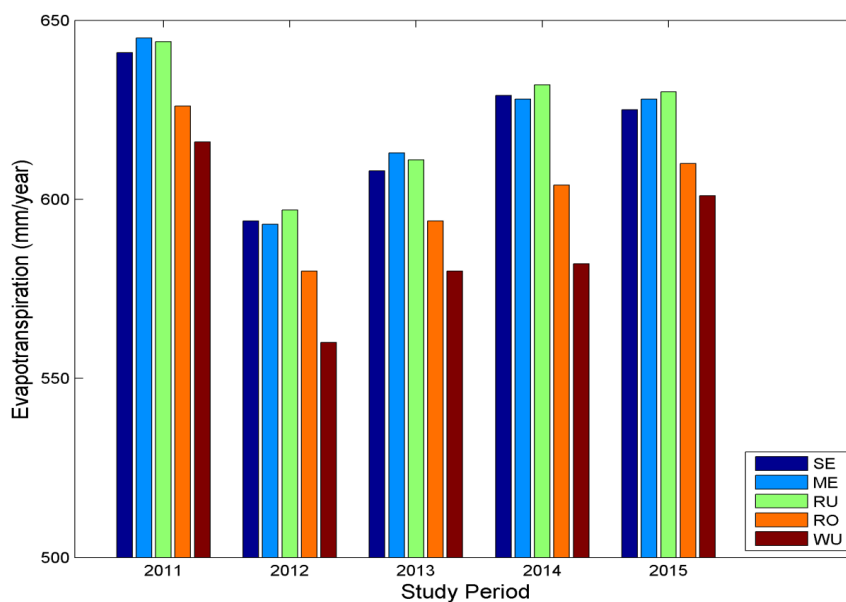


Figure 3.12. Annual sum of evapotranspiration ( $\text{mm year}^{-1}$ ) for Eddy Covariance sites, namely, Selhausen (SE), Merzenhausen (ME), Selhausen-Ruraue (RU), Rollesbroich (RO) and Wuestebach (WU) for a period of 2011 through 2015, in the Rur catchment, Germany.

### 3.5. Conclusions

In this study, geostationary satellite-based operational energy fluxes and vegetation information were evaluated using an empirical simplification of an energy balance approach for a period of five years (2011-2015) to obtain continuous LE time-series. Validation results from this study have shown that, using remotely sensed energy fluxes (coarse spatial resolution of 5x5 km but high temporal resolution of 30 minutes), temporally consistent estimates of latent heat could be generated to derive evapotranspiration (Figure 3.11). The model worked well in crop areas, with different crop types having different plantation, senescent and harvest periods, leading to increased sub-pixel surface heterogeneity. However, uncertainty increases in areas with higher LAI (Eifel National Park) with less sub-pixel surface heterogeneity. LE estimates are purely remotely sensed and reference latent heat ( $LE_{EC}$ ) data were only used to perform validation. Validation statistics (on hourly LE estimates) at five Eddy Covariance sites in the Rur catchment (covering croplands, grassland and forests) are generally satisfactory. Agreement between reference LE and  $LE_{EBM}$  (Table 3.2a) and  $LE_{REG}$  (Table 3.4) was similar with reasonable reduction in model discrepancies (i.e., RMSD, MBE and MAE) for the latter. Furthermore,  $LE_{REG}$  data have more hourly data points for validation and can be used to derive annual sums of latent heat. Using the regression based LE retrieval approach, gap-free time-series of latent heat with subsequent evapotranspiration can be generated in an operational manner even in areas with no meteorological data availability.

I hypothesize that surface heterogeneity within the respective pixel of the remote sensing image referring to each EC site was the major source of higher RMSD, MBE and MAE when modelled LE was compared to *in situ* LE. My model exhibited good agreement between remotely sensed and *in situ* hourly latent heat during June, when the area covered by the pixel representing EC site was homogeneously covered by green vegetation. Earlier and later in the vegetation period, the sowing and harvesting dates of different crop types can lead to strong LE contrasts between inactive (bare or senescent) and green fields, with the EC station representing only the type present on its field, while the pixel LE is a weighted average of both. Main sources of uncertainty in the calculated LE are related to this surface heterogeneity within the same pixel. Overestimated latent heat was observed at Rollesbroich and Wuestebach and exhibited very high RMSD, MBE and MAE as compared to the rest of the test sites. However, this overestimation was reduced for  $LE_{REG}$ . The Wuestebach and the Rollesbroich sites are characterized by comparatively higher elevation, higher LAI (forest) and slightly lower surface

and air temperature as compared to Selhausen, Merzenhausen and Selhausen-Ruraue. Higher LAI, more cloudy conditions and a different temperature gradient within the canopy may have led to the overestimation in latent heat, especially in  $LE_{EBM}$ , in the southern Rur catchment. Nevertheless, the southern part of the catchment is characterized by a comparatively lower annual ET sum than the northern part. Validation of coarse resolution latent heat with footprint-scale *in situ* latent heat has been always challenging due to the scale mismatch. To bridge the gap between *in situ* and large scale remotely sensed fluxes, Norman et al. (2003) designed the disALEXI approach to disaggregate ALEXI fluxes from continental-scale to field-scale. Vegetation information (LAI) calculated at high spatial resolution will reduce the difference between  $LE_{EC}$  and  $LE_{EMB}/LE_{REG}$ , as high resolution LAI captures surface heterogeneity more precisely (see chapter 2).

This study reveals 2011 as the year with the highest ET rate in the study period, followed by the lowest rate in 2012 and a gradual increase in annual ET sum toward 2015. This temporal variability in annual ET sum can be linked with rain deficit conditions coupled with low cloudiness and higher than normal temperature in Europe as reported by the European Drought Observatory (EDO) especially during 2011 and 2015 (EDO-2011a; EDO-2011b; EDO-2015). The approach may be applied to another geographical area (with different set of meteorological and environmental conditions) in order to evaluate the robustness of the method beyond the study area. Alternatively, application on an even longer time-series may be suitable to evaluate the method for various years with different rainfall occurrence. It will help test the method on comparatively dry and wet conditions in the same area under investigation. Application of the method on high spatial resolution remote sensing data would produce more accurate and reliable estimates of ET and will reduce scale gap to reference observations for validation. Energy fluxes and vegetation information on high spatial resolution will further reduce model discrepancies by reducing the surrounding pixel area around Eddy Covariance point on relevant remote sensing data.

## **4. Towards a Solely Remotely-Sensed Water Balance for the Rur Catchment, Germany<sup>3</sup>**

### **4.1. Introduction**

Spatial and Temporal variability and distribution of water are crucial for weather and climatic systems and its variable patterns over the earth surface from local to regional scale. There are several factors that control/affect the spatio-temporal distribution of water and its movement on the earth surface and between soil and atmosphere. Temperature is an important variable among other factors that have profound impacts on the water cycle components (Sala *et al.*, 2015). During the past decades, increase in the global temperature was observed with uncertainty about the future increase (Huntington, 2006). Climate models also revealed major changes to the climate in future i.e., precipitation patterns, temperature anomalies, hot extreme and heat waves coupled with less frequent cold extremes (Kundzewicz, 2008; Kundzewicz *et al.*, 2009). Changes in climate affect the hydrological cycle (water cycle) and vice versa (Kundzewicz, 2008). Climate change would affect the hydrological cycle and the balance of water between soil-vegetation and atmosphere (Oki and Kanae, 2006; Shelton, 2009) leading to hydrologic extremes in the form of floods (heavy rains) and extreme droughts (Kundzewicz, 2008). Better planning and management strategies are needed for water resources being vital for various human activities from domestic to agricultural and industrial use. Furthermore, better water management strategies and practices are also critical to mitigate antagonistic effects of hydrological extremes. Shortage of water may be directly linked to food production (Allen and Bastiaanssen, 2005). Hydrological processes like precipitation, evapotranspiration (ET), infiltration, subsurface flow, interception and runoff (Kundzewicz, 2008) are the main components of the water cycle and its spatio-temporal distribution and variation affect terrestrial water balance. Water balance approach is commonly used in hydrology for accounting the flow of water in and out of a system. Water balance is the separation of water added to a system (as precipitation) into major components i.e., evapotranspiration, runoff and storage as terrestrial water. Changes in terrestrial water storage may be neglected when water balance is applied on a longer temporal scale (Milly, 1994; Babin, 1995; Montzka *et al.*, 2008b). For catchment-scale water balance applications, operational and reliable estimates of rain,

---

<sup>3</sup> Adapted from: Ali, M., Montzka, C., Jadoon, K. Z., Diederich, M., Diekkrueger, B., Vereecken, H., (in preparation), Towards a Solely Remotely Sensed Water Balance for the Rur Catchment, Germany.

evapotranspiration and runoff with respect to space and time are crucial. Land cover types and materials, the degree of imperviousness both in urban and rural areas (Shuster *et al.*, 2005; Montzka *et al.*, 2008b; O'Driscoll *et al.*, 2010) and inadequate measurement of water balance components may lead to uncertainties in the water balance.

Precipitation is the primary water input source to a hydrological domain and its precise spatio-temporal estimates are very crucial for land surface hydrology (Uijlenhoet, 2001; Kundzewicz, 2008). Ground-based radar systems are capable of quantifying rainfall with respect to space and time (Uijlenhoet, 2001). Also, satellite-based techniques for rainfall estimations e.g., TRMM (Tropical Rainfall Measuring Mission), GPM (Global Precipitation Mission) and MPE (Multi-sensor Precipitation Estimate) etc. are becoming useful for areas with no ground-based radar coverage and *in situ* information. After precipitation, evapotranspiration is the second largest component of the terrestrial water balance. Spatio-temporal variability in ET is very important for the hydrological cycle and weather system of an area and may be closely linked to changing climate and land use (Thompson *et al.* (2011). Evapotranspiration depends on incoming solar radiation and its partitioning into various components, i.e., latent heat (LE), sensible heat (H) and ground heat flux (G). This partitioning depends on various factors including land use, density and type of vegetation, type of climate, geographical location, topography, air temperature, time of the day and day of the year etc. (see chapter 3). Latent heat flux (LE) is responsible to transform liquid water into vapour. Energy balance is applied at the earth surface whereby latent heat is measured as residual of the energy balance (see chapter 3). Latent heat is converted to equivalent evapotranspiration (ET) units ( $\text{mmyear}^{-1}$ ) from energy units ( $\text{Wm}^{-2}$ ) using  $28.4 \text{ Wm}^{-2} = 1 \text{ mmday}^{-1}$  (Allen *et al.*, 1998; Allen *et al.*, 2005).

Runoff is referred as the component of the hydrological cycle that flows downstream instead of being evaporated or absorbed by the soil through infiltration to add soil moisture and replenish groundwater. Built-up parts in a catchment reduce infiltration rate and hence increase the rate of surface runoff. Topography may also affect the rate of infiltration and runoff, however, the slope-infiltration relationship is not very clear (Fox *et al.*, 1997; Ribolzi *et al.*, 2011). Runoff estimates with respect to space and time are crucial for managing water resource in an area for better allocation of water for various uses including agricultural, industrial and domestic use (Parajka *et al.*, 2013; Viglione *et al.*, 2013). Runoff/discharge characteristics are essential variables for hydrological extremes predictions especially drought (McKee *et al.*, 1993) and flooding (Rogger *et al.*, 2012) conditions in an area. The response of runoff, the balance

between precipitation and evapotranspiration may help to better plan hydrological risk management, e.g. to evaluate the effect of hydrological extremes (floods and droughts).

Numerous hydrological models are employed to simulate hydrological processes at all scales (Devi *et al.*, 2015), whereby calibration with *in situ* hydrological properties is an integral part (Pechlivanidis *et al.*, 2011). Due to inconsistency of the *in situ* measurements, extrapolations of the available measurements are applied in space and time in the modelling procedures (Pechlivanidis *et al.*, 2011). Various model parameters do not have physical interpretation and the hydrological simulations may become conceptual rather than physical (Wagner *et al.*, 2003). In this study, the catchment-scale water balance solely based on remotely sensed data to predict runoff provides useful information regarding the runoff patterns in the study area. This approach may be used in ungauged or poorly gauged basins for better water balance analysis. According to Parajka *et al.* (2013) runoff prediction in ungauged catchments is comparatively more accurate for catchments with humid conditions than arid conditions. In case of no or limited *in situ* data, runoff prediction solely based on remotely sense data is of utmost importance towards practical applications for operational decision making, utilization, planning and management of water resources especially in areas more vulnerable to water scarcity or inundation.

This study is aimed to retrieve runoff solely from remotely sensed data for various sub-catchments in the Rur catchment. Here, catchment and sub-catchments-scale runoff/discharge (Q) is quantified by incorporating satellite-based remotely sensed ET (calculated in this study) and radar-based precipitation, in order to assess the catchment-scale annual status and trend of water resource during 2011 through 2014. For this purpose, annual rates and four year annual means of evapotranspiration (ET) and precipitation (P) are balanced at various sub-catchments in the Rur catchment to estimate annual runoff from 2011 through 2014, where net terrestrial water storage is kept negligible. To quantify runoff, accuracy of rainfall and evapotranspiration especially from remote sensors (ground- and satellite-based) have profound impact on the accuracy of runoff. The estimated runoff is compared to *in situ* runoff. Furthermore, the effects of wet and dry conditions in the study area during the study period are also evaluated through annual hydrographs on sub-catchment scale.

## 4.2. Materials and Methods

### 4.2.1. Hydro-geological Description of the Study Area

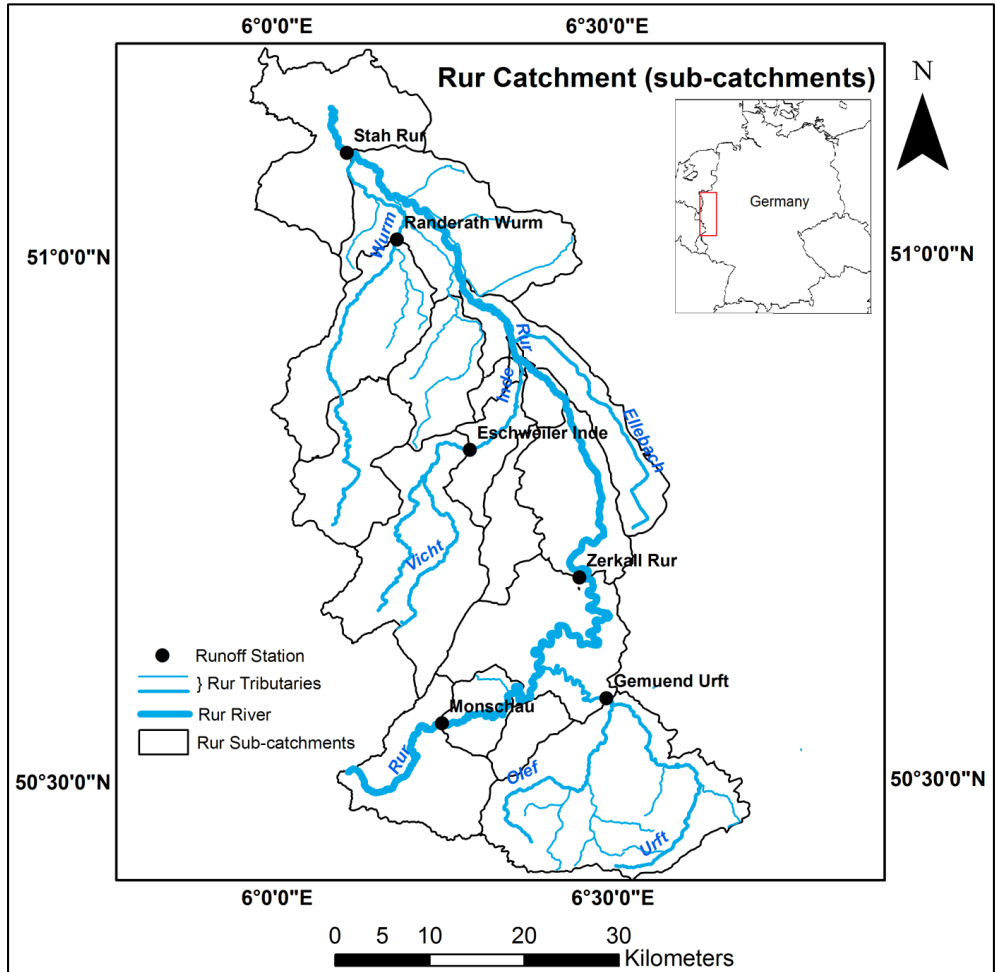


Figure 4.1. Sub-catchments in the Rur catchment with Rur River and its main tributaries along with runoff measuring gauge locations.

The Rur catchment is equipped with state-of-the-art hydrological and meteorological observatories at various test sites (TERENO; Bogena *et al.*, 2005a; Bogena *et al.*, 2005b; Bogena *et al.*, 2005c; Bogena *et al.*, 2006). The catchment can be divided into distinctive southern and northern parts. Located on the bedrock of the Eifel Mountains, the southern part



has a higher long-term annual precipitation of 850–1300  $\text{mmyear}^{-1}$  and a moderate annual potential evapotranspiration of 450–550  $\text{mmyear}^{-1}$ . Due to Devonian and Carboniferous sedimentary rocks, the region is characterized by low permeability (low infiltration rates) and small groundwater storage volumes mostly exhibit direct runoff towards streams and reservoirs (Bogena *et al.*, 2005a; Bogena *et al.*, 2005c; Montzka *et al.*, 2008a; Montzka *et al.*, 2008b). Owing to different geological and topographical setting and high precipitation with comparatively low temperatures and evapotranspiration, the southern Rur catchment experiences higher runoff rate (Montzka *et al.*, 2008b). This part is largely covered by forest and grassland. The northern part is predominantly arable land with fertile soil and characterized by a relatively low annual precipitation (650–850  $\text{mmyear}^{-1}$ ) and a high potential evapotranspiration of 580–600  $\text{mmyear}^{-1}$ . This region has more groundwater recharge potential owing to the underlying loose rock aquifers (Bogena *et al.*, 2005c) and experiences low surface runoff (Montzka *et al.*, 2008b). The Rur catchment is mainly drained by the Rur River (165 km long) that originates in the southwest of the catchment in Rhenish Massif with maximum altitude of 720 m and annual rainfall of 1200 mm (Bogena *et al.*, 2005c). The Rur River has many small and large tributaries including Urft, Olef, Vicht, Inde and Wurm (Figure 1), whereas the Rur itself is a sub-catchment of the River Maas (Meuse) with annual average rainfall of 700 mm. The study area is marked with various small and large sub-catchments and more than half of the catchment is covered by consolidated rocks (Bogena *et al.*, 2005b). Owing to the coarse resolution of the satellite data, only larger sub-catchments (Bogena *et al.*, 2005a) [namely, Stah-Rur (area 2135.15  $\text{km}^2$ ), Randerath-Wurm (area 310.52  $\text{km}^2$ ), Eschweiler-Inde (area 232.15  $\text{km}^2$ ), Zerkall-Rur (area 787  $\text{km}^2$ ), Gemuend-Urft (area 344.55  $\text{km}^2$ ) and Monschau-Rur (area 143.63  $\text{km}^2$ )] were selected for water balance analysis in this study (Figure 1). *In situ* runoff measuring stations are located at the outlet of each sub-catchment (Figure 1). The Stah runoff station serves as the outlet for the whole Rur catchment incorporating all sub-catchments with area slightly smaller than the whole downstream area (2354  $\text{km}^2$ ) of the Rur catchment. Likewise, Zerkall-Rur incorporates Monschau-Rur and Gemuend-Urft. The annual average runoff and flow at the gauging Stah is 348mm and 22.8 $\text{m}^3\text{s}^{-1}$ , respectively (Bogena *et al.*, 2005a).

#### **4.2.2. Remotely Sensed Precipitation Estimates**

Radars are important active remote sensors (both ground-based and satellite-based), which emit electromagnetic radiation at microwave frequencies and sense back the reflected echoes. Radars became essential tool to estimate type, direction and intensity of precipitation. These abilities

of radar technology make it a first choice of operational data acquisition tool for meteorologists, hydrologists and researchers in other relevant fields (Fabry, 2015). Ground-based radar reflectivity data i.e. RADOLAN (Radar Online Adjustment) of German weather Service (DWD) were mainly used to estimate rainfall patterns for the study area. Using radar for precipitation estimates, radar reflectivity factor  $z$  ( $\text{mm}^6\text{m}^{-3}$ ) is converted to rain rate ( $R$ ) using  $z$ - $R$  relationship between reflectance and rainfall (Eq. 4.1) (Bianchi *et al.*, 2013; Fabry, 2015):

$$z = 200R^{1.6} \quad (4.1)$$

Due to the large range (from 0.001 to 36000000  $\text{mm}^6\text{m}^{-3}$  for fog and large size hail, respectively) of the radar reflectivity factor ( $z$ ), it is expressed in decibel of reflectivity (dBZ) where dBZ is 10 times the log of  $z$  (Eq. 4.2):

$$dBZ = 10 \log z \quad (4.2)$$

Equation 4.1 is modified as Equation 4.3 for converting dBZ to rain rate ( $\text{mmh}^{-1}$ ):

$$R [\text{mmh}^{-1}] = \left( \frac{10^{dBZ/10}}{200} \right)^{1/1.6} \quad (4.3)$$

This conversion is very crucial for the application of radar-based surface hydrological estimates and lead to under-or-overestimation of the rain rate. The strength of echoes received at the radar receiver are affected by several factors, for instance, distance from radar, earth curvature, beam angle, topography (elevation and surface roughness), and non-precipitation targets like smoke/ash, aeroplanes, large fires, birds' flocks and ground clutter. Furthermore, due to the lower melting layer, the winter months are more problematic and surface rain estimates are comparatively more contaminated. The region of the atmosphere where snow and rain coexist as snow is falling aloft and melt before reaching the ground is known as melting layer or snow region (Matrosov *et al.*, 2007; Diederich *et al.*, 2015a). Much more improved melting layer correction methods are needed for calculating more accurate rain rate during cold months (Diederich *et al.*, 2015b, a). Extreme care is needed to filter-out unwanted echoes by non-precipitation targets. Here, systematic discrepancies in radar rain estimates were minimized through Inverse Distance Weighting (IDW) based interpolated bias calculated between RADOLAN rain rate and *in situ* rain at various location in the Rur catchment. Annual sums

( $\text{mm year}^{-1}$ ) of rain were calculated on RADOLAN data for various large sub-catchments in the Rur catchment, Germany.

The available satellite-based remote sensing precipitation data was not utilized in this study. The TRMM mission (with spatial covering of  $50^{\circ}\text{N}$ - $50^{\circ}\text{S}$ ) had commenced in 1997, and came to an end in April 2015 after providing operational tropical rainfall estimates for hydrological, meteorological and weather related studies (NASA-TRMM; Derin and Yilmaz, 2014). The study area is laying outside the TRMM spatial coverage. GPM data was not incorporated due to unavailability during major part of the study period (NASA-GPM). MPE is more appropriate for the spatial distribution and strength of the convective rainfall estimates only (Heinemann *et al.*, 2002; Derin and Yilmaz, 2014).

#### 4.2.3. Remotely-sensed ET estimates

Annual sums of evapotranspiration were derived from the time-series of latent heat ( $LE_{\text{REG}}$ ) calculated through a simplified regression relationship (Eq. 3.18) established between calculated latent heat ( $LE_{\text{EBM}}$ ) and downwelling surface shortwave flux from the SEVIRI onboard the Meteosat second generation geostationary satellites (see chapter 3). Latent heat retrieval from satellite platform is highly affected by the presence of clouds causing gaps in hourly  $LE_{\text{EBM}}$  making it unsuitable for calculating annual sums. DSSF under cloudy conditions are estimated based on cloud transmittance, cloud albedo and atmospheric transmittance between surface and clouds (as discussed in detail in chapter 3 section 3.3.2).

#### 4.2.4. Water Balance

The water balance represents the hydrologic cycle in a linear way with rainfall as main input while total runoff ( $Q_T$ ) and ET are the main output (Eq. 4.4):

$$P = ET + Q_T \pm \Delta S \quad (\text{where } \Delta S = 0 \text{ for } \text{mm/year}) \quad (4.4)$$

One assumption in this study is that net change in terrestrial water storage ( $\Delta S$ ) is negligible on annual scale. The water balance separates incoming precipitation into major catchment losses, i.e., evapotranspiration and total runoff. Evapotranspiration (ET) is comprised of transpiration from vegetation and evaporation from bare soil and water bodies. Total runoff ( $Q_T$ ) is comprised of surface runoff and groundwater flow or infiltration whereof surface runoff is the flow of

water into streams, while infiltration is the downward flow of water as soil moisture and further deep as groundwater recharge with strong link to the river system. Soil moisture greatly affect the distribution of total runoff into surface runoff and infiltration (Moradkhani, 2008).

The infiltrated water is evaporated from the bare soil or transpired through vegetation goes back to the atmosphere or percolate further to groundwater. The groundwater is usually pumped-out for drinking purpose and other uses, while the rest is eventually exfiltrated to surface water as baseflow (Ponce and Shetty, 1995). According to L'vovich (1979), deep percolation is very small and generally can be neglected. Therefore, in a water balance approach applied on a longer temporal scale, terrestrial water storage can be neglected (Milly, 1994; Babin, 1995; Montzka *et al.*, 2008b) on practical grounds and Eq. 4.4 is adopted to assess sub-catchment and catchment-scale river/stream discharge/runoff (Q). In this study, I balance remotely sensed ET (also see chapter 3) and RADOLAN-based rainfall data to predict runoff from sub-catchment to catchment scale in the Rur catchment. The predicted runoff is then compared to runoff measured at various observatories located at the outlet of each sub-catchment (Figure 4.1).

### **4.3. Results and Discussions**

#### **4.3.1. Annual Runoff**

In this study, the annual status and trend of water in-flow and out-flow (on sub-catchment to catchment scale) in the Rur catchment was evaluated by analyzing temporal trends in precipitation, ET and total runoff on annual basis and for the mean of three years. Runoff was predicted for various sub-catchments in the study area (Figure 4.1) using equation 4.4 whereby remotely sensed ground radar-based reflectivity were converted to rain rate ( $\text{mmh}^{-1}$ ) and satellite-based latent heat ( $\text{LE}_{\text{REG}}$ ) was converted to equivalent evapotranspiration units ( $\text{mmh}^{-1}$  and  $\text{mmyear}^{-1}$ ). Thus the water balance was applied solely on remotely sensed variables to quantify runoff. Predicted runoff data were then compared to *in situ* runoff measured at the outlet of each sub-catchment, namely Stah, Zerkall, Gemuend, Randerath, Eschweiler and Monschau as shown in figure 4.1. *In situ* runoff for the year 2011 was excluded due to unavailability. The Stah sub-catchment, with an area  $\sim 2153.15 \text{ km}^2$ , includes all other catchments as sub-catchments. Sub-catchment-wise detailed comparison of yearly precipitation, evapotranspiration, predicted runoff and *in situ* runoff during 2011 through 2014 is shown in Table 4.1a,b and Figure 4.2.

Table 4.1a. Annual rate of radar-based rainfall, satellite-based ET, predicted and *in situ* runoff for various sub-catchments in the Rur catchment, Germany, during 2011-2012.

| Sub-Catchments<br>(Area in km <sup>2</sup> ) | 2011 (mmyear <sup>-1</sup> ) |        |                        |                     | 2012 (mmyear <sup>-1</sup> ) |        |                        |                     |
|--|------------------------------|--------|------------------------|---------------------|------------------------------|--------|------------------------|---------------------|
|  | P                            | ET     | Q <sub>Predicted</sub> | Q <sub>Insitu</sub> | P                            | ET     | Q <sub>Predicted</sub> | Q <sub>Insitu</sub> |
| <b>Stah</b><br>(2135.15)                     | 722.94                       | 631.64 | 91.30                  | no<br>data          | 869.48                       | 583.47 | 286.00                 | 242.01              |
| <b>Zerkall</b><br>(787)                      | 801.46                       | 630.00 | 171.46                 | no<br>data          | 990.61                       | 578.94 | 411.67                 | 423.29              |
| <b>Gemuend</b><br>(344.55)                   | 727.87                       | 632.77 | 95.09                  | no<br>data          | 920.34                       | 581.65 | 338.69                 | 342.53              |
| <b>Randerath</b><br>(310.52)                 | 608.32                       | 629.54 | -21.22                 | no<br>data          | 783.73                       | 585.68 | 198.06                 | 296.10              |
| <b>Eschweiler</b><br>(232.15)                | 736.28                       | 614.88 | 121.40                 | no<br>data          | 923.35                       | 567.94 | 355.41                 | 330.77              |
| <b>Monschau</b><br>(143.63)                  | 967.04                       | 622.42 | 344.62                 | no<br>data          | 1201.40                      | 567.36 | 634.05                 | 790.95              |

Table 4.1b. Annual rate of radar-based rainfall, satellite-based ET, predicted and *in situ* runoff for various sub-catchments in the Rur catchment, Germany, during 2013-2014.

| Sub-catchments    | 2013 (mmyear <sup>-1</sup> ) |        |                        |                      | 2014 (mmyear <sup>-1</sup> ) |        |                        |                      |
|-------------------|------------------------------|--------|------------------------|----------------------|------------------------------|--------|------------------------|----------------------|
|                   | P                            | ET     | Q <sub>Predicted</sub> | Q <sub>In situ</sub> | P                            | ET     | Q <sub>Predicted</sub> | Q <sub>In situ</sub> |
| <b>Stah</b>       | 748.39                       | 601.18 | 147.22                 | 359.94               | 878.54                       | 613.01 | 265.54                 | 237.03               |
| <b>Zerkall</b>    | 842.41                       | 597.98 | 244.42                 | 480.58               | 881.76                       | 603.81 | 277.95                 | 400.52               |
| <b>Gemuend</b>    | 793.42                       | 600.59 | 192.83                 | 360.82               | 821.73                       | 606.06 | 215.67                 | 312.58               |
| <b>Randerath</b>  | 683.35                       | 602.11 | 81.24                  | 302.25               | 896.07                       | 615.22 | 280.86                 | 306.02               |
| <b>Eschweiler</b> | 789.19                       | 583.16 | 206.03                 | 333.77               | 936.89                       | 598.96 | 337.93                 | 290.05               |
| <b>Monschau</b>   | 1014.80                      | 594.41 | 420.38                 | 647.70               | 1032.80                      | 591.46 | 441.37                 | 573.61               |

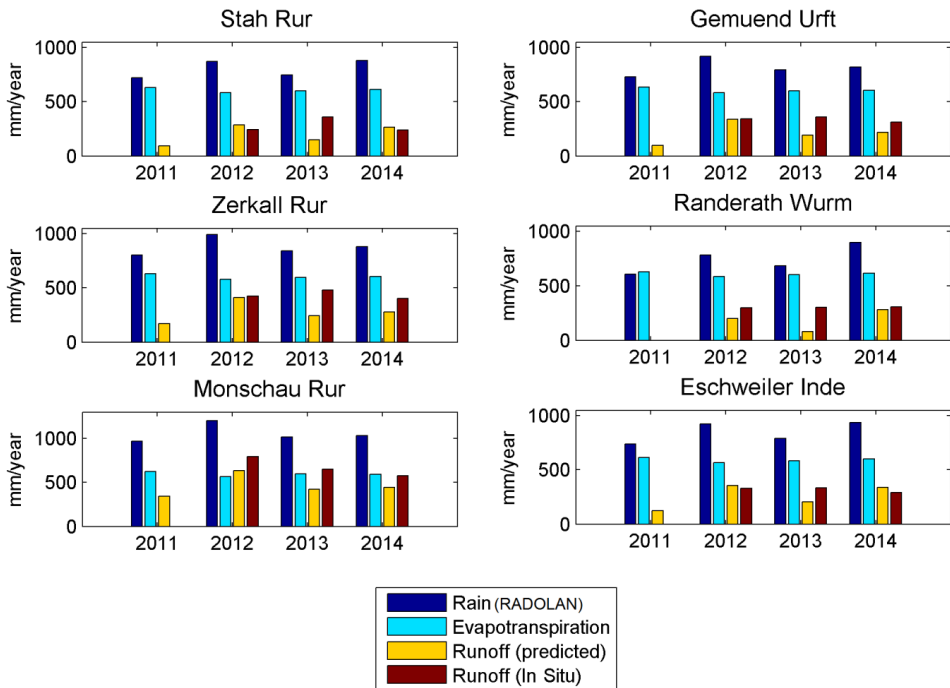


Figure 4.2. Comparison of the annual remotely sensed radar-based rain rate (RADOLAN), satellite-based ET, predicted and *in situ* runoff for various sub-catchments in the Rur catchment for the year 2011 through 2014.

During 2012 and 2014, better comparison was observed between *in situ* and predictive runoff with less difference between *in situ* and predictive runoff. This comparison is different in 2013 and comparatively large difference was observed between *in situ* and predictive runoff throughout the Rur catchment. Lowest runoff was observed at the outlet of all sub-catchments in the study area during 2011 which was also declared as the driest year over major parts of Europe, including the study area, by the European Drought Observatory, EDO (EDO-2011a; EDO-2011b). Annual sum of rainfall from RADOLAN data utilized in this study also revealed lowest rainfall in 2011 as compared to the rest of the study period (Table 4.1a,b). ET and rainfall estimates in this study show highest rainfall and lowest evapotranspiration in 2012 during the study period and hence comparatively higher runoff was predicted (Table 4.1a). RADOLAN rain data revealed again less rainfall during 2013 in the Rur catchment as compared to 2012 and 2014 (Table 4.1a,b), but still more than rainfall during 2011. Larger difference between *in situ* and predictive runoff due to higher *in situ* runoff during 2013 may be attributed to the subsurface flow (also called through flow) of the rainfall events during 2012. To further evaluate the temporal discharge patterns and difference of *in situ* and predicted rainfall in the Rur catchment, hydrographs were plotted on annual *in situ* and predicted runoff for all sub-catchments in the Rur catchment (Figure 4.3). The hydrographs show more or less similar runoff patterns during 2012 and 2014 with respect to *in situ* and predicted runoff. The year 2013 exhibits different runoff pattern between *in situ* and predicted runoff throughout the Rur catchment. The Monschau sub-catchment is located in the region of less permeable rocks with forests and higher rainfall, therefore, overland flow dominates subsurface flow and the runoff rate is higher than in other sub-catchments. The Monschau sub-catchment exhibits higher runoff in 2012 with decreasing trend towards 2014, whereas, the rest of the catchments exhibit higher *in situ* runoff during 2013. Therefore, comparison between *in situ* and predictive runoff on longer temporal scale will minimize the effect of late subsurface flow in the catchment.

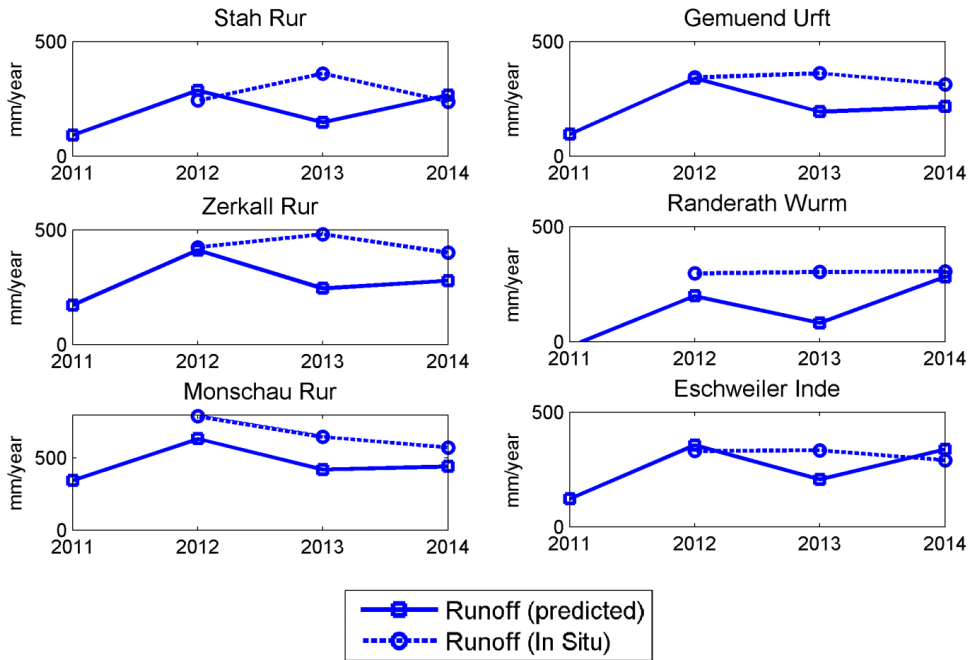


Figure 4.3. Hydrograph of annual *in situ* and estimated runoff for various sub-catchments in the Rur catchment for the years 2011-2014.

#### 4.3.2. Mean Annual Runoff

The rate of infiltration and subsequent subsurface flow (baseflow) may affect annual runoff estimates solely from remotely sensed rainfall and evapotranspiration as net change in terrestrial water storage was kept negligible. Applications of this approach on short temporal scale may produce better results for rainfall events with more intensity as more intense rain may affect (minimize) the rate of infiltration i.e., decrease in recharge coefficient (Huang *et al.*, 2013), such that a major part of rainfall becomes overland or surface flow. Also, this approach may be effective for large urbanized surfaces where imperviousness reduces the rate of infiltration (Montzka *et al.*, 2008b). The infiltration capacity of the soil depends on soil properties e.g., hydraulic conductivity, porosity, and pore distribution (Baker, 1979; Haghazari *et al.*, 2015). Vegetation increases permeability and water storage capacity of the soil (Huang *et al.*, 2013). A longer temporal scale may be used for obtaining better model results. Therefore, three years mean annual precipitation, evapotranspiration, predicted runoff and *in situ* runoff during 2012



through 2014 were also evaluated and the comparison have been presented in Table 4.2 and figure 4.4. Compared to the annual runoff rates, difference of *in situ* and predicted runoff is reduced for three years mean annual runoff rates, as evident from Table 4.2 and figure 4.4.

Table 4.2. Mean annual rate of radar-based rainfall, satellite-based ET, predicted and *in situ* runoff for various sub-catchments in the Rur catchment, Germany, during 2012 through 2014.

| Sub-catchments    | 2012-2014 (Mean Annual in $\text{mmyear}^{-1}$ ) |        |                        |                     |
|-------------------|--|--------|------------------------|---------------------|
|                   | P  | ET     | Q <sub>Predicted</sub> | Q <sub>Insitu</sub> |
| <b>Stah</b>       | 832.14   | 599.22 | 232.92                 | 279.66              |
| <b>Zerkall</b>    | 904.92   | 593.58 | 311.35                 | 434.79              |
| <b>Gemuend</b>    | 845.17   | 596.10 | 249.07                 | 338.64              |
| <b>Randerath</b>  | 787.72   | 601.00 | 186.72                 | 301.46              |
| <b>Eschweiler</b> | 883.14   | 583.35 | 299.79                 | 318.20              |
| <b>Monschau</b>   | 1083.00  | 584.41 | 498.60                 | 670.75              |

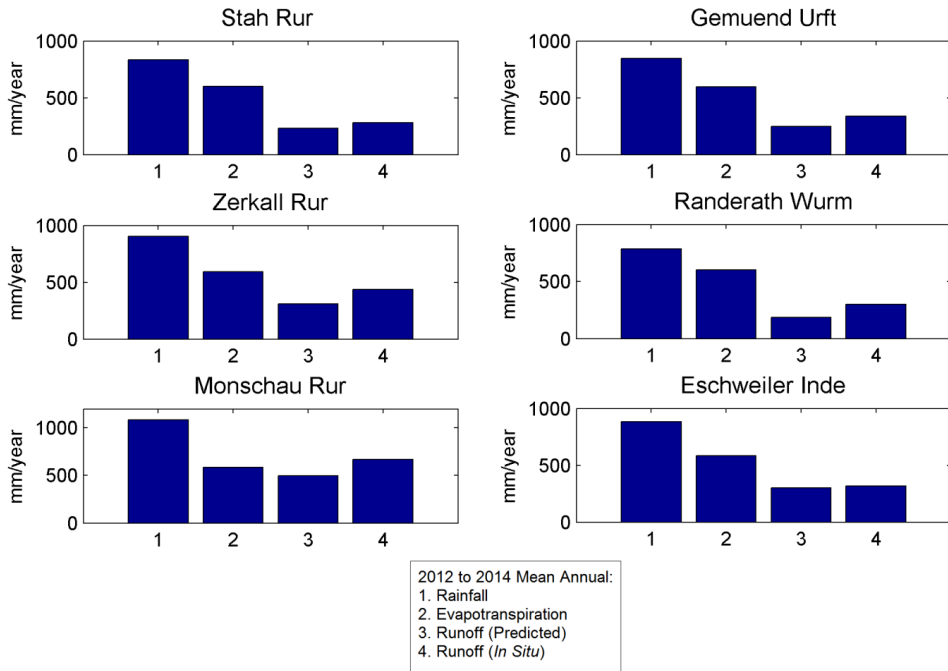


Figure 4.4. Mean annual remotely sensed radar-based rain rate (RADOLAN), satellite-based ET, predicted and *in situ* runoff for various sub-catchments in the Rur catchment for the year 2012 through 2014.

The scatter plot in figure 4.5 demonstrates the correlation result of this approach for various sub-catchments in the Rur catchment based on three year mean (i.e., 2012 through 2014). The predicted runoff correlates very well to the *in situ* runoff with correlation coefficient,  $r = 0.95$ , the root mean squared difference,  $\text{RMSD} = 106.92 \text{ mmyear}^{-1}$ , and mean bias error,  $\text{MBE} = -94.18 \text{ mmyear}^{-1}$ . The predicted runoff with this approach exhibits underestimation which may be attributed partly to overestimation in ET. The Eschweiler gauge presents best model result i.e., close to 1:1 line, followed by the Stah gauge, however, considering area of the sub-catchments (Table 4.1a), the Stah and the Zerkall may be ranked best than any other sub-catchment. The Randerath, Gemuend and Zerkall can be ranked similar with respect to predicted runoff following the same distance from 1:1 line (Figure 4.5). The Monschau and Gemuend sub-catchments are located towards south in the Eifel region with comparatively higher rate of annual rainfall and lower rate of evapotranspiration at Monschau, whereas, Gemuend receive comparatively less rainfall (Tables 4.1a,b and 4.2, Figures 4.2 and 4.4). The Monschau sub-catchment is the smallest sub-catchment in the Rur catchment evaluated here,

but due to higher rainfall and lower ET rate, it exhibits higher annual and mean annual runoff throughout the study period. The mean annual rate of *in situ* and predicted runoff (279.66 and 232.92 mm, respectively) observed at the Stah gauge is less than the average annual runoff (348 mm) reported by Bogena et al. (2005a). Overall, the mean annual predicted runoff is underestimated as compared to the *in situ* runoff data for all sub-catchments. This underestimation may partially be attributed to the overestimation of remotely sensed evapotranspiration (also see chapter 3 section 4.2). Increasing the temporal scale from annual to three years mean annual rate, predicted runoff demonstrated comparatively better correlation to *in situ* runoff data. Less biased evapotranspiration from remote sensors and application on even longer time scale may further improve the estimation of runoff solely from remotely sensed data.

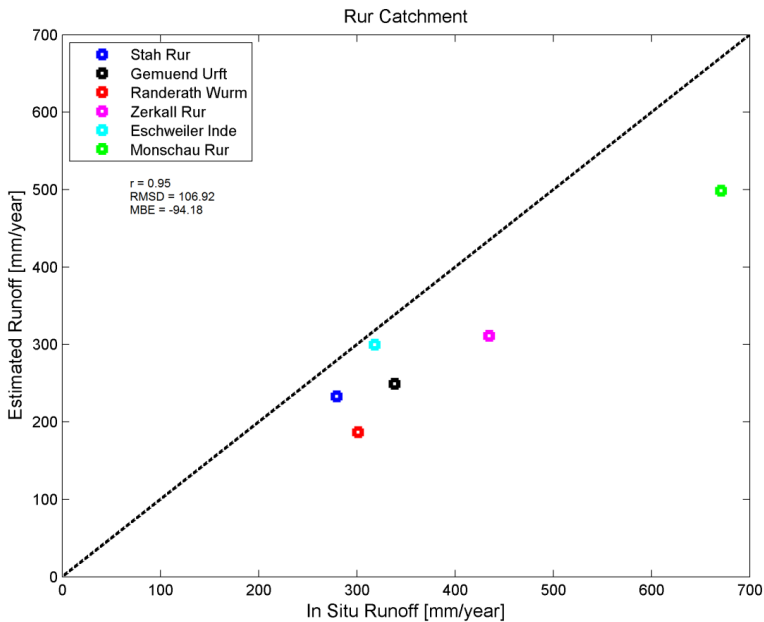


Figure 4.5. Scatter plot of mean annual *in situ* and predicted runoff for various sub-catchments in the Rur catchment for the years 2012-2014.

#### 4.4. Conclusion and Outlook

This study evaluates the utilization of solely remotely sensed data to build water balance on a catchment scale. With radar-based rainfall (RADOLAN) and satellite-based evapotranspiration, annual (2011-2014) and mean (2012-2014) runoff data were calculated for various sub-catchments in the Rur catchment, Germany. The derived spatial and temporal runoff patterns were analyzed in comparison to *in situ* runoff patterns on annual and mean annual temporal scales. Variations in runoff patterns with respect to space and time may be used as a clue for understanding the water balance of an area and provide an appropriate guide towards agriculture and water related planning and practices especially to overcome events of hydrological extremes. During 2012-2014, as the observed mean annual runoff, both estimated and *in situ*, at the outlet of the Rur catchment at the Stah gauge was lower than the mean annual runoff equal to 348 mm reported in literature (Bogena *et al.*, 2005a). Thus, it can also be linked with local to regional scale climatic changes and weather anomalies reported by the European Drought Observatory during the past several years (Kundzewicz *et al.*, 2009) and also during the study period (EDO-2011a; EDO-2011b; EDO-2015). Apart from weather and meteorological impacts, further analysis of land use and land cover (LULC) changes may better explain the varying trend of runoff in the catchment.

During the study period, the year 2011 was a drier period with less annual rainfall and comparatively higher evapotranspiration in the Rur catchment. Also lowest runoff was estimated throughout the catchment during 2011. Considering the alternate dry and wet periods in the catchment and current climate change scenario, consistent and operational analysis of the hydrological estimates must be carried out before and after the study period selected in this study. The robustness of the water balance analysis solely on remote sensing data must be examined in different geographical areas with a different set of weather and climatic conditions before extension to ungauged or poorly gauged basins. This approach exclusively applied to remotely sensed data would better manage water related issues especially in basins with water scarcity conditions and ungauged basins. More precise and accurate spatio-temporal estimates of rainfall and evapotranspiration from remote sensors mounted on satellite platforms would make the approach more widely applicable throughout the globe, especially in remote areas and regions with no or less *in situ* networks.

Here, changes in the terrestrial water storage were kept constant and hence the water balance was applied on annual rainfall and evapotranspiration, however, better results were observed

for 3-years mean data (i.e., 2012 through 2014). It is concluded here that the current approach is more appropriate on larger temporal scales, for instance, larger than annual scale. Applications on larger temporal scale may lead to improved estimates of sub-catchment to catchment scale runoff.

## 5. Synthesis

### 5.1. Final conclusion

This thesis investigated direct retrieval methods of a vegetation bio-physical variable (i.e., LAI) and hydrological fluxes (i.e., rainfall, evapotranspiration and runoff) from remotely sensed data. Remote sensing methods employ sophisticated and state-of-the-art sensors/instrument to capture spatial information on regional scale in operational manner. Consistent availability of the relevant variables and state variables from remote sensing platforms is the foremost choice of data acquisition for spatio-temporal surface hydrological estimates. Approaches developed in this thesis for remotely sensed vegetation characteristics and hydrological parameters estimates were exclusively validated in the Rur catchment in the west of Germany near the border area of Netherlands-Belgium-Germany. The Rur catchment has well-equipped test sites (e.g., TERENO test sites) with *in situ* networks for measuring various hydrological and energy fluxes within the soil-vegetation-atmosphere continuum. The catchment is also covered by radar-based rain (RADOLAN) estimation (Diederich *et al.*, 2015b). Throughout this thesis, it was tried to solely utilize remote sensing data and reduce dependency on the *in situ* measurements except for validation of remotely sensed vegetation bio-physical and hydrological estimates. Being site specific, *in situ* measurements have limited scope towards spatial extrapolation and hence cannot be applied on regional scale. Nevertheless, being most accurate and precise, *in situ* measurements are widely used for calibration and validation of remote sensing estimates. Sometimes, *in situ* information has been used in semi-empirical approaches for parameter calibration and cannot be excluded from the main algorithms to compute several required variables and state variables and also the required final output.

#### 5.1.1. Estimation and validation of LAI

Various spectral vegetation indices (VI) calculated on satellite images contain important information easily compatible in various models used for retrieving soil moisture, evapotranspiration, plants growth, agriculture productivity and weather related estimates. The effects of changing atmospheric conditions on the time-series of RapidEye level 3A imagery were evaluated through the application of relative (IR-MAD) and absolute (ATCOR) atmospheric corrections. This study reports that relative and absolute atmospheric corrections are not necessary for LAI retrieval. Vegetation indices used for LAI retrieval are already normalized (i.e., difference of two spectral bands (red and NIR) is normalized by the sum of

the same spectral bands). It was concluded that correction applied on the producer level were enough for the level 3A RapidEye product for LAI retrieval. However, these corrections may be further tested under different climatic and illumination conditions in a different geographical location. LAI estimated incorporating newly available satellite-based red-edge band presented best correlation with *in situ* measurements for winter wheat. The red-edge band proved as a best substitute for the red spectral channel in NDVI and SAVI for estimating LAI and should be applied in future studies utilizing Sentinel-2 data. The light extinction coefficient  $k(\theta)$  showed sensitivity towards the RMSD between  $LAI_{\text{rapideye}}$  and  $LAI_{\text{destr.}}$ . The most appropriate  $k(\theta)$  selection depends upon VI, vegetation type, leaf angle, leaves distribution, density of vegetation, light penetration into the canopy and latitudinal location on the earth surface.

### 5.1.2. Evapotranspiration

Estimation and validation of latent heat calculated through the energy balance model ( $LE_{\text{EBM}}$ ) and regression analysis ( $LE_{\text{REG}}$ ) are presented here.  $LE_{\text{REG}}$  exhibits better correlation statistics as compared to  $LE_{\text{EBM}}$ .  $LE_{\text{EBM}}$  presented suitable validation results for areas with crops in the northern Rur catchment and exhibited overestimation in the forested southern Rur catchment. In general, throughout the catchment higher model discrepancies are linked to the coarse spatial resolution (5km x 5Km) and its comparison to footprint scale Eddy Covariance data. Temporally the discrepancies are higher when the pixel representing EC station is not homogeneous with respect to vegetation. Within a pixel, the surface homogeneity is decreased when the EC station is surrounded by senescent vegetation close to harvest season or barren soil when vegetation is already harvested. Furthermore, another reason for the within pixel reduced homogeneity is the difference in planting and harvest time of various crops in the study area. Utilization of finer spatial resolution satellite imagery will increase surface homogeneity surrounding the EC station.

Downwelling Surface Shortwave Flux (DSSF) was used as the main controlling factor for ET and was used in pixel-wise regression with  $LE_{\text{EBM}}$  (Figure 3.7). For final  $LE_{\text{REG}}$  estimation, suitable regression slope was selected from the agricultural sites in Selhausen. The regression analysis was proved to be a better direct ET retrieval method to create a gap-free consistent latent heat (evapotranspiration) from remote sensing data by relating longer time-series of ET (with gaps) to a basic ET controlling/depending factor.  $LE_{\text{REG}}$  leads to a strong increase in the number of available hourly data points for validation with minor variation in correlation coefficient and slight reduction in RMSD for Selhausen, Merzenhausen and Selhausen-Ruraue.

The root mean square difference (RMSD), mean bias error (MBE) and mean absolute error (MAE) are significantly reduced for Rollesbroich and Wuestebach sites owing to the utilization of best suitable regression slope from agricultural fields for  $LE_{REG}$  estimation. This study reveals higher annual ET rate during 2011 with lowest annual rate in 2012 and again increasing trend in ET annual rate towards 2015. The higher ET rate during 2011 can be linked to regional perspective of increased temperature and shortage in rainfall reported by the European Drought Observatory (EDO-2011a; EDO-2011b).

### 5.1.3. Water Balance

The aim of this chapter was to develop water balance solely on remotely sensed evapotranspiration and rainfall to estimate annual and mean annual runoff at sub-catchment to catchment scale. For rainfall estimates, ground-based radar rainfall data (RADOLAN) from DWD was incorporated instead of using satellite-based precipitation e.g., MPE (best for convective rain only), GPM (unavailable) and TRMM (spatially outside the study area). Throughout the study period 2011 is marked as the driest year with less rainfall and more evapotranspiration coupled with higher temperature. In 2011, lowest runoff was observed at the outlet of all sub-catchments in the study area as compared to the rest of the study period. The year was also marked as the driest year by the European Drought Observatory EDO (<http://edo.jrc.ec.europa.eu/edov2/php/index.php?id=1051>). The year 2012 records maximum rainfall and lowest evapotranspiration estimates and hence higher runoff estimates.

Estimated runoff is comparable to the *in situ* runoff throughout the study area. Especially, the mean annual estimated runoff showed high correlation ( $r = 0.95$ ) to *in situ* runoff. Overall, the mean annual estimated runoff is underestimated when compared to *in situ* runoff data. Application on even longer time scale may improve the estimation of runoff solely from remotely sensed data by reducing root mean squared difference and mean absolute error. The mean annual *in situ* and estimated runoff for the Rur catchment observed in this study is less than the average runoff reported in literature (Bogena *et al.*, 2005a). Impacts of climate and land use/land cover changes induced uncertainties to hydrological processes may further be evaluated in connection with the spatio-temporal runoff patterns observed recently.



## 5.2. Outlook

This thesis investigated estimation and validation of LAI, evapotranspiration, rainfall and runoff based on remote sensing techniques in the Rur catchment, Germany, may lead to better direct retrieval methods for continental and global scale applications. Estimated time-series of LAI was validated on winter wheat and further studies must be carried out to evaluate the robustness of the method on other vegetation and in other geographical areas with different set of climatic, illumination and soil conditions. The red-edge spectral band can further be tested for other crops, grasses (Asam *et al.*, 2013) and forests (Schumacher *et al.*, 2016) in the study area and beyond. Additionally, further analysis of the light extinction coefficient for heterogeneous surfaces with different vegetation types, incorporating different spectral vegetation indices, different illumination conditions and for different sensors acquiring multispectral imagery may lead to more appropriate and suitable light extinction coefficient selection for diverse spatial scale LAI mapping based on remote sensing data.

Estimated latent heat derived on coarse pixel size lead to higher uncertainty under heterogeneous surface vegetation conditions when compared to Eddy Covariance measurements. This uncertainty can be reduced by using finer resolution remotely sensed energy fluxes and vegetation information. So far, no single satellite system provides data with fine spatial and temporal resolutions simultaneously. Next Meteosat mission, the Meteosat Third Generation (MTG) of EUMETSAT and ESA, with infrared and ultraviolet/visible sounding missions will provide crucial data for land surface processes. The satellite-based consistent monitoring with fine resolution spatial and temporal information are needed for more accurate and precise assessment of evapotranspiration and its impacts on the hydrology, weather, agricultural practices, irrigation and other relevant phenomena and processes. The energy balance approach with subsequent regression approach must be applied to an even longer period incorporating dry and wet years in the same study area or under similar climatic conditions. Also, the robustness of the model used must be analyzed in another geographical location under different set of weather and climatic conditions. Keeping in view the episodes of high and low annual rates in the catchment, further investigation through incoming years needed to better understand the annual trend in evapotranspiration rate in the catchment and beyond.

The satellite-based precipitation estimates are increasingly used for hydrological applications, however, its accuracy is still inappropriate for several quantitative hydrological estimates and

## Synthesis

catchment scale water balance studies. This thesis demonstrated utilization of ground-based radar rainfall estimates to quantify annual runoff patterns. Prediction of runoff based on remotely sensed data with more precise rainfall estimates from satellite platform (i.e., applications of the water balance purely on remotely sensed data) could lead to better and operational water related planning and management especially for ungauged or poorly gauged basins. It will timely and operationally help to ward off or mitigate the adversities from severe rains and extreme droughts.

**Bibliography**

- Abdou, W.A., Pilorz, S.H., Helmlinger, M.C., Conel, J.E., Diner, D.J., Bruegge, C.J., Martonchik, J.V., Gatebe, C.K., King, M.D., Hobbs, P.V., 2006. Sua Pan surface bidirectional reflectance: A case study to evaluate the effect of atmospheric correction on the surface products of the Multi-angle Imaging SpectroRadiometer (MISR) during SAFARI 2000. *IEEE Trans. Geosci. Remote Sensing* 44, 1699-1706.
- Aires, F., Prigent, C., Rossow, W.B., Rothstein, M., 2001. A new neural network approach including first guess for retrieval of atmospheric water vapor, cloud liquid water path, surface temperature, and emissivities over land from satellite microwave observations. *J. Geophys. Res.-Atmos.* 106, 14887-14907.
- Alavi, N., Warland, J.S., Berg, A.A., 2006. Filling gaps in evapotranspiration measurements for water budget studies: Evaluation of a Kalman filtering approach. *Agric. For. Meteorol.* 141, 57-66.
- Allen, R.G., Bastiaanssen, W.G.M., 2005. Special issue on remote sensing of crop evapotranspiration for large regions. *Irrigation and Drainage Systems* 19(3), 207-210.
- Allen, R.G., Pereira, L.S., Raes, D., Smith, M., 1998. Crop evapotranspiration: guide-lines for computing crop water requirements. In: *FAO Irrigation and Drainage Paper No. 56*. FAO, Rome, Italy.
- Allen, R.G., Pereira, L.S., Smith, M., Raes, D., Wright, J.L., 2005. FAO-56 dual crop coefficient method for estimating evaporation from soil and application extensions. *J. Irrig. Drainage Eng-ASCE* 131, 2-13.
- Allen, R.G., Tasumi, M., Trezza, R., 2007. Satellite-based energy balance for mapping evapotranspiration with internalized calibration (METRIC) - Model. *J. Irrig. Drainage Eng-ASCE* 133, 380-394.
- Anderson, M.C., Kustas, W.P., Norman, J.M., Hain, C.R., Mecikalski, J.R., Schultz, L., Gonzalez-Dugo, M.P., Cammalleri, C., d'Urso, G., Pimstein, A., Gao, F., 2011. Mapping daily evapotranspiration at field to continental scales using geostationary and polar orbiting satellite imagery. *Hydrol. Earth Syst. Sci.* 15, 223-239.
- Anderson, M.C., Norman, J.M., Diak, G.R., Kustas, W.P., Mecikalski, J.R., 1997. A two-source time-integrated model for estimating surface fluxes using thermal infrared remote sensing. *Remote Sens. Environ.* 60, 195-216.

## Bibliography

- Anderson, M.C., Norman, J.M., Mecikalski, J.R., Otkin, J.A., Kustas, W.P., 2007. A climatological study of evapotranspiration and moisture stress across the continental United States based on thermal remote sensing: 1. Model formulation. *J. Geophys. Res.-Atmos.* 112.
- Anderson, M.C., Norman, J.M., Meyers, T.P., Diak, G.R., 2000. An analytical model for estimating canopy transpiration and carbon assimilation fluxes based on canopy light-use efficiency. *Agric. For. Meteorol.* 101, 265-289.
- Arora, V., 2002. Modeling vegetation as a dynamic component in soil-vegetation-atmosphere transfer schemes and hydrological models. *Rev. Geophys.* 40.
- Asam, S., Fabritius, H., Klein, D., Conrad, C., Dech, S., 2013. Derivation of leaf area index for grassland within alpine upland using multi-temporal RapidEye data. *Int. J. Remote Sens.* 34, 8628-8652.
- Asrar, G., Fuchs, M., Kanemasu, E.T., Hatfield, J.L., 1984. ESTIMATING ABSORBED PHOTOSYNTHETIC RADIATION AND LEAF-AREA INDEX FROM SPECTRAL REFLECTANCE IN WHEAT. *Agron. J.* 76, 300-306.
- Atzberger, C., 2013. Advances in Remote Sensing of Agriculture: Context Description, Existing Operational Monitoring Systems and Major Information Needs. *Remote Sens.* 5, 949-981.
- Atzberger, C., Guerif, M., Baret, F., Werner, W., 2010. Comparative analysis of three chemometric techniques for the spectroradiometric assessment of canopy chlorophyll content in winter wheat. *Comput. Electron. Agric.* 73, 165-173.
- Aubin, I., Beaudet, M., Messier, C., 2000. Light extinction coefficients specific to the understory vegetation of the southern boreal forest, Quebec. *Can. J. For. Res.-Rev. Can. Rech. For.* 30, 168-177.
- Babin, S.M., 1995. SENSITIVITY OF AVERAGE ANNUAL RUNOFF TO SPATIAL VARIABILITY AND TEMPORAL CORRELATION OF RAINFALL. *J. Clim.* 8, 2104-2108.
- Bai, Y., Wong, M.S., Shi, W.Z., Wu, L.X., Qin, K., 2015. Advancing of Land Surface Temperature Retrieval Using Extreme Learning Machine and Spatio-Temporal Adaptive Data Fusion Algorithm. *Remote Sens.* 7, 4424-4441.
- Baker, S.W., 1979. Pore size distribution — A factor to be considered in infiltration studies? *J. Hydrol.* 41, 279-290.
- Baret, F., Guyot, G., 1991. POTENTIALS AND LIMITS OF VEGETATION INDEXES FOR LAI AND APAR ASSESSMENT. *Remote Sens. Environ.* 35, 161-173.

## Bibliography

- Barnett, T.L., Thompson, D.R., 1983. LARGE-AREA RELATION OF LANDSAT MSS AND NOAA-6 AVHRR SPECTRAL DATA TO WHEAT YIELDS. *Remote Sens. Environ.* 13, 277-290.
- Basarudin, H., Aziz, T.A.T., Sulaiman, M.I., Ali, A.H., Ieee, 2014. Preliminary study of EUMETSAT's Multi-Sensor Precipitation Estimate product for microwave links in Malaysia. 2014 4th International Conference on Engineering Technology and Technopreneurship (Ice2t), 218-221.
- Bastiaanssen, W.G.M., Menenti, M., Feddes, R.A., Holtslag, A.A.M., 1998a. A remote sensing surface energy balance algorithm for land (SEBAL) - 1. Formulation. *J. Hydrol.* 212, 198-212.
- Bastiaanssen, W.G.M., Pelgrum, H., Wang, J., Ma, Y., Moreno, J.F., Roerink, G.J., van der Wal, T., 1998b. A remote sensing surface energy balance algorithm for land (SEBAL) - 2. Validation. *J. Hydrol.* 212, 213-229.
- Beck, P.S.A., Atzberger, C., Hogda, K.A., Johansen, B., Skidmore, A.K., 2006. Improved monitoring of vegetation dynamics at very high latitudes: A new method using MODIS NDVI. *Remote Sens. Environ.* 100, 321-334.
- BfG-2011, Available Online at: [http://www.bafg.de/EN/03\\_The\\_%20BfG/the\\_bfg.html](http://www.bafg.de/EN/03_The_%20BfG/the_bfg.html). Accessed on July, 2, 2016.
- Bianchi, B., van Leeuwen, P.J., Hogan, R.J., Berne, A., 2013. A Variational Approach to Retrieve Rain Rate by Combining Information from Rain Gauges, Radars, and Microwave Links. *J. Hydrometeorol.* 14, 1897-1909.
- BlackBridge-RapidEye, 2013. Satellite Imagery Product Specifications. Internet: [http://www.blackbridge.com/rapideye/upload/RE\\_Product\\_Specifications\\_ENG.pdf](http://www.blackbridge.com/rapideye/upload/RE_Product_Specifications_ENG.pdf).
- Bogena, H., Hake, J.F., Herbst, M., Kunkel, R., Montzka, C., Putz, T., Vereecken, H., Wendland, F., 2005a. MOSYRUR – water balance analysis in the Rur basin. *Schriften des Forschungszentrums Juelich, Reihe Umwelt* 52.
- Bogena, H., Kunkel, R., Montzka, C., Wendland, F., 2005b. Uncertainties in the simulation of groundwater recharge at different scales. *Advances in Geosciences.* 5, 25-30.
- Bogena, H., Kunkel, R., Schobel, T., Schrey, H.P., Wendland, E., 2005c. Distributed modeling of groundwater recharge at the macroscale. *Ecol. Model.* 187, 15-26.
- Bogena, H., Schulz, K., Vereecken, H., 2006. Towards a network of observatories in terrestrial environmental research. *Advances in Geosciences* 9, 109-114.

## Bibliography

- Breda, N.J.J., 2003. Ground-based measurements of leaf area index: a review of methods, instruments and current controversies. *J. Exp. Bot.* 54, 2403-2417.
- Brisson, A., Borgne, P.L., Marsouin, A., 1999. Development of algorithms for Surface Solar Irradiance retrieval at O&SI SAF Low and Mid Latitudes. Available at: <http://citeseerx.ist.psu.edu/viewdoc/download?doi=10.1.1.133.9660&rep=rep1&type=pdf>.
- Cammalleri, C., Anderson, M.C., Ciraolo, G., D'Urso, G., Kustas, W.P., La Loggia, G., Minacapilli, M., 2012. Applications of a remote sensing-based two-source energy balance algorithm for mapping surface fluxes without in situ air temperature observations. *Remote Sens. Environ.* 124, 502-515.
- Cammalleri, C., Anderson, M.C., Gao, F., Hain, C.R., Kustas, W.P., 2013. A data fusion approach for mapping daily evapotranspiration at field scale. *Water Resour. Res.* 49, 4672-4686.
- Canty, M.J., Nielsen, A.A., 2008. Automatic radiometric normalization of multitemporal satellite imagery with the iteratively re-weighted MAD transformation. *Remote Sens. Environ.* 112, 1025-1036.
- Canty, M.J., Nielsen, A.A., Schmidt, M., 2004. Automatic radiometric normalization of multitemporal satellite imagery. *Remote Sens. Environ.* 91, 441-451.
- Chen, J.M., Blanken, P.D., Blank, T.A., Guilbeault, M., Chen, S., 1997. Radiation regime and canopy architecture in a boreal aspen forest. *Agric. For. Meteorol.* 86, 107-125.
- Chen, J.M., Cihlar, J., 1996. Retrieving leaf area index of boreal conifer forests using landsat TM images. *Remote Sens. Environ.* 55, 153-162.
- Chen, Y.Y., Chu, C.R., Li, M.H., 2012. A gap-filling model for eddy covariance latent heat flux: Estimating evapotranspiration of a subtropical seasonal evergreen broad-leaved forest as an example. *J. Hydrol.* 468, 101-110.
- Choudhury, B.J., Idso, S.B., Reginato, R.J., 1987. ANALYSIS OF AN EMPIRICAL-MODEL FOR SOIL HEAT-FLUX UNDER A GROWING WHEAT CROP FOR ESTIMATING EVAPORATION BY AN INFRARED-TEMPERATURE BASED ENERGY-BALANCE EQUATION. *Agric. For. Meteorol.* 39, 283-297.
- Clevers, J., 1988. THE DERIVATION OF A SIMPLIFIED REFLECTANCE MODEL FOR THE ESTIMATION OF LEAF-AREA INDEX. *Remote Sens. Environ.* 25, 53-69.
- Clevers, J., 1989. THE APPLICATION OF A WEIGHTED INFRARED-RED VEGETATION INDEX FOR ESTIMATING LEAF-AREA INDEX BY CORRECTING FOR SOIL-MOISTURE. *Remote Sens. Environ.* 29, 25-37.

- Clevers, J.G.P.W., 1986. APPLICATION OF REMOTE SENSING TO AGRICULTURAL FIELD TRIALS. Wageningen Agricultural University Papers 86, 1-227.
- Cohen, W.B., Maieresperger, T.K., Gower, S.T., Turner, D.P., 2003. An improved strategy for regression of biophysical variables and Landsat ETM+ data. *Remote Sens. Environ.* 84, 561-571.
- Colaizzi, P.D., Kustas, W.P., Anderson, M.C., Agam, N., Tolk, J.A., Evett, S.R., Howell, T.A., Gowda, P.H., O'Shaughnessy, S.A., 2012. Two-source energy balance model estimates of evapotranspiration using component and composite surface temperatures. *Adv. Water Resour.* 50, 134-151.
- Colliander, A., Jackson, T.J., Bindlish, R., Chan, S., Kim, S.B., Cosh, M.H., Dunbar, R.S., Dang, L., Pashaian, L., Asanuma, J., Berg, A.A., Rowlandson, T., Bosch, D., Caldwell, T., Caylor, K., Goodrich, D., Al Jassar, H., Lopez-Baeza, E., Martinez-Fernandez, J., Gonzalez-Zamora, A., Livingston, S., McNairn, H., Pacheco, A., Moghaddam, M., Montzka, C., Notarnicola, C., Niedrist, G., Pellarin, T., Prueger, J., Pulliainen, J., Rautiainen, K., Ramos, J., Seyfried, M., Starks, P., Su, Z., Zeng, Y., Van der Velde, R., Thibeault, M., Dorigo, W., Vreugdenhil, M., Walker, J.P., Wu, X., Monerris, A., O'Neill, P.E., Entekhabi, D., Njoku, E.G., Yueh, S.H., submitted. Validation of SMAP surface soil moisture products with core validation sites. *Remote Sens. Environ.*
- Colombo, R., Bellingeri, D., Fasolini, D., Marino, C.M., 2003. Retrieval of leaf area index in different vegetation types using high resolution satellite data. *Remote Sens. Environ.* 86, 120-131.
- Cristea, N.C., Kampf, S.K., Burges, S.J., 2013. Linear models for estimating annual and growing season reference evapotranspiration using averages of weather variables. *Int. J. Climatol.* 33, 376-387.
- Cristobal, J., Anderson, M.C., 2013. Validation of a Meteosat Second Generation solar radiation dataset over the northeastern Iberian Peninsula. *Hydrol. Earth Syst. Sci.* 17, 163-175.
- Curran, P.J., 1983. MULTISPECTRAL REMOTE-SENSING FOR THE ESTIMATION OF GREEN LEAF-AREA INDEX. *Philos. Trans. R. Soc. A-Math. Phys. Eng. Sci.* 309, 257-270.
- Dadson, S., Acreman, M., Harding, R., 2013. Water security, global change and land-atmosphere feedbacks. *Philos. Trans. R. Soc. A-Math. Phys. Eng. Sci.* 371, 17.

## Bibliography

- Darvishzadeh, R., Atzberger, C., Skidmore, A.K., Abkar, A.A., 2009. Leaf Area Index derivation from hyperspectral vegetation indices and the red edge position. *Int. J. Remote Sens.* 30, 6199-6218.
- Delegido, J., Verrelst, J., Alonso, L., Moreno, J., 2011. Evaluation of Sentinel-2 Red-Edge Bands for Empirical Estimation of Green LAI and Chlorophyll Content. *Sensors* 11, 7063-7081.
- Deng, F., Chen, J.M., Plummer, S., Chen, M.Z., Pisek, J., 2006. Algorithm for global leaf area index retrieval using satellite imagery. *IEEE Trans. Geosci. Remote Sensing* 44, 2219-2229.
- Derin, Y., Yilmaz, K.K., 2014. Evaluation of Multiple Satellite-Based Precipitation Products over Complex Topography. *J. Hydrometeorol.* 15, 1498-1516.
- Devi, G.K., Ganasri, B.P., Dwarakish, G.S., 2015. A Review on Hydrological Models. In: Dwarakish, G.S. (Ed.), *International Conference on Water Resources, Coastal and Ocean Engineering*. Elsevier Science Bv, Amsterdam, pp. 1001-1007.
- Diederich, M., Ryzhkov, A., Simmer, C., Zhang, P.F., Tromel, S., 2015a. Use of Specific Attenuation for Rainfall Measurement at X-Band Radar Wavelengths. Part I: Radar Calibration and Partial Beam Blockage Estimation. *J. Hydrometeorol.* 16, 487-502.
- Diederich, M., Ryzhkov, A., Simmer, C., Zhang, P.F., Tromel, S., 2015b. Use of Specific Attenuation for Rainfall Measurement at X-Band Radar Wavelengths. Part II: Rainfall Estimates and Comparison with Rain Gauges. *J. Hydrometeorol.* 16, 503-516.
- Duchemin, B., Hadria, R., Erraki, S., Boulet, G., Maisongrande, P., Chehbouni, A., Escadafal, R., Ezzahar, J., Hoedjes, J.C.B., Kharrou, M.H., Khabba, S., Mougenot, B., Olioso, A., Rodriguez, J.C., Simonneaux, V., 2006. Monitoring wheat phenology and irrigation in Central Morocco: On the use of relationships between evapotranspiration, crops coefficients, leaf area index and remotely-sensed vegetation indices. *Agric. Water Manage.* 79, 1-27.
- Duggin, M.J., Piwinski, D., 1984. RECORDED RADIANCE INDEXES FOR VEGETATION MONITORING USING NOAA AVHRR DATA - ATMOSPHERIC AND OTHER EFFECTS IN MULTITEMPORAL DATA SETS. *Appl. Optics* 23, 2620-2623.
- Eder, F., Schmidt, M., Damian, T., Traumner, K., Mauder, M., 2015. Mesoscale Eddies Affect Near-Surface Turbulent Exchange: Evidence from Lidar and Tower Measurements. *J. Appl. Meteorol. Climatol.* 54, 189-206.



## Bibliography

- EDO-2011a, Available Online at:  
<http://edo.jrc.ec.europa.eu/documents/news/EDODroughtNews201104.pdf>.  
Accessed on July, 2, 2016.
- EDO-2011b, Available Online at:  
<http://edo.jrc.ec.europa.eu/documents/news/EDODroughtNews201105.pdf>.  
Accessed on July, 2, 2016.
- EDO-2015, Available Online at:  
<http://edo.jrc.ec.europa.eu/documents/news/EDODroughtNews201508.pdf>.  
Accessed on July, 2, 2016.
- Ehammer, A., Fritsch, S., Conrad, C., Lamers, J., Dech, S., 2010. Statistical derivation of fPAR and LAI for irrigated cotton and rice in arid Uzbekistan by combining multi-temporal RapidEye data and ground measurements. In: Neale, C.M.U., Maltese, A. (Eds.), Remote Sensing for Agriculture, Ecosystems, and Hydrology Xii. Spie-Int Soc Optical Engineering, Bellingham.
- Eitel, J.U.H., Long, D.S., Gessler, P.E., Smith, A.M.S., 2007. Using in-situ measurements to evaluate the new RapidEye (TM) satellite series for prediction of wheat nitrogen status. *Int. J. Remote Sens.* 28, 4183-4190.
- Eitel, J.U.H., Vierling, L.A., Litvak, M.E., Long, D.S., Schulthess, U., Ager, A.A., Krofcheck, D.J., Stoscheck, L., 2011. Broadband, red-edge information from satellites improves early stress detection in a New Mexico conifer woodland. *Remote Sens. Environ.* 115, 3640-3646.
- EUMETSAT's-MPE, Available online at:  
[http://www.eumetsat.int/website/home/News/DAT\\_2602960.html](http://www.eumetsat.int/website/home/News/DAT_2602960.html). Accessed on August, 2, 2016.
- Fabry, F., 2015. Radar Meteorology: Principles and Practices. Cambridge University Press, United Kingdom, 272.
- Falge, E., Baldocchi, D., Olson, R., Anthoni, P., Aubinet, M., Bernhofer, C., Burba, G., Ceulemans, R., Clement, R., Dolman, H., Granier, A., Gross, P., Grunwald, T., Hollinger, D., Jensen, N.O., Katul, G., Keronen, P., Kowalski, A., Lai, C.T., Law, B.E., Meyers, T., Moncrieff, H., Moors, E., Munger, J.W., Pilegaard, K., Rannik, U., Rebmann, C., Suyker, A., Tenhunen, J., Tu, K., Verma, S., Vesala, T., Wilson, K., Wofsy, S., 2001. Gap filling strategies for defensible annual sums of net ecosystem exchange. *Agric. For. Meteorol.* 107, 43-69.

## Bibliography

- Filella, I., Penuelas, J., 1994. The red edge position and shape as indicators of plant chloro phyll content, biomass and hydric status. *International Journal of Remote Sensing* 15, 1459 - 1470.
- Fox, D.M., Bryan, R.B., Price, A.G., 1997. The influence of slope angle on final infiltration rate for interrill conditions. *Geoderma* 80, 181-194.
- Frouin, R., Lingner, D.W., Gautier, C., Baker, K.S., Smith, R.C., 1989. A SIMPLE ANALYTICAL FORMULA TO COMPUTE CLEAR SKY TOTAL AND PHOTOSYNTHETICALLY AVAILABLE SOLAR IRRADIANCE AT THE OCEAN SURFACE. *J. Geophys. Res.-Oceans* 94, 9731-9742.
- Gao, F., Anderson, M.C., Kustas, W.P., Wang, Y.J., 2012. Simple method for retrieving leaf area index from Landsat using MODIS leaf area index products as reference. *J. Appl. Remote Sens.* 6, 15.
- Gautier, C., Diak, G., Masse, S., 1980. A SIMPLE PHYSICAL MODEL TO ESTIMATE INCIDENT SOLAR-RADIATION AT THE SURFACE FROM GOES SATELLITE DATA. *J. Appl. Meteorol.* 19, 1005-1012.
- Ge, J.J., 2009. On the Proper Use of Satellite-Derived Leaf Area Index in Climate Modeling. *J. Clim.* 22, 4427-4433.
- Geerken, R., Zaitchik, B., Evans, J.P., 2005. Classifying rangeland vegetation type and coverage from NDVI time series using Fourier Filtered Cycle Similarity. *Int. J. Remote Sens.* 26, 5535-5554.
- Gerten, D., Schaphoff, S., Haberlandt, U., Lucht, W., Sitch, S., 2004. Terrestrial vegetation and water balance - hydrological evaluation of a dynamic global vegetation model. *J. Hydrol.* 286, 249-270.
- Gitelson, A., Merzlyak, M.N., 1994a. QUANTITATIVE ESTIMATION OF CHLOROPHYLL-A USING REFLECTANCE SPECTRA - EXPERIMENTS WITH AUTUMN CHESTNUT AND MAPLE LEAVES. *J. Photochem. Photobiol. B-Biol.* 22, 247-252.
- Gitelson, A., Merzlyak, M.N., 1994b. SPECTRAL REFLECTANCE CHANGES ASSOCIATED WITH AUTUMN SENESCENCE OF AESCULUS-HIPPOCASTANUM L AND ACER-PLATANOIDES L LEAVES - SPECTRAL FEATURES AND RELATION TO CHLOROPHYLL ESTIMATION. *J. Plant Physiol.* 143, 286-292.

- Gong, L.B., Xu, C.Y., Chen, D.L., Halldin, S., Chen, Y.Q.D., 2006. Sensitivity of the Penman-Monteith reference evapotranspiration to key climatic variables in the Changjiang (Yangtze River) basin. *J. Hydrol.* 329, 620-629.
- GPCC-2011, Available Online at: <https://climatedataguide.ucar.edu/climate-data/gpcc-global-precipitation-climatology-centre>. Accessed on July, 2, 2016.
- Graf, A., Bogena, H.R., Drue, C., Hardelauf, H., Putz, T., Heinemann, G., Vereecken, H., 2014. Spatiotemporal relations between water budget components and soil water content in a forested tributary catchment. *Water Resour. Res.* 50, 4837-4857.
- Graf, A., Werner, J., Langensiepen, M., van de Boer, A., Schmidt, M., Kupisch, M., Vereecken, H., 2013. Validation of a minimum microclimate disturbance chamber for net ecosystem flux measurements. *Agric. For. Meteorol.* 174, 1-14.
- Gu, Z.J., Shi, X.Z., Li, L., Yu, D.S., Liu, L.S., Zhang, W.T., 2011. Using multiple radiometric correction images to estimate leaf area index. *Int. J. Remote Sens.* 32, 9441-9454.
- Haboudane, D., Miller, J.R., Pattey, E., Zarco-Tejada, P.J., Strachan, I.B., 2004. Hyperspectral vegetation indices and novel algorithms for predicting green LAI of crop canopies: Modeling and validation in the context of precision agriculture. *Remote Sens. Environ.* 90, 337-352.
- Hadjimitsis, D.G., Papadavid, G., Agapiou, A., Themistocleous, K., Hadjimitsis, M.G., Retalis, A., Michaelides, S., Chrysoulakis, N., Toullos, L., Clayton, C.R.I., 2010. Atmospheric correction for satellite remotely sensed data intended for agricultural applications: impact on vegetation indices. *Nat. Hazards Earth Syst. Sci.* 10, 89-95.
- Haghnazari, F., Shahgholi, H., Feizi, M., 2015. Factors affecting the infiltration of agricultural soils: review. *International Journal of Agronomy and Agricultural Research* 6(5), 21-35.
- Hall, F.G., 1991. Radiometric rectification: Toward a common Radiometric response among multirate, multisensor images. *Remote Sens. Environ.* 35, 11-27.
- Han, X.J., Li, X., Rigon, R., Jin, R., Endrizzi, S., 2015. Soil Moisture Estimation by Assimilating L-Band Microwave Brightness Temperature with Geostatistics and Observation Localization. *PLoS One* 10, 20.
- Hasan, S., Montzka, C., Rudiger, C., Ali, M., Bogena, H.R., Vereecken, H., 2014. Soil moisture retrieval from airborne L-band passive microwave using high resolution multispectral data. *ISPRS-J. Photogramm. Remote Sens.* 91, 59-71.
- Hattermann, F.F., Huang, S., Koch, H., 2015. Climate change impacts on hydrology and water resources. *Meteorol. Z.* 24, 201-211.

## Bibliography

- Heinemann, T., Latanzio, A., Roveda, F., 2002. The EUMETSAT multi-sensor precipitation estimate (MPE). EUMETSAT Rep., 8 pp. [Available online at [http://oiswww.eumetsat.int/;idds/html/doc/IPWG\\_2002\\_MPE.pdf](http://oiswww.eumetsat.int/;idds/html/doc/IPWG_2002_MPE.pdf)].
- Huang, J., Wu, P.T., Zhao, X.N., 2013. Effects of rainfall intensity, underlying surface and slope gradient on soil infiltration under simulated rainfall experiments. *Catena* 104, 93-102.
- Huete, A.R., 1988. A SOIL-ADJUSTED VEGETATION INDEX (SAVI). *Remote Sens. Environ.* 25, 295-309.
- Huntington, T.G., 2006. Evidence for intensification of the global water cycle: Review and synthesis. *J. Hydrol.* 319, 83-95.
- Irmak, S., Irmak, A., Allen, R.G., Jones, J.W., 2003. Solar and net radiation-based equations to estimate reference evapotranspiration in humid climates. *J. Irrig. Drainage Eng-ASCE* 129, 336-347.
- Irmak, S., Payero, J.O., Martin, D.L., Irmak, A., Howell, T.A., 2006. Sensitivity analyses and sensitivity coefficients of standardized daily ASCE-Penman-Monteith equation. *J. Irrig. Drainage Eng-ASCE* 132, 564-578.
- Jacquemoud, S., Verhoef, W., Baret, F., Bacour, C., Zarco-Tejada, P.J., Asner, G.P., Francois, C., Ustin, S.L., 2009. PROSPECT plus SAIL models: A review of use for vegetation characterization. *Remote Sens. Environ.* 113, S56-S66.
- Jonckheere, I., Fleck, S., Nackaerts, K., Muys, B., Coppin, P., Weiss, M., Baret, F., 2004. Review of methods for in situ leaf area index determination - Part I. Theories, sensors and hemispherical photography. *Agric. For. Meteorol.* 121, 19-35.
- Jung, M., Reichstein, M., Ciais, P., Seneviratne, S.I., Sheffield, J., Goulden, M.L., Bonan, G., Cescatti, A., Chen, J.Q., de Jeu, R., Dolman, A.J., Eugster, W., Gerten, D., Gianelle, D., Gobron, N., Heinke, J., Kimball, J., Law, B.E., Montagnani, L., Mu, Q.Z., Mueller, B., Oleson, K., Papale, D., Richardson, A.D., Rouspard, O., Running, S., Tomelleri, E., Viovy, N., Weber, U., Williams, C., Wood, E., Zaehle, S., Zhang, K., 2010. Recent decline in the global land evapotranspiration trend due to limited moisture supply. *Nature* 467, 951-954.
- Kalma, J.D., McVicar, T.R., McCabe, M.F., 2008. Estimating Land Surface Evaporation: A Review of Methods Using Remotely Sensed Surface Temperature Data. *Surv. Geophys.* 29, 421-469.
- Kite, G.W., Pietroniro, A., 1996. Remote sensing applications in hydrological modelling. *Hydrol. Sci. J.-J. Sci. Hydrol.* 41, 563-591.

## Bibliography

- Kovoor, G.M., Nandagiri, L., 2007. Developing regression models for predicting pan evaporation from climatic data - A comparison of multiple least-squares, principal components, and partial least-squares approaches. *J. Irrig. Drainage Eng-ASCE* 133, 444-454.
- Kundzewicz, Z., Gerstengarbe, F.W., Osterle, H., Werner, P., Fricke, W., 2009. Recent anomalies of mean temperature of 12 consecutive months - Germany, Europe, Northern Hemisphere. *Theor. Appl. Climatol.* 95, 417-422.
- Kundzewicz, Z., W., 2008. Climate change impacts on the hydrological cycle. *Ecohydrology & Hydrobiology* 8, 195-203.
- Kundzewicz, Z.W., Kaczmarek, Z., 2000. Coping with hydrological extremes. *Water Int.* 25, 66-75.
- Kustas, W., Anderson, M., 2009. Advances in thermal infrared remote sensing for land surface modeling. *Agric. For. Meteorol.* 149, 2071-2081.
- Kustas, W.P., Hatfield, J.L., Prueger, J.H., 2005. The soil moisture-atmosphere coupling experiment (SMACEX): Background, hydrometeorological conditions, and preliminary findings. *J. Hydrometeorol.* 6, 791-804.
- Kustas, W.P., Norman, J.M., 1999. Evaluation of soil and vegetation heat flux predictions using a simple two-source model with radiometric temperatures for partial canopy cover. *Agric. For. Meteorol.* 94, 13-29.
- L'vovich, M.I., 1979. *World Water Resources and their Future*. Original in Russian. English Translation, American Geophysical Union, Washington, D.C.
- Land-SAF\_DSSF, 2011. The EUMETSAT Satellite Application Facility on Land Surface Analysis (Land-SAF), Product User Manual, Downwelling Shortwave Flux (DSSF). Reference Number: SAF/LAND/MF/PUM\_DSSF/2.6v2, available at: <https://landsaf.meteo.pt/algorithms.jsp?seltab=1&starttab=1>.
- Land-SAF\_LST, 2015. The EUMETSAT Satellite Application Facility on Land Surface Analysis (Land-SAF), Product User Manual, Land Surface Temperature (LST). Reference Number: SAF/LAND/IPMA/PUM\_LST/2.6 Available at: <http://landsaf.meteo.pt/algorithms.jsp?seltab=0&starttab=0>.
- Li, F.Q., Kustas, W.P., Prueger, J.H., Neale, C.M.U., Jackson, T.J., 2005. Utility of remote sensing-based two-source energy balance model under low- and high-vegetation cover conditions. *J. Hydrometeorol.* 6, 878-891.

## Bibliography

- Loumagne, C., Normand, M., Riffard, M., Weisse, A., Quesney, A., Le Hegarat-Masclé, S., Alem, F., 2001. Integration of remote sensing data into hydrological models for reservoir management. *Hydrol. Sci. J.-J. Sci. Hydrol.* 46, 89-102.
- Lussem, U., Waldhoff, G., 2013. Enhanced land use classification of 2011 for the Rur catchment. *CRC/TR32 Database (TR32DB)* DOI: 10.5880/TR32DB.7.
- Maes, W.H., Steppe, K., 2012. Estimating evapotranspiration and drought stress with ground-based thermal remote sensing in agriculture: a review. *J. Exp. Bot.* 63, 4671-4712.
- Mallick, K., Jarvis, A.J., Boegh, E., Fisher, J.B., Drewry, D.T., Tu, K.P., Hook, S.J., Hulley, G., Ardo, J., Beringer, J., Arain, A., Niyogi, D., 2014. A Surface Temperature Initiated Closure (STIC) for surface energy balance fluxes. *Remote Sens. Environ.* 141, 243-261.
- Markham, B.L., Storey, J.C., Irons, J.R., 2013. Landsat Data Continuity Mission - Now Landsat-8: Six Months on Orbit. In: Butler, J.J., Xiong, X., Gu, X. (Eds.), *Earth Observing Systems XVIII. Spie-Int Soc Optical Engineering*, Bellingham.
- Matrosov, S.Y., Clark, K.A., Kingsmill, D.E., 2007. A polarimetric radar approach to identify rain, melting-layer, and snow regions for applying corrections to vertical profiles of reflectivity. *J. Appl. Meteorol. Climatol.* 46, 154-166.
- McGlynn, B.L., Bloeschl, G., Borga, M., Bormann, H., Hurkmans, R., Komma, J., Nandagiri, L., Uijlenhoet, R., Wagener, T., 2012. A data acquisition framework for prediction of runoff in ungauged basins, In *Run-off Prediction in Ungauged Basins: Synthesis Across Processes, Places and Scales* (eds Bloeschl, G., Sivapalan, M., T. Wagener, T., Viglione, A. and Savenije, H.). Cambridge Univ. Press, DOI: 10.1017/CBO9781139235761.006, 29-51.
- McKee, T.B.N., Doesken, J., Kleist, J., 1993. The relationship of drought frequency and duration to time scales. *Eight Conf. On Applied Climatology*. Anaheim, CA, Amer. Meteor. Soc., 179-184.
- McMahon, T., Peel, M.C., Lowe, L., Srikanthan, R., McVicar, T.R., 2013. Estimating actual, potential, reference crop and pan evaporation using standard meteorological data: A pragmatic synthesis" published in *Hydrology and Earth System Sciences* (vol 17, pg 1331, 2013). *Hydrol. Earth Syst. Sci.* 17, 4503-4503.
- Mecherikunnel, A., Weiss, M., Penn, L., 1995. THE ESTIMATION OF EMITTED AND REFLECTED ENERGY OVER THE CENTRAL PACIFIC USING METEOROLOGICAL PARAMETERS. *J. Clim.* 8, 762-772.

## Bibliography

- Mecikalski, J.R., Diak, G.R., Anderson, M.C., Norman, J.M., 1999. Estimating fluxes on continental scales using remotely sensed data in an atmospheric-land exchange model. *J. Appl. Meteorol.* 38, 1352-1369.
- Milly, P.C.D., 1994. CLIMATE, SOIL-WATER STORAGE, AND THE AVERAGE ANNUAL WATER-BALANCE. *Water Resour. Res.* 30, 2143-2156.
- Mirzaie, M., Darvishzadeh, R., Shakiba, A., Matkan, A.A., Atzberger, C., Skidmore, A., 2014. Comparative analysis of different uni- and multi-variate methods for estimation of vegetation water content using hyper-spectral measurements. *Int. J. Appl. Earth Obs. Geoinf.* 26, 1-11.
- Mokhtari, M.H., Ahmad, B., Hoveidi, H., Busu, I., 2013. Sensitivity Analysis of METRIC-Based Evapotranspiration Algorithm. *Int. J. Environ. Res.* 7, 407-422.
- Montzka, C., Bogena, H.R., Weihermuller, L., Jonard, F., Bouzinac, C., Kainulainen, J., Balling, J.E., Loew, A., Dall'Amico, J.T., Rouhe, E., Vanderborght, J., Vereecken, H., 2013. Brightness Temperature and Soil Moisture Validation at Different Scales During the SMOS Validation Campaign in the Rur and Erft Catchments, Germany. *IEEE Trans. Geosci. Remote Sensing* 51, 1728-1743.
- Montzka, C., Canty, M., Kreins, P., Kunkel, R., Menz, G., Vereecken, H., Wendland, F., 2008a. Multispectral remotely sensed data in modelling the annual variability of nitrate concentrations in the leachate. *Environ. Modell. Softw.* 23, 1070-1081.
- Montzka, C., Canty, M., Kunkel, R., Menz, G., Vereecken, H., Wendland, F., 2008b. Modelling the water balance of a mesoscale catchment basin using remotely sensed land cover data. *J. Hydrol.* 353, 322-334.
- Montzka, C., Jagdhuber, T., Horn, R., Bogena, H., Hajnsek, I., Reigber, A., Vereecken, H., 2016. Investigation of SMAP fusion algorithms with airborne active and passive L-band microwave remote sensing. *IEEE Transactions on Geosciences and Remote Sensing* 54(7), 3878-3889.
- Moradkhani, H., 2008. Hydrologic remote sensing and land surface data assimilation. *Sensors* 8, 2986-3004.
- Mu, Q.Z., Zhao, M.S., Running, S.W., 2011. Evolution of hydrological and carbon cycles under a changing climate. Part III: global change impacts on landscape scale evapotranspiration. *Hydrol. Process.* 25, 4093-4102.
- NASA-GPM, Available online at: <https://pmm.nasa.gov/GPM>. Accessed on August, 2, 2016.
- NASA-TRMM, Available online at: <http://trmm.gsfc.nasa.gov/>. Accessed on August, 2, 2016.

## Bibliography

- Norman, J.M., Anderson, M.C., Kustas, W.P., French, A.N., Mecikalski, J., Torn, R., Diak, G.R., Schmugge, T.J., Tanner, B.C.W., 2003. Remote sensing of surface energy fluxes at 10(1)-m pixel resolutions. *Water Resour. Res.* 39, 18.
- Norman, J.M., Kustas, W.P., Humes, K.S., 1995. Source Approach for Estimating Soil and Vegetation Energy Fluxes in Observations of Directional Radiometric Surface-temperature. *Agric. For. Meteorol.* 77, 263-293.
- Norman, J.M., Kustas, W.P., Humes, K.S., 1996. Source approach for estimating soil and vegetation energy fluxes in observations of directional radiometric surface temperature (vol 77, pg 263, 1995). *Agric. For. Meteorol.* 80, 297-297.
- Norman, J.M., Kustas, W.P., Prueger, J.H., Diak, G.R., 2000. Surface flux estimation using radiometric temperature: A dual temperature-difference method to minimize measurement errors. *Water Resour. Res.* 36, 2263-2274.
- O'Driscoll, M., Clinton, S., Jefferson, A., Manda, A., McMillan, S., 2010. Urbanization Effects on Watershed Hydrology and In-Stream Processes in the Southern United States. *Water* 2, 605-648.
- Oki, T., Kanae, S., 2006. Global hydrological cycles and world water resources. *Science* 313, 1068-1072.
- Pan, M., Wood, E.F., Wojcik, R., McCabe, M.F., 2008. Estimation of regional terrestrial water cycle using multi-sensor remote sensing observations and data assimilation. *Remote Sens. Environ.* 112, 1282-1294.
- Parajka, J., Viglione, A., Rogger, M., Salinas, J.L., Sivapalan, M., Blöschl, G., 2013. Comparative assessment of predictions in ungauged basins - Part 1: Runoff-hydrograph studies. *Hydrol. Earth Syst. Sci.* 17, 1783-1795.
- Pechlivanidis, I.G., Jackson, B.M., McIntyre, N.R., Wheater, H.S., 2011. CATCHMENT SCALE HYDROLOGICAL MODELLING: A REVIEW OF MODEL TYPES, CALIBRATION APPROACHES AND UNCERTAINTY ANALYSIS METHODS IN THE CONTEXT OF RECENT DEVELOPMENTS IN TECHNOLOGY AND APPLICATIONS. *Glob. Nest. J.* 13, 193-214.
- Pietroniro, A., Prowse, T.D., 2002. Preface - Applications of remote sensing in hydrology. *Hydrol. Process.* 16, 1537-1541.
- PlanetLabs, Planet Labs. Available online: [https://www.planet.com/?utm\\_source=planet&utm\\_medium=blog&utm\\_content=company-news&utm\\_campaign=2015-07-15-acquisition](https://www.planet.com/?utm_source=planet&utm_medium=blog&utm_content=company-news&utm_campaign=2015-07-15-acquisition).



- Ponce, V.M., Shetty, A.V., 1995. A CONCEPTUAL-MODEL OF CATCHMENT WATER-BALANCE .1. FORMULATION AND CALIBRATION. *J. Hydrol.* 173, 27-40.
- Propastin, P., Erasmi, S., 2010. A physically based approach to model LAI from MODIS 250 m data in a tropical region. *Int. J. Appl. Earth Obs. Geoinf.* 12, 47-59.
- Propastin, P., Panferov, O., 2013. Retrieval of remotely sensed LAI using Landsat ETM plus data and ground measurements of solar radiation and vegetation structure: Implication of leaf inclination angle. *Int. J. Appl. Earth Obs. Geoinf.* 25, 38-46.
- Pu, R.L., Gong, P., 2004. Wavelet transform applied to EO-1 hyperspectral data for forest LAI and crown closure mapping. *Remote Sens. Environ.* 91, 212-224.
- Qi, J., Marsett, R.C., Moran, M.S., Goodrich, D.C., Heilman, P., Kerr, Y.H., Dedieu, G., Chehbouni, A., Zhang, X.X., 2000. Spatial and temporal dynamics of vegetation in the San Pedro River basin area. *Agric. For. Meteorol.* 105, 55-68.
- Reichenau, T., Korres, W., Schneider, K., Fiener, P., Wilken, F., Stadler, A., Montzka, C., Waldhoff, G., 2016. The seasonal course of LAI spatial heterogeneity on arable land: combining field measurements, remote sensing and simulation. *PLoS One*.
- Rembold, F., Atzberger, C., Savin, I., Rojas, O., 2013. Using Low Resolution Satellite Imagery for Yield Prediction and Yield Anomaly Detection. *Remote Sens.* 5, 1704-1733.
- Reuter, D.C., Richardson, C.M., Pellerano, F.A., Irons, J.R., Allen, R.G., Anderson, M., Jhabvala, M.D., Lunsford, A.W., Montanaro, M., Smith, R.L., Tesfaye, Z., Thome, K.J., 2015. The Thermal Infrared Sensor (TIRS) on Landsat 8: Design Overview and Pre-Launch Characterization. *Remote Sens.* 7, 1135-1153.
- Ribolzi, O., Patin, J., Bresson, L.M., Latschack, K.O., Mouche, E., Sengtaheuanghong, O., Silvera, N., Thiebaut, J.P., Valentin, C., 2011. Impact of slope gradient on soil surface features and infiltration on steep slopes in northern Laos. *Geomorphology* 127, 53-63.
- Richter, R., 1996a. Atmospheric correction of satellite data with haze removal including a haze/clear transition region. *Comput. Geosci.* 22, 675-681.
- Richter, R., 1996b. A spatially adaptive fast atmospheric correction algorithm. *Int. J. Remote Sens.* 17, 1201-1214.
- Rind, D., 1984. The Influence of Vegetation on the Hydrologic Cycle in a Global Climate Model, In *Climate Processes and Climate Sensitivity* (eds Hansen, J. E. and Takahashi, T.). Geophysical Union, Washington, D. C., DOI: 10.1029/GM029p0073.

## Bibliography

- Rogger, M., Kohl, B., Pirkl, H., Viglione, A., Komma, J., Kirnbauer, R., Merz, R., Bloschl, G., 2012. Runoff models and flood frequency statistics for design flood estimation in Austria - Do they tell a consistent story? *J. Hydrol.* 456, 30-43.
- Rötzer, K., Montzka, C., Bogena, H., Wegner, W., Kerr, Y.H., Kidd, R., Vereecken, H., 2014. Catchment scale validation of SMOS and ASCAT soil moisture products using hydrological modeling and temporal stability analysis. *J. Hydrol.* 519, 934-946.
- Rouse, J.W., Haas, R.H., Schell, J.A., Deering, D.W., 1973. Monitoring vegetation systems in the great plains with ERTS. In: S. C. Freden, E. P. Mercanti, and M. Becker [EDS.]. Third earth resources technology satellite-1 symposium. Volume I: Technical presentations. NASA SP-351. Washington, DC, 309-317.
- Rudolph, S., van der Kruk, J., von Hebel, C., Ali, M., Herbst, M., Montzka, C., Pätzold, S., Robinson, D.A., Vereecken, H., Weiermüller, L., 2015. Linking satellite derived LAI patterns with subsoil heterogeneity using large-scale ground-based electromagnetic induction measurements. *Geoderma* 241-242, 262-271.
- Sala, O.E., Gherardi, L.A., Peters, D.P.C., 2015. Enhanced precipitation variability effects on water losses and ecosystem functioning: differential response of arid and mesic regions. *Clim. Change* 131, 213-227.
- Schlerf, M., Atzberger, C., 2006. Inversion of a forest reflectance model to estimate structural canopy variables from hyperspectral remote sensing data. *Remote Sens. Environ.* 100, 281-294.
- Schmugge, T.J., Kustas, W.P., Ritchie, J.C., Jackson, T.J., Rango, A., 2002. Remote sensing in hydrology. *Adv. Water Resour.* 25, 1367-1385.
- Schumacher, P., Mislímshoeva, B., Brenning, A., Zandler, H., Brandt, M., Samimi, C., Koellner, T., 2016. Do Red Edge and Texture Attributes from High-Resolution Satellite Data Improve Wood Volume Estimation in a Semi-Arid Mountainous Region? *Remote Sens.* 8(7), 540.
- Schuster, C., Forster, M., Kleinschmit, B., 2012. Testing the red edge channel for improving land-use classifications based on high-resolution multi-spectral satellite data. *Int. J. Remote Sens.* 33, 5583-5599.
- Scipal, K., Holmes, T., de Jeu, R., Naeimi, V., Wagner, W., 2008. A possible solution for the problem of estimating the error structure of global soil moisture data sets. *Geophys. Res. Lett.* 35, 4.

## Bibliography

- Scipal, K., Scheffler, C., Wagner, W., 2005. Soil moisture-runoff relation at the catchment scale as observed with coarse resolution microwave remote sensing. *Hydrol. Earth Syst. Sci.* 9, 173-183.
- Sellers, P.J., Dickinson, R.E., Randall, D.A., Betts, A.K., Hall, F.G., Berry, J.A., Collatz, G.J., Denning, A.S., Mooney, H.A., Nobre, C.A., Sato, N., Field, C.B., Henderson-Sellers, A., 1997. Modeling the exchanges of energy, water, and carbon between continents and the atmosphere. *Science* 275, 502-509.
- Sheffield, J., Wood, E.F., Chaney, N., Guan, K.Y., Sadri, S., Yuan, X., Olang, L., Abou, A., Ali, A., Demuth, S., Ogallo, L., 2014. A DROUGHT MONITORING AND FORECASTING SYSTEM FOR SUB-SAHARA AFRICAN WATER RESOURCES AND FOOD SECURITY. *Bull. Amer. Meteorol. Soc.* 95, 861-+.
- Shelton, M.L., 2009. *Hydroclimatology: Perspectives and Applications*. Cambridge University Press, 426.
- Shuster, W.D., Bonta, J., Thurston, H., Warnemuende, E., Smith, D.R., 2005. Impacts of impervious surface on watershed hydrology: a review. *Urban Water Journal* 2(4), 263–275.
- Sims, D.A., Gamon, J.A., 2002. Relationships between leaf pigment content and spectral reflectance across a wide range of species, leaf structures and developmental stages. *Remote Sens. Environ.* 81, 337-354.
- Sivapalan, M., Takeuchi, K., Franks, S.W., Gupta, V.K., Karambiri, H., Lakshmi, V., Liang, X., McDonnell, J.J., Mendiondo, E.M., O'Connell, P.E., Oki, T., Pomeroy, J.W., Schertzer, D., Uhlenbrook, S., Zehe, E., 2003. IAHS decade on Predictions in Ungauged Basins (PUB), 2003-2012: Shaping an exciting future for the hydrological sciences. *Hydrol. Sci. J.-J. Sci. Hydrol.* 48, 857-880.
- Smith, B., Samuelsson, P., Wramneby, A., Rummukainen, M., 2011. A model of the coupled dynamics of climate, vegetation and terrestrial ecosystem biogeochemistry for regional applications. *Tellus Ser. A-Dyn. Meteorol. Oceanol.* 63, 87-106.
- Sprintsin, M., Karnieli, A., Berliner, P., Rotenberg, E., Yakir, D., Cohen, S., 2007. The effect of spatial resolution on the accuracy of leaf area index estimation for a forest planted in the desert transition zone. *Remote Sens. Environ.* 109, 416-428.
- Stadler, A., Rudolph, S., Kupisch, M., Langensiepen, M., van der Kruk, J., Ewert, F., 2015. Quantifying the effects of soil variability on crop growth using apparent soil electrical conductivity measurements. *Europ. J. Agronomy* 64, 8-20.

## Bibliography

- Stanislaus, J., Schymanski, Dani, O., 2016. Leaf-scale experiments reveal important omission in the Penman-Monteith equation. *Hydrol. Earth Syst. Sci. Discuss.*, DOI:10.5194/hess-2016-363.
- Syed, T.H., Famiglietti, J.S., Chambers, D.P., Willis, J.K., Hilburn, K., 2010. Satellite-based global-ocean mass balance estimates of interannual variability and emerging trends in continental freshwater discharge. *Proc. Natl. Acad. Sci. U. S. A.* 107, 17916-17921.
- TERENO, Terrestrial Environmental Observatories. Available online: [http://teodoor.icg.kfa-juelich.de/overview-en?set\\_language=en](http://teodoor.icg.kfa-juelich.de/overview-en?set_language=en).
- Thompson, S.E., Harman, C.J., Konings, A.G., Sivapalan, M., Neal, A., Troch, P.A., 2011. Comparative hydrology across AmeriFlux sites: The variable roles of climate, vegetation, and groundwater. *Water Resour. Res.* 47.
- Thorp, K.R., Batchelor, W.D., Paz, J.O., Kaleita, A.L., DeJonge, K.C., 2007. Using cross-validation to evaluate CERES-Maize yield simulations within a decision support system for precision agriculture. *Trans. ASABE* 50, 1467-1479.
- Trenberth, K.E., Fasullo, J.T., Kiehl, J., 2009. EARTH'S GLOBAL ENERGY BUDGET. *Bull. Amer. Meteorol. Soc.* 90, 311-+.
- Trigo, I.F., Dacamara, C.C., Viterbo, P., Roujean, J.L., Olesen, F., Barroso, C., Camacho-de-Coca, F., Carrer, D., Freitas, S.C., Garcia-Haro, J., Geiger, B., Gellens-Meulenberghs, F., Ghilain, N., Melia, J., Pessanha, L., Siljamo, N., Arboleda, A., 2011. The Satellite Application Facility for Land Surface Analysis. *Int. J. Remote Sens.* 32, 2725-2744.
- Turner, D.P., Cohen, W.B., Kennedy, R.E., Fassnacht, K.S., Briggs, J.M., 1999. Relationships between leaf area index and Landsat TM spectral vegetation indices across three temperate zone sites. *Remote Sens. Environ.* 70, 52-68.
- Uijlenhoet, R., 2001. Raindrop size distributions and radar reflectivity-rain rate relationships for radar hydrology. *Hydrol. Earth Syst. Sci.* 5, 615-627.
- Ullah, S., Si, Y., Schlerf, M., Skidmore, A.K., Shafique, M., Iqbal, I.A., 2012. Estimation of grassland biomass and nitrogen using MERIS data. *Int. J. Appl. Earth Obs. Geoinf.* 19, 196-204.
- Usman, M., Liedl, R., Kavousi, A., 2015. Estimation of distributed seasonal net recharge by modern satellite data in irrigated agricultural regions of Pakistan. *Environ. Earth Sci.* 74, 1463-1486.

## Bibliography

- Van Loon, A.F., 2015. Hydrological drought explained. *Wiley Interdiscip. Rev.-Water* 2, 359-392.
- Vereecken, H., Huisman, J.A., Bogaen, H., Vanderborght, J., Vrugt, J.A., Hopmans, J.W., 2008. On the value of soil moisture measurements in vadose zone hydrology: A review. *Water Resour. Res.* 44, 21.
- Vereecken, H., Weihermuller, L., Jonard, F., Montzka, C., 2012. Characterization of Crop Canopies and Water Stress Related Phenomena using Microwave Remote Sensing Methods: A Review. *Vadose Zone J.* 11(2) doi: 10.2136/vzj2011.0138ra.
- Verhoef, W., 1984. LIGHT-SCATTERING BY LEAF LAYERS WITH APPLICATION TO CANOPY REFLECTANCE MODELING - THE SAIL MODEL. *Remote Sens. Environ.* 16, 125-141.
- Viglione, A., Parajka, J., Rogger, M., Salinas, J.L., Laaha, G., Sivapalan, M., Blöschl, G., 2013. Comparative assessment of predictions in ungauged basins - Part 3: Runoff signatures in Austria. *Hydrol. Earth Syst. Sci.* 17, 2263-2279.
- Vuolo, F., Atzberger, C., Richter, K., D'Urso, G., Dash, J., 2010. RETRIEVAL OF BIOPHYSICAL VEGETATION PRODUCTS FROM RAPIDEYE IMAGERY. 100 Years Isprs Advancing Remote Sensing Science, Pt 1 38, 281-286.
- Wagner, T., McIntyre, N., Lees, M.J., Wheeler, H.S., Gupta, H.V., 2003. Towards reduced uncertainty in conceptual rainfall-runoff modelling: Dynamic identifiability analysis. *Hydrol. Process.* 17, 455-476.
- Wagner, W., Verhoest, N.E.C., Ludwig, R., Tedesco, M., 2009. Editorial 'Remote sensing in hydrological sciences'. *Hydrol. Earth Syst. Sci.* 13, 813-817.
- Walthall, C., Dulaney, W., Anderson, M., Norman, J., Fang, H.L., Liang, S.L., 2004. A comparison of empirical and neural network approaches for estimating corn and soybean leaf area index from Landsat ETM+ imagery. *Remote Sens. Environ.* 92, 465-474.
- Wan, Z., Dozier, J., 1996. A generalised split-window algorithm for retrieving landsurface temperature from space. *IEEE Trans. Geosci. Remote Sens.* 34(4), 892-905.
- Wang, K.C., Wang, P., Li, Z.Q., Cribb, M., Sparrow, M., 2007. A simple method to estimate actual evapotranspiration from a combination of net radiation, vegetation index, and temperature. *J. Geophys. Res.-Atmos.* 112.
- Weihermueller, L., 2005. Comparison of Different Soil Water Extraction Systems for the Prognoses of Solute Transport at the Field Scale Using Numerical Simulations,

## Bibliography

- Field and Lysimeter Experiments. Diss. Rheinische Friedrich-Wilhelms-Universitaet, Bonn.
- Weihermuller, L., Huisman, J.A., Lambot, S., Herbst, M., Vereecken, H., 2007. Mapping the spatial variation of soil water content at the field scale with different ground penetrating radar techniques. *J. Hydrol.* 340, 205-216.
- Weiss, J.L., Gutzler, D.S., Coonrod, J.E.A., Dahm, C.N., 2004. Seasonal and inter-annual relationships between vegetation and climate in central New Mexico, USA. *J. Arid. Environ.* 57, 507-534.
- Wheater, H., Sorooshian, S., Sharma, K.D., 2008. *Hydrological Modelling in Arid and Semi-Arid Areas*. Cambridge Univ Press, Cambridge.
- White, M.A., Thornton, P.E., Running, S.W., Nemani, R.R., 2000. Parametrization and sensitivity analysis of the BIOME-BGC terrestrial ecosystem model: net primary production controls. *Earth Interact.* 4, 1-85.
- Wilhelm, W.W., Ruwe, K., Schlemmer, M.R., 2000. Comparison of three leaf area index meters in a corn canopy. *Crop Sci.* 40, 1179-1183.
- Willmott, C.J., Matsuura, K., 2005. Advantages of the mean absolute error (MAE) over the root mean square error (RMSE) in assessing average model performance. *Clim. Res.* 30, 79-82.
- Willmott, C.J., Rowe, C.M., Mintz, Y., 1985. CLIMATOLOGY OF THE TERRESTRIAL SEASONAL WATER CYCLE. *Journal of Climatology* 5, 589-606.
- WMO-2011, Available Online at: [http://www.wmo.int/pages/index\\_en.html](http://www.wmo.int/pages/index_en.html). Accessed on July, 2, 2016.
- Xiao, J.F., Moody, A., 2005. A comparison of methods for estimating fractional green vegetation cover within a desert-to-upland transition zone in central New Mexico, USA. *Remote Sens. Environ.* 98, 237-250.
- Xie, Y.C., Sha, Z.Y., Yu, M., 2008. Remote sensing imagery in vegetation mapping: a review. *J. Plant Ecol.* 1, 9-23.
- Xu, X.Y., Li, J., Tolson, B.A., 2014. Progress in integrating remote sensing data and hydrologic modeling. *Prog. Phys. Geogr.* 38, 464-498.
- Yang, R., Shukla, J., Sellers, P.J., 1994. The influence of changes in vegetation type on the surface energy budget. *Adv. Atmos. Sci.* 11(2), 139-161.
- Yang, X.J., Lo, C.P., 2000. Relative radiometric normalization performance for change detection from multi-date satellite images. *Photogramm. Eng. Remote Sens.* 66, 967-980.

## Bibliography

- Yu, W.P., Ma, M.G., 2015. Scale Mismatch Between In Situ and Remote Sensing Observations of Land Surface Temperature: Implications for the Validation of Remote Sensing LST Products. *IEEE Geosci. Remote Sens. Lett.* 12, 497-501.
- Zacharias, S., Bogena, H., Samaniego, L., Mauder, M., Fuss, R., Putz, T., Frenzel, M., Schwank, M., Baessler, C., Butterbach-Bahl, K., Bens, O., Borg, E., Brauer, A., Dietrich, P., Hajsek, I., Helle, G., Kiese, R., Kunstmann, H., Klotz, S., Munch, J.C., Papen, H., Priesack, E., Schmid, H.P., Steinbrecher, R., Rosenbaum, U., Teutsch, G., Vereecken, H., 2011. A Network of Terrestrial Environmental Observatories in Germany. *Vadose Zone J.* 10, 955-973.
- Zeng, X.B., Dickinson, R.E., Walker, A., Shaikh, M., DeFries, R.S., Qi, J.G., 2000. Derivation and evaluation of global 1-km fractional vegetation cover data for land modeling. *J. Appl. Meteorol.* 39, 826-839.
- Zeng, X.B., Rao, P., DeFries, R.S., Hansen, M.C., 2003. Interannual variability and decadal trend of global fractional vegetation cover from 1982 to 2000. *J. Appl. Meteorol.* 42, 1525-1530.

## Curriculum Vitae

### **PERSONAL INFORMATION**

---

Name: Muhammad Ali  
Address: St. No. 7, House No. 11, Palosi Road, Rahatabad, Peshawar, Pakistan.  
Date of Birth: 17/07/1981  
E-Mail: [aliumarzai@upesh.edu.pk](mailto:aliumarzai@upesh.edu.pk)  
Researchgate Profile [https://www.researchgate.net/profile/Muhammad\\_Ali106](https://www.researchgate.net/profile/Muhammad_Ali106)  
Phone (office): +92-91-9216427, 9216429  
Phone (mobile): +92-333-9153818

### **WORK EXPERIENCE**

---

06/2011 - 01/2014 National Centre of Excellence in Geology, University of Peshawar, Peshawar, Pakistan  
Research Associate

02/2014 – to date National Centre of Excellence in Geology, University of Peshawar, Peshawar, Pakistan  
Assistant Professor

11/2011 – 09/2015 Forschungszentrum Jülich GmbH, Institute for Bio- and Geosciences, Agrosphere Institute (IBG-3)  
PhD Student

10/2006-11/2006 International Centre for Integrated Mountain Development (ICIMOD), Kathmandu, Nepal  
Visiting Scientist

### **EDUCATION**

---

2017 University of Bonn  
Geography  
Degree: Dr. rer. nat.

2013 National Centre of Excellence in Geology, University of Peshawar, Peshawar, Pakistan  
Major: Remote Sensing, GIS, Tectonic Geomorphology  
Degree: MPhil (Master of Philosophy)  
Dissertation: 'Identifying Neotectonic Features using Lineament analysis of Satellite Images in Tectonically Active Muzaffarbad Area, Kashmir'

2004 National Centre of Excellence in Geology, University of Peshawar, Peshawar, Pakistan  
Major: GIS, Remote Sensing



Degree: Postgraduate Diploma

2003 Department of Geography, University of Peshawar, Peshawar, Pakistan  
Major: Geography  
Degree: MSc

### **ADDITIONAL TRAINING**

---

2012 English Academic Presentations  
*27, 29 November 2012, Cologne, Germany.*

2012 Graduate Course 'Inverse Modelling in Earth and  
Environmental Sciences'  
*30 July – 03 August 2012, KU Leuven, Leuven, Belgium*

2012 Scientific Writing Course  
*28 – 30 March 2012 Jülich, Germany*

### **LANGUAGE SKILLS**

---

Pashto  
Urdu  
English

### **IT SKILLS**

---

Microsoft Office  
Arc GIS  
Erdas Imagine, ATCOR  
ENVI, IR-MAD  
Matlab

### **PUBLICATIONS – PEER REVIEWED & CONFERENCE PROCEEDINGS**

---

**Ali, M.**, Montzka, C., Stadler, A., Menz, G., Thonfeld, F., Vereecken, H., (2015): Estimation and Validation of RapidEye-Based Time-Series of Leaf Area Index for Winter Wheat in the Rur Catchment (Germany). *Remote Sensing*, 7, 2808-2831.

Rudolph, S., Van der Kruk, J., Von Hebel, C., **Ali, M.**, Herbst, M., Montzka, C., Pätzold, S., Robinson, D.A., Vereecken, H., Weihermüller, L., (2015): Linking satellite derived LAI patterns with subsoil heterogeneity using large-scale ground-based electromagnetic induction measurements. *Geoderma*, 241-242, 262-271.

Hasan, S., Montzka, C., Rudiger, C., **Ali, M.**, Bogena, H., and Vereecken, H., (2014): Soil moisture retrieval from airborne L-band passive microwave using high resolution multispectral data. *ISPRS Journal of Photogrammetry and Remote Sensing*, 91, 59-17.

**Ali, M.**, Montzka, C., Stadler, A., Menz, G., Vereecken, H., (2013): Estimation and validation of leaf area index time-series for crops on 5m scale from space. *International geosciences and remote Sensing Symposium (IGARSS)*, Melbourne, Australia, Pages 3837-3840, DOI: 10.1109/IGARSS.2013.6723668.

**Ali, M.**, Montzka, C., Stadler, A., Vereecken, H., (2013): Validation of Leaf Area Index calculated on RapidEye imagery against *in situ* measurements in Rur catchment, Germany. In: Borg, Daedelow, Johnson (ed), *Proceedings of 5<sup>th</sup> RESA workshop (From the Basics to the Service)*, Neustrelitz, Germany, 159-171.

### **ORAL PRESENTATIONS**

---

**Ali, M.**, Montzka, C., Stadler, A., Vereecken, H., (2013): Validation of Leaf Area Index calculated on RapidEye imagery against *in situ* measurements in Rur catchment, Germany. 5<sup>th</sup> RESA workshop (From the Basics to the Service), Neustrelitz, Germany, 20-21 March 2013.

Wahab, A., **Ali, M.**, Khan, M. A., (2010). Peak Flood Inundation Map of the Western Peshawar Plain (Peshawar, Charsadda, Nowshera Districts): Implications for Flood Disaster Preparedness Plans. 'International Conference on Earth Sciences, Pakistan 2010 (New Developments)', Abstract in: *Journal of Himalayan Earth Sciences, Geological Bulletin, University of Peshawar*, (Vol. 43). Baragali, Pakistan, 20-22 September 2010.

Khan, J., **Ali, M.**, (2010). Use of GIS in Defining the Management Strategies for Groundwater Resources of Quetta Valley, Pakistan. *International Conference on 'Earth Sciences, Pakistan 2010 (New Developments)'*, Abstract in: *Journal of Himalayan Earth Sciences, Geological Bulletin, University of Peshawar*, (Vol. 43), Baragali, Pakistan, 20-22 September 2010.

### **POSTERS**

---

**Ali, M.**, Montzka, C., Graf, A., Jonard, F., Vereecken, H., (2014): Catchment Scale Estimation of Evapotranspiration from remote Sensing Data Based on an Energy Balance Approach: A Validation Study for the Rur Catchment, Germany. *European Geosciences Union General Assembly, Vienna, Austria*, 27 April - 02 May 2014.

Stadler, A., Rudolph, S., **Ali, M.**, Kupisch, M., Montzka, C., Langensiepen, M., and Ewert, F., (2014): Modeling crop growth heterogeneity patterns using apparent soil electrical conductivity maps. *Global Vegetation Monitoring and Modeling, Palais des Papes, Avignon, France*, 3 - 7 February 2014.

**Ali, M.**, Montzka, C., Stadler, A., Menz, G., Vereecken, H., (2013): Estimation and validation of leaf area index time-series for crops on 5m scale from space. *International geosciences and remote Sensing Symposium (IGARSS)*, Melbourne, Australia, 21 - 26 July 2013.

Rudolph, S., von Hebel, C., **Ali, M.**, Stadler, A., Herbst, M., Montzka, C., Puetzold, S., Weihermueller, L., van der Kruk, J., and Vereecken, H., (2013): Validation of a paleo river

system derived by ground based electromagnetic induction measurements with satellite based RapidEye images. European Geosciences Union General Assembly, Vienna, Austria, 7 - 12 April 2013.

Hasan, S., Montzka, C., Bogen, H., Ruediger, C., **Ali, M.**, and Vereecken, H., (2013): Vegetation effects on airborne passive microwave response to soil moisture: A case study for the Rur catchment, Germany. European Geosciences Union General Assembly, Vienna, Austria, 7 - 12 April 2013.

Band / Volume 389

**Modelling of High Temperature Polymer Electrolyte Fuel Cells**

Q. Cao (2017), 173 pp

ISBN: 978-3-95806-263-4

Band / Volume 390

**Potential use of nitrification inhibitors for mitigating N<sub>2</sub>O emission from soils**

D. Wu (2017), 206 pp

ISBN: 978-3-95806-264-1

Band / Volume 391

**Mechanical Characterization of Solid Oxide Fuel Cells and Sealants**

J. Wei (2017), II, 151 pp

ISBN: 978-3-95806-266-5

Band / Volume 392

**Microcrystalline Silicon Carbide for Silicon Heterojunction Solar Cells**

M. B. Pomaska (2017), 150 pp

ISBN: 978-3-95806-267-2

Band / Volume 393

**Einfluss der Kristallisation auf das Fließverhalten oxidischer Schmelzen**

S. Seebold (2017), 168 pp

ISBN: 978-3-95806-268-9

Band / Volume 394

**Water vapour in the UTLS – Climatologies and Transport**

P. R. Neis (2017), x, 124 pp

ISBN: 978-3-95806-269-6

Band / Volume 395

**Neutronenaktivierungsanalyse mit gepulsten 14 MeV Neutronen zur Charakterisierung heterogener radioaktiver Abfälle**

F. Mildenerger (2017), vi, 128 pp

ISBN: 978-3-95806-271-9

Band / Volume 396

**Coupled biotic-abiotic mechanisms of nitrous oxide production in soils during nitrification involving the reactive intermediates hydroxylamine and nitrite**

S. Liu (2017), xvii, 148 pp

ISBN: 978-3-95806-272-6

Band / Volume 397

**Mixed-phase and ice cloud observations with NIXE-CAPS**

A. Costa (2017), xviii, 117 pp

ISBN: 978-3-95806-273-3

Band / Volume 398

**Deposition Mechanisms of Thermal Barrier Coatings (TBCs)  
Manufactured by Plasma Spray-Physical Vapor Deposition (PS-PVD)**

W. He (2017), ix, 162 pp

ISBN: 978-3-95806-275-7

Band / Volume 399

**Carbonyl Sulfide in the Stratosphere: airborne instrument development  
and satellite based data analysis**

C. Kloss (2017), vi, 84, 1-14 pp

ISBN: 978-3-95806-276-4

Band / Volume 400

**Lagrangian transport of trace gases in the upper troposphere  
and lower stratosphere (UTLS)**

P. Konopka (2017), 70 pp

ISBN: 978-3-95806-279-5

Band / Volume 401

**Numerical Simulation of Plasma Spray-Physical Vapor Deposition**

P. Wang (2017), IX, 127 pp

ISBN: 978-3-95806-282-5

Band / Volume 402

**The Selective Separation of Am(III) from Highly Radioactive  
PUREX Raffinate**

P. Kaufholz (2017), IV, 173 pp

ISBN: 978-3-95806-284-9

Band / Volume 403

**Spatio-Temporal Estimation and Validation of Remotely Sensed  
Vegetation and Hydrological Fluxes in the Rur Catchment, Germany**

M. Ali (2018), xvi, 116 pp

ISBN: 978-3-95806-287-0



Energie & Umwelt / Energy & Environment  
Band / Volume 403  
ISBN 978-3-95806-287-0